PHYSICAL REVIEW D **109,** 022001 (2024)

Editors' Suggestion

GWTC-2.1: Deep extended catalog of compact binary coalescences observed by LIGO and Virgo during the first half of the third observing run

R. Abbott,[1] T. D. Abbott,[2] F. Acernese,[3,4] K. Ackley,[5] C. Adams,[6] N. Adhikari,[7] R. X. Adhikari,[1] V. B. Adya,[8] C. Affeldt,[9,10] D. Agarwal,[11] M. Agathos,[12,13] K. Agatsuma,[14] N. Aggarwal,[15] O. D. Aguiar,[16] L. Aiello,[17] A. Ain,[18] P. Ajith,[19] S. Albanesi,[20] A. Allocca,[21,4] P. A. Altin,[8] A. Amato,[22] C. Anand,[5] S. Anand,[1] A. Ananyeva,[1] S. B. Anderson,[1] W. G. Anderson,[7] T. Andrade,[23] N. Andres,[24] T. Andrić,[25] S. V. Angelova,[26] S. Ansoldi,[27,28] J. M. Antelis,[29] S. Antier,[30] S. Appert,[1] K. Arai,[1] M. C. Araya,[1] J. S. Areeda,[31] M. Arène,[30] N. Arnaud,[32,33] S. M. Aronson,[2] K. G. Arun,[34] Y. Asali,[35] G. Ashton,[5] M. Assiduo,[36,37] S. M. Aston,[6] P. Astone,[38] F. Aubin,[24] C. Austin,[2] S. Babak,[30] F. Badaracco,[39] M. K. M. Bader,[40] C. Badger,[41] S. Bae,[42] A. M. Baer,[43] S. Bagnasco,[20] Y. Bai,[1] J. Baird,[30] M. Ball,[44] G. Ballardin,[33] S. W. Ballmer,[45] A. Balsamo,[43] G. Baltus,[46] S. Banagiri,[47] D. Bankar,[11] J. C. Barayoga,[1] C. Barbieri,[48,49,50] B. C. Barish,[1] D. Barker,[51] P. Barneo,[23] F. Barone,[52,4] B. Barr,[53] L. Barsotti,[54] M. Barsuglia,[30] D. Barta,[55] J. Bartlett,[51] M. A. Barton,[53] I. Bartos,[56] R. Bassiri,[57] A. Basti,[58,18] M. Bawaj,[59,60] J. C. Bayley,[53] A. C. Baylor,[7] M. Bazzan,[61,62] B. Bécsy,[63] V. M. Bedakihale,[64] M. Bejger,[65] I. Belahcene,[32] V. Benedetto,[66] D. Beniwal,[67] T. F. Bennett,[68] J. D. Bentley,[14] M. BenYaala,[26] F. Bergamin,[9,10] B. K. Berger,[57] S. Bernuzzi,[13] C. P. L. Berry,[15,53] D. Bersanetti,[69] A. Bertolini,[40] J. Betzwieser,[6] D. Beveridge,[70] R. Bhandare,[71] U. Bhardwaj,[72,40] D. Bhattacharjee,[73] S. Bhaumik,[56] I. A. Bilenko,[74] G. Billingsley,[1] S. Bini,[75,76] R. Birney,[77] O. Birnholtz,[78] S. Biscans,[1,54] M. Bischi,[36,37] S. Biscoveanu,[54] A. Bisht,[9,10] B. Biswas,[11] M. Bitossi,[33,18] M.-A. Bizouard,[79] J. K. Blackburn,[1] C. D. Blair,[70,6] D. G. Blair,[70] R. M. Blair,[51] F. Bobba,[80,81] N. Bode,[9,10] M. Boer,[79] G. Bogaert,[79] M. Boldrini,[82,38] L. D. Bonavena,[61] F. Bondu,[83] E. Bonilla,[57] R. Bonnand,[24] P. Booker,[9,10] B. A. Boom,[40] R. Bork,[1] V. Boschi,[18] N. Bose,[84] S. Bose,[11] V. Bossilkov,[70] V. Boudart,[46] Y. Bouffanais,[61,62] A. Bozzi,[33] C. Bradaschia,[18] P. R. Brady,[7] A. Bramley,[6] A. Branch,[6] M. Branchesi,[25,85] J. E. Brau,[44] M. Breschi,[13] T. Briant,[86] J. H. Briggs,[53] A. Brillet,[79] M. Brinkmann,[9,10] P. Brockill,[7] A. F. Brooks,[1] J. Brooks,[33] D. D. Brown,[67] S. Brunett,[1] G. Bruno,[39] R. Bruntz,[43] J. Bryant,[14] T. Bulik,[87] H. J. Bulten,[40] A. Buonanno,[88,89] R. Buscicchio,[14] D. Buskulic,[24] C. Buy,[90] R. L. Byer,[57] L. Cadonati,[91] G. Cagnoli,[22] C. Cahillane,[51] J. Calderón Bustillo,[92,93] J. D. Callaghan,[53] T. A. Callister,[94,95] E. Calloni,[21,4] J. Cameron,[70] J. B. Camp,[96] M. Canepa,[97,69] S. Canevarolo,[98] M. Cannavacciuolo,[80] K. C. Cannon,[99] H. Cao,[67] E. Capote,[45] G. Carapella,[80,81] F. Carbognani,[33] J. B. Carlin,[100] M. F. Carney,[15] M. Carpinelli,[101,102,33] G. Carrillo,[44] G. Carullo,[58,18] T. L. Carver,[17] J. Casanueva Diaz,[33] C. Casentini,[103,104] G. Castaldi,[105] S. Caudill,[40,98] M. Cavaglià,[73] F. Cavalier,[32] R. Cavalieri,[33] M. Ceasar,[106] G. Cella,[18] P. Cerdá-Durán,[107] E. Cesarini,[104] W. Chaibi,[79] K. Chakravarti,[11] S. Chalathadka Subrahmanya,[108] E. Champion,[109] C.-H. Chan,[110] C. Chan,[99] C. L. Chan,[93] K. Chan,[93] K. Chandra,[84] P. Chanial,[33] S. Chao,[110] P. Charlton,[111] E. A. Chase,[15] E. Chassande-Mottin,[30] C. Chatterjee,[70] Debarati Chatterjee,[11] Deep Chatterjee,[7] D. Chattopadhyay,[112] M. Chaturvedi,[71] S. Chaty,[30] K. Chatziioannou,[1] H. Y. Chen,[54] J. Chen,[110] X. Chen,[70] Y. Chen,[113] Z. Chen,[17] H. Cheng,[56] C. K. Cheong,[93] H. Y. Cheung,[93] H. Y. Chia,[56] F. Chiadini,[114,81] G. Chiarini,[62] R. Chierici,[115] A. Chincarini,[69] M. L. Chiofalo,[58,18] A. Chiummo,[33] G. Cho,[116] H. S. Cho,[117] R. K. Choudhary,[70] S. Choudhary,[11] N. Christensen,[79] Q. Chu,[70] S. Chua,[8] K. W. Chung,[41] G. Ciani,[61,62] P. Ciecielag,[65] M. Cieślar,[65] M. Cifaldi,[103,104] A. A. Ciobanu,[67] R. Ciolfi,[118,62] F. Cipriano,[79] A. Cirone,[97,69] F. Clara,[51] E. N. Clark,[119] J. A. Clark,[1,91] L. Clarke,[120] P. Clearwater,[112] S. Clesse,[121] F. Cleva,[79] E. Coccia,[25,85] E. Codazzo,[25] P.-F. Cohadon,[86] D. E. Cohen,[32] L. Cohen,[2] M. Colleoni,[122] C. G. Collette,[123] A. Colombo,[48] M. Colpi,[48,49] C. M. Compton,[51] M. Constancio, Jr.,[16] L. Conti,[62] S. J. Cooper,[14] P. Corban,[6] T. R. Corbitt,[2] I. Cordero-Carrión,[124] S. Corezzi,[60,59] K. R. Corley,[35] N. Cornish,[63] D. Corre,[32] A. Corsi,[125] S. Cortese,[33] C. A. Costa,[16] R. Cotesta,[89] M. W. Coughlin,[47] J.-P. Coulon,[79] S. T. Countryman,[35] B. Cousins,[126] P. Couvares,[1] D. M. Coward,[70] M. J. Cowart,[6] D. C. Coyne,[1] R. Coyne,[127] J. D. E. Creighton,[7] T. D. Creighton,[128] A. W. Criswell,[47] M. Croquette,[86] S. G. Crowder,[129] J. R. Cudell,[46] T. J. Cullen,[2] A. Cumming,[53] R. Cummings,[53] L. Cunningham,[53] E. Cuoco,[33,130,18] M. Curyło,[87] P. Dabadie,[22] T. Dal Canton,[32] S. Dall'Osso,[25] G. Dálya,[131] A. Dana,[57] L. M. DaneshgaranBajastani,[68] B. D'Angelo,[97,69] B. Danila,[132] S. Danilishin,[133,40] S. D'Antonio,[104] K. Danzmann,[9,10] C. Darsow-Fromm,[108] A. Dasgupta,[64] L. E. H. Datrier,[53] S. Datta,[11] V. Dattilo,[33] I. Dave,[71] M. Davier,[32] G. S. Davies,[134] D. Davis,[1] M. C. Davis,[106] E. J. Daw,[135] R. Dean,[106] D. DeBra,[57] M. Deenadayalan,[11] J. Degallaix,[136] M. De Laurentis,[21,4] S. Deléglise,[86] V. Del Favero,[109] F. De Lillo,[39] N. De Lillo,[53] W. Del Pozzo,[58,18] L. M. DeMarchi,[15] F. De Matteis,[103,104] V. D'Emilio,[17] N. Demos,[54] T. Dent,[92] A. Depasse,[39] R. De Pietri,[137,138] R. De Rosa,[21,4] C. De Rossi,[33] R. DeSalvo,[105] R. De Simone,[114] S. Dhurandhar,[11] M. C. Díaz,[128] M. Diaz-Ortiz, Jr.,[56] N. A. Didio,[45] T. Dietrich,[89,40] L. Di Fiore,[4] C. Di Fronzo,[14] C. Di Giorgio,[80,81] F. Di Giovanni,[107] M. Di Giovanni,[25] T. Di Girolamo,[21,4] A. Di Lieto,[58,18] B. Ding,[123] S. Di Pace,[82,38] I. Di Palma,[82,38] F. Di Renzo,[58,18] A. K. Divakarla,[56] Divyajyoti,[139] A. Dmitriev,[14] Z. Doctor,[44] L. D'Onofrio,[21,4] F. Donovan,[54] K. L. Dooley,[17] S. Doravari,[11] I. Dorrington,[17] M. Drago,[82,38] J. C. Driggers,[51] Y. Drori,[1] J.-G. Ducoin,[32] P. Dupej,[53] O. Durante,[80,81] D. D'Urso,[101,102] P.-A. Duverne,[32] S. E. Dwyer,[51] C. Eassa,[51] P. J. Easter,[5] M. Ebersold,[140]

2470-0010/2024/109(2)/022001(45)

T. Eckhardt,[108] G. Eddolls,[53] B. Edelman,[44] T. B. Edo,[1] O. Edy,[134] A. Effler,[6] J. Eichholz,[8] S. S. Eikenberry,[56] M. Eisenmann,[24] R. A. Eisenstein,[54] A. Ejlli,[17] E. Engelby,[31] L. Errico,[21,4] R. C. Essick,[141] H. Estellés,[122] D. Estevez,[142] Z. Etienne,[143] T. Etzel,[1] M. Evans,[54] T. M. Evans,[6] B. E. Ewing,[126] V. Fafone,[103,104,25] H. Fair,[45] S. Fairhurst,[17] S. P. Fanning,[7] A. M. Farah,[141] S. Farinon,[69] B. Farr,[44] W. M. Farr,[94,95] N. W. Farrow,[5] E. J. Fauchon-Jones,[17] G. Favaro,[61] M. Favata,[144] M. Fays,[46] M. Fazio,[145] J. Feicht,[1] M. M. Fejer,[57] E. Fenyvesi,[55,146] D. L. Ferguson,[147] A. Fernandez-Galiana,[54] I. Ferrante,[58,18] T. A. Ferreira,[16] F. Fidecaro,[58,18] P. Figura,[87] I. Fiori,[33] M. Fishbach,[15] R. P. Fisher,[43] R. Fittipaldi,[148,81] V. Fiumara,[149,81] R. Flaminio,[24,150] E. Floden,[47] H. Fong,[99] J. A. Font,[107,151] B. Fornal,[152] P. W. F. Forsyth,[8] A. Franke,[108] S. Frasca,[82,38] F. Frasconi,[18] C. Frederick,[153] J. P. Freed,[29] Z. Frei,[131] A. Freise,[154] R. Frey,[44] P. Fritschel,[54] V. V. Frolov,[6] G. G. Fronzé,[20] P. Fulda,[56] M. Fyffe,[6] H. A. Gabbard,[53] W. Gabella,[155] B. U. Gadre,[89] J. R. Gair,[89] J. Gais,[93] S. Galaudage,[5] R. Gamba,[13] D. Ganapathy,[54] A. Ganguly,[19] S. G. Gaonkar,[11] B. Garaventa,[69,97] F. García,[30] C. García-Núñez,[77] C. García-Quirós,[122] F. Garufi,[21,4] B. Gateley,[51] S. Gaudio,[29] V. Gayathri,[56] G. Gemme,[69] A. Gennai,[18] J. George,[71] R. N. George,[147] O. Gerberding,[108] L. Gergely,[132] P. Gewecke,[108] S. Ghonge,[91] Abhirup Ghosh,[89] Archisman Ghosh,[156] Shaon Ghosh,[7,144] Shrobana Ghosh,[17] B. Giacomazzo,[48,49,50] L. Giacoppo,[82,38] J. A. Giaime,[2,6] K. D. Giardina,[6] D. R. Gibson,[77] C. Gier,[26] M. Giesler,[157] P. Giri,[18,58] F. Gissi,[66] J. Glanzer,[2] A. E. Gleckl,[31] P. Godwin,[126] E. Goetz,[158] R. Goetz,[56] N. Gohlke,[9,10] B. Goncharov,[5,25] G. González,[2] A. Gopakumar,[159] M. Gosselin,[33] R. Gouaty,[24] D. W. Gould,[8] B. Grace,[8] A. Grado,[160,4] M. Granata,[136] V. Granata,[80] A. Grant,[53] S. Gras,[54] P. Grassia,[1] C. Gray,[51] R. Gray,[53] G. Greco,[59] A. C. Green,[56] R. Green,[17] A. M. Gretarsson,[29] E. M. Gretarsson,[29] D. Griffith,[1] W. Griffiths,[17] H. L. Griggs,[91] G. Grignani,[60,59] A. Grimaldi,[75,76] S. J. Grimm,[25,85] H. Grote,[17] S. Grunewald,[89] P. Gruning,[32] D. Guerra,[107] G. M. Guidi,[36,37] A. R. Guimaraes,[2] G. Guixé,[23] H. K. Gulati,[64] H.-K. Guo,[152] Y. Guo,[40] Anchal Gupta,[1] Anuradha Gupta,[161] P. Gupta,[40,98] E. K. Gustafson,[1] R. Gustafson,[162] F. Guzman,[163] L. Haegel,[30] O. Halim,[28,164] E. D. Hall,[54] E. Z. Hamilton,[140] G. Hammond,[53] M. Haney,[140] J. Hanks,[51] C. Hanna,[126] M. D. Hannam,[17] O. Hannuksela,[98,40] H. Hansen,[51] T. J. Hansen,[29] J. Hanson,[6] T. Harder,[79] T. Hardwick,[2] K. Haris,[40,98] J. Harms,[25,85] G. M. Harry,[165] I. W. Harry,[134] D. Hartwig,[108] B. Haskell,[65] R. K. Hasskew,[6] C.-J. Haster,[54] K. Haughian,[53] F. J. Hayes,[53] J. Healy,[109] A. Heidmann,[86] A. Heidt,[9,10] M. C. Heintze,[6] J. Heinze,[9,10] J. Heinzel,[166] H. Heitmann,[79] F. Hellman,[167] P. Hello,[32] A. F. Helmling-Cornell,[44] G. Hemming,[33] M. Hendry,[53] I. S. Heng,[53] E. Hennes,[40] J. Hennig,[168] M. H. Hennig,[168] A. G. Hernandez,[68] F. Hernandez Vivanco,[5] M. Heurs,[9,10] S. Hild,[133,40] P. Hill,[26] A. S. Hines,[163] S. Hochheim,[9,10] D. Hofman,[136] J. N. Hohmann,[108] D. G. Holcomb,[106] N. A. Holland,[8] K. Holley-Bockelmann,[155] I. J. Hollows,[135] Z. J. Holmes,[67] K. Holt,[6] D. E. Holz,[141] P. Hopkins,[17] J. Hough,[53] S. Hourihane,[113] E. J. Howell,[70] C. G. Hoy,[17] D. Hoyland,[14] A. Hreibi,[9,10] Y. Hsu,[110] Y. Huang,[54] M. T. Hübner,[5] A. D. Huddart,[120] B. Hughey,[29] V. Hui,[24] S. Husa,[122] S. H. Huttner,[53] R. Huxford,[126] T. Huynh-Dinh,[6] B. Idzkowski,[87] A. Iess,[103,104] C. Ingram,[67] M. Isi,[54] K. Isleif,[108] B. R. Iyer,[19] V. JaberianHamedan,[70] T. Jacqmin,[86] S. J. Jadhav,[169] S. P. Jadhav,[11] A. L. James,[17] A. Z. Jan,[109] K. Jani,[155] J. Janquart,[98,40] K. Janssens,[170,79] N. N. Janthalur,[169] P. Jaranowski,[171] D. Jariwala,[56] R. Jaume,[122] A. C. Jenkins,[41] K. Jenner,[67] M. Jeunon,[47] W. Jia,[54] G. R. Johns,[43] N. K. Johnson-McDaniel,[12] A. W. Jones,[70] D. I. Jones,[172] J. D. Jones,[51] P. Jones,[14] R. Jones,[53] R. J. G. Jonker,[40] L. Ju,[70] J. Junker,[9,10] V. Juste,[142] C. V. Kalaghatgi,[17,98] V. Kalogera,[15] B. Kamai,[1] S. Kandhasamy,[11] G. Kang,[173] J. B. Kanner,[1] Y. Kao,[110] S. J. Kapadia,[19] D. P. Kapasi,[8] S. Karat,[1] C. Karathanasis,[174] S. Karki,[73] R. Kashyap,[126] M. Kasprzack,[1] W. Kastaun,[9,10] S. Katsanevas,[33] E. Katsavounidis,[54] W. Katzman,[6] T. Kaur,[70] K. Kawabe,[51] F. Kéfélian,[79] D. Keitel,[122] J. S. Key,[175] S. Khadka,[57] F. Y. Khalili,[74] S. Khan,[17] E. A. Khazanov,[176] N. Khetan,[25,85] M. Khursheed,[71] N. Kijbunchoo,[8] C. Kim,[177] J. C. Kim,[178] K. Kim,[179] W. S. Kim,[180] Y.-M. Kim,[181] C. Kimball,[15] M. Kinley-Hanlon,[53] R. Kirchhoff,[9,10] J. S. Kissel,[51] L. Kleybolte,[108] S. Klimenko,[56] A. M. Knee,[158] T. D. Knowles,[143] E. Knyazev,[54] P. Koch,[9,10] G. Koekoek,[40,133] S. Koley,[25] P. Kolitsidou,[17] M. Kolstein,[174] K. Komori,[54] V. Kondrashov,[1] A. Kontos,[182] N. Koper,[9,10] M. Korobko,[108] M. Kovalam,[70] D. B. Kozak,[1] V. Kringel,[9,10] N. V. Krishnendu,[9,10] A. Królak,[183,184] G. Kuehn,[9,10] F. Kuei,[110] P. Kuijer,[40] S. Kulkarni,[161] A. Kumar,[169] P. Kumar,[157] Rahul Kumar,[51] Rakesh Kumar,[64] K. Kuns,[54] S. Kuwahara,[99] P. Lagabbe,[24] D. Laghi,[58,18] E. Lalande,[185] T. L. Lam,[93] A. Lamberts,[79,186] M. Landry,[51] B. B. Lane,[54] R. N. Lang,[54] J. Lange,[147] B. Lantz,[57] I. La Rosa,[24] A. Lartaux-Vollard,[32] P. D. Lasky,[5] M. Laxen,[6] A. Lazzarini,[1] C. Lazzaro,[61,62] P. Leaci,[82,38] S. Leavey,[9,10] Y. K. Lecoeuche,[158] H. M. Lee,[116] H. W. Lee,[178] J. Lee,[116] K. Lee,[187] J. Lehmann,[9,10] A. Lemaître,[188] N. Leroy,[32] N. Letendre,[24] C. Levesque,[185] Y. Levin,[5] J. N. Leviton,[162] K. Leyde,[30] A. K. Y. Li,[1] B. Li,[110] J. Li,[15] T. G. F. Li,[93] X. Li,[113] F. Linde,[189,40] S. D. Linker,[68] J. N. Linley,[53] T. B. Littenberg,[190] J. Liu,[9,10] K. Liu,[110] X. Liu,[7] F. Llamas,[128] M. Llorens-Monteagudo,[107] R. K. L. Lo,[1] A. Lockwood,[191] L. T. London,[54] A. Longo,[192,193] D. Lopez,[140] M. Lopez Portilla,[98] M. Lorenzini,[103,104] V. Loriette,[194] M. Lormand,[6] G. Losurdo,[18] T. P. Lott,[91] J. D. Lough,[9,10] C. O. Lousto,[109] G. Lovelace,[31] J. F. Lucaccioni,[153] H. Lück,[9,10] D. Lumaca,[103,104] A. P. Lundgren,[134] J. E. Lynam,[43] R. Macas,[134] M. MacInnis,[54] D. M. Macleod,[17] I. A. O. MacMillan,[1] A. Macquet,[79] I. Magaña Hernandez,[7] C. Magazzù,[18] R. M. Magee,[1] R. Maggiore,[14] M. Magnozzi,[69,97] S. Mahesh,[143] E. Majorana,[82,38] C. Makarem,[1] I. Maksimovic,[194] S. Maliakal,[1] A. Malik,[71] N. Man,[79] V. Mandic,[47] V. Mangano,[82,38] J. L. Mango,[195] G. L. Mansell,[51,54] M. Manske,[7] M. Mantovani,[33] M. Mapelli,[61,62] F. Marchesoni,[196,59,197] F. Marion,[24] Z. Mark,[113] S. Márka,[35] Z. Márka,[35] C. Markakis,[12] A. S. Markosyan,[57] A. Markowitz,[1] E. Maros,[1] A. Marquina,[124] S. Marsat,[30]

F. Martelli,[36,37] I. W. Martin,[53] R. M. Martin,[144] M. Martinez,[174] V. A. Martinez,[56] V. Martinez,[22] K. Martinovic,[41]
D. V. Martynov,[14] E. J. Marx,[54] H. Masalehdan,[108] K. Mason,[54] E. Massera,[135] A. Masserot,[24] T. J. Massinger,[54]
M. Masso-Reid,[53] S. Mastrogiovanni,[30] A. Matas,[89] M. Mateu-Lucena,[122] F. Matichard,[1,54] M. Matiushechkina,[9,10]
N. Mavalvala,[54] J. J. McCann,[70] R. McCarthy,[51] D. E. McClelland,[8] P. K. McClincy,[126] S. McCormick,[6] L. McCuller,[54]
G. I. McGhee,[53] S. C. McGuire,[198] C. McIsaac,[134] J. McIver,[158] T. McRae,[8] S. T. McWilliams,[143] D. Meacher,[7]
M. Mehmet,[9,10] A. K. Mehta,[89] Q. Meijer,[98] A. Melatos,[100] D. A. Melchor,[31] G. Mendell,[51] A. Menendez-Vazquez,[174]
C. S. Menoni,[145] R. A. Mercer,[7] L. Mereni,[136] K. Merfeld,[44] E. L. Merilh,[6] J. D. Merritt,[44] M. Merzougui,[79] S. Meshkov,[1,*]
C. Messenger,[53] C. Messick,[147] P. M. Meyers,[100] F. Meylahn,[9,10] A. Mhaske,[11] A. Miani,[75,76] H. Miao,[14] I. Michaloliakos,[56]
C. Michel,[136] H. Middleton,[100] L. Milano,[21] A. Miller,[68] A. L. Miller,[39] B. Miller,[72,40] M. Millhouse,[100] J. C. Mills,[17]
E. Milotti,[164,28] O. Minazzoli,[79,199] Y. Minenkov,[104] Ll. M. Mir,[174] M. Miravet-Tenés,[107] C. Mishra,[139] T. Mishra,[56]
T. Mistry,[135] S. Mitra,[11] V. P. Mitrofanov,[74] G. Mitselmakher,[56] R. Mittleman,[54] Geoffrey Mo,[54] E. Moguel,[153]
K. Mogushi,[73] S. R. P. Mohapatra,[54] S. R. Mohite,[7] I. Molina,[31] M. Molina-Ruiz,[167] M. Mondin,[68] M. Montani,[36,37]
C. J. Moore,[14] D. Moraru,[51] F. Morawski,[65] A. More,[11] C. Moreno,[29] G. Moreno,[51] S. Morisaki,[7] B. Mours,[142]
C. M. Mow-Lowry,[14,154] S. Mozzon,[134] F. Muciaccia,[82,38] Arunava Mukherjee,[200] D. Mukherjee,[126] Soma Mukherjee,[128]
Subroto Mukherjee,[64] Suvodip Mukherjee,[72] N. Mukund,[9,10] A. Mullavey,[6] J. Munch,[67] E. A. Muñiz,[45] P. G. Murray,[53]
R. Musenich,[69,97] S. Muusse,[67] S. L. Nadji,[9,10] A. Nagar,[20,201] V. Napolano,[33] I. Nardecchia,[103,104] L. Naticchioni,[38]
B. Nayak,[68] R. K. Nayak,[202] B. F. Neil,[70] J. Neilson,[66,81] G. Nelemans,[203] T. J. N. Nelson,[6] M. Nery,[9,10] P. Neubauer,[153]
A. Neunzert,[175] K. Y. Ng,[54] S. W. S. Ng,[67] C. Nguyen,[30] P. Nguyen,[44] T. Nguyen,[54] S. A. Nichols,[2] S. Nissanke,[72,40]
E. Nitoglia,[115] F. Nocera,[33] M. Norman,[17] C. North,[17] L. K. Nuttall,[134] J. Oberling,[51] B. D. O'Brien,[56] J. O'Dell,[120]
E. Oelker,[53] G. Oganesyan,[25,85] J. J. Oh,[180] S. H. Oh,[180] F. Ohme,[9,10] H. Ohta,[99] M. A. Okada,[16] C. Olivetto,[33] R. Oram,[6]
B. O'Reilly,[6] R. G. Ormiston,[47] N. D. Ormsby,[43] L. F. Ortega,[56] R. O'Shaughnessy,[109] E. O'Shea,[157] S. Ossokine,[89]
C. Osthelder,[1] D. J. Ottaway,[67] H. Overmier,[6] A. E. Pace,[126] G. Pagano,[58,18] M. A. Page,[70] G. Pagliaroli,[25,85] A. Pai,[84]
S. A. Pai,[71] J. R. Palamos,[44] O. Palashov,[176] C. Palomba,[38] H. Pan,[110] P. K. Panda,[169] P. T. H. Pang,[40,98] C. Pankow,[15]
F. Pannarale,[82,38] B. C. Pant,[71] F. H. Panther,[70] F. Paoletti,[18] A. Paoli,[33] A. Paolone,[38,204] H. Park,[7] W. Parker,[6,198]
D. Pascucci,[40] A. Pasqualetti,[33] R. Passaquieti,[58,18] D. Passuello,[18] M. Patel,[43] M. Pathak,[67] B. Patricelli,[33,18] A. S. Patron,[2]
S. Patrone,[82,38] S. Paul,[44] E. Payne,[5] M. Pedraza,[1] M. Pegoraro,[62] A. Pele,[6] S. Penn,[205] A. Perego,[75,76] A. Pereira,[22]
T. Pereira,[206] C. J. Perez,[51] C. Périgois,[24] C. C. Perkins,[56] A. Perreca,[75,76] S. Perriès,[115] J. Petermann,[108] D. Petterson,[1]
H. P. Pfeiffer,[89] K. A. Pham,[47] K. S. Phukon,[40,189] O. J. Piccinni,[38] M. Pichot,[79] M. Piendibene,[58,18] F. Piergiovanni,[36,37]
L. Pierini,[82,38] V. Pierro,[66,81] G. Pillant,[33] M. Pillas,[32] F. Pilo,[18] L. Pinard,[136] I. M. Pinto,[66,81,207] M. Pinto,[33]
K. Piotrzkowski,[39] M. Pirello,[51] M. D. Pitkin,[208] E. Placidi,[82,38] L. Planas,[122] W. Plastino,[192,193] C. Pluchar,[119]
R. Poggiani,[58,18] E. Polini,[24] D. Y. T. Pong,[93] S. Ponrathnam,[11] P. Popolizio,[33] E. K. Porter,[30] R. Poulton,[33] J. Powell,[112]
M. Pracchia,[24] T. Pradier,[142] A. K. Prajapati,[64] K. Prasai,[57] R. Prasanna,[169] G. Pratten,[14] M. Principe,[66,207,81]
G. A. Prodi,[209,76] L. Prokhorov,[14] P. Prosposito,[103,104] L. Prudenzi,[89] A. Puecher,[40,98] M. Punturo,[59] F. Puosi,[18,58] P. Puppo,[38]
M. Pürrer,[89] H. Qi,[17] V. Quetschke,[128] R. Quitzow-James,[73] F. J. Raab,[51] G. Raaijmakers,[72,40] H. Radkins,[51] N. Radulesco,[79]
P. Raffai,[131] S. X. Rail,[185] S. Raja,[71] C. Rajan,[71] K. E. Ramirez,[6] T. D. Ramirez,[31] A. Ramos-Buades,[89] J. Rana,[126]
P. Rapagnani,[82,38] U. D. Rapol,[210] A. Ray,[7] V. Raymond,[17] N. Raza,[158] M. Razzano,[58,18] J. Read,[31] L. A. Rees,[165]
T. Regimbau,[24] L. Rei,[69] S. Reid,[26] S. W. Reid,[43] D. H. Reitze,[1,56] P. Relton,[17] A. Renzini,[1] P. Rettegno,[211,20] A. Reza,[40]
M. Rezac,[31] F. Ricci,[82,38] D. Richards,[120] J. W. Richardson,[1] L. Richardson,[163] G. Riemenschneider,[211,20] K. Riles,[162]
S. Rinaldi,[18,58] K. Rink,[158] M. Rizzo,[15] N. A. Robertson,[1,53] R. Robie,[1] F. Robinet,[32] A. Rocchi,[104] S. Rodriguez,[31]
L. Rolland,[24] J. G. Rollins,[1] M. Romanelli,[83] R. Romano,[3,4] C. L. Romel,[51] A. Romero-Rodríguez,[174] I. M. Romero-Shaw,[5]
J. H. Romie,[6] S. Ronchini,[25,85] L. Rosa,[4,21] C. A. Rose,[7] M. J. B. Rosell,[147] D. Rosińska,[87] M. P. Ross,[191] S. Rowan,[53]
S. J. Rowlinson,[14] S. Roy,[98] Santosh Roy,[11] Soumen Roy,[212] D. Rozza,[101,102] P. Ruggi,[33] K. Ruiz-Rocha,[155] K. Ryan,[51]
S. Sachdev,[126] T. Sadecki,[51] J. Sadiq,[92] M. Sakellariadou,[41] O. S. Salafia,[50,49,48] L. Salconi,[33] M. Saleem,[47] F. Salemi,[75,76]
A. Samajdar,[40,98] E. J. Sanchez,[1] J. H. Sanchez,[31] L. E. Sanchez,[1] N. Sanchis-Gual,[213] J. R. Sanders,[214] A. Sanuy,[23]
T. R. Saravanan,[11] N. Sarin,[5] B. Sassolas,[136] H. Satari,[70] O. Sauter,[56] R. L. Savage,[51] D. Sawant,[84] H. L. Sawant,[11]
S. Sayah,[136] D. Schaetzl,[1] M. Scheel,[113] J. Scheuer,[15] M. Schiworski,[67] P. Schmidt,[14] S. Schmidt,[98] R. Schnabel,[108]
M. Schneewind,[9,10] R. M. S. Schofield,[44] A. Schönbeck,[108] B. W. Schulte,[9,10] B. F. Schutz,[17,9,10] E. Schwartz,[17] J. Scott,[53]
S. M. Scott,[8] M. Seglar-Arroyo,[24] D. Sellers,[6] A. S. Sengupta,[212] D. Sentenac,[33] E. G. Seo,[93] V. Sequino,[21,4] A. Sergeev,[176]
Y. Setyawati,[98] T. Shaffer,[51] M. S. Shahriar,[15] B. Shams,[152] A. Sharma,[25,85] P. Sharma,[71] P. Shawhan,[88]
N. S. Shcheblanov,[188] M. Shikauchi,[99] D. H. Shoemaker,[54] D. M. Shoemaker,[147] S. ShyamSundar,[71] M. Sieniawska,[87]
D. Sigg,[51] L. P. Singer,[96] D. Singh,[126] N. Singh,[87] A. Singha,[133,40] A. M. Sintes,[122] V. Sipala,[101,102] V. Skliris,[17]
B. J. J. Slagmolen,[8] T. J. Slaven-Blair,[70] J. Smetana,[14] J. R. Smith,[31] R. J. E. Smith,[5] J. Soldateschi,[215,216,37] S. N. Somala,[217]
E. J. Son,[180] K. Soni,[11] S. Soni,[2] V. Sordini,[115] F. Sorrentino,[69] N. Sorrentino,[58,18] R. Soulard,[79] T. Souradeep,[210,11]
E. Sowell,[125] V. Spagnuolo,[133,40] A. P. Spencer,[53] M. Spera,[61,62] R. Srinivasan,[79] A. K. Srivastava,[64] V. Srivastava,[45]
K. Staats,[15] C. Stachie,[79] D. A. Steer,[30] J. Steinhoff,[89] J. Steinlechner,[133,40] S. Steinlechner,[133,40] S. Stevenson,[112]

D. J. Stops,[14] M. Stover,[153] K. A. Strain,[53] L. C. Strang,[100] G. Stratta,[218,37] A. Strunk,[51] R. Sturani,[206] A. L. Stuver,[106] S. Sudhagar,[11] V. Sudhir,[54] H. G. Suh,[7] T. Z. Summerscales,[219] H. Sun,[70] L. Sun,[8] S. Sunil,[64] A. Sur,[65] J. Suresh,[99] P. J. Sutton,[17] B. L. Swinkels,[40] M. J. Szczepańczyk,[56] P. Szewczyk,[87] M. Tacca,[40] S. C. Tait,[53] C. J. Talbot,[26] C. Talbot,[1] A. J. Tanasijczuk,[39] D. B. Tanner,[56] D. Tao,[1] L. Tao,[56] E. N. Tapia San Martín,[40] C. Taranto,[103] J. D. Tasson,[166] R. Tenorio,[122] J. E. Terhune,[106] L. Terkowski,[108] M. P. Thirugnanasambandam,[11] L. Thomas,[14] M. Thomas,[6] P. Thomas,[51] J. E. Thompson,[17] S. R. Thondapu,[71] K. A. Thorne,[6] E. Thrane,[5] Shubhanshu Tiwari,[140] Srishti Tiwari,[11] V. Tiwari,[17] A. M. Toivonen,[47] K. Toland,[53] A. E. Tolley,[134] M. Tonelli,[58,18] A. Torres-Forné,[107] C. I. Torrie,[1] I. Tosta e Melo,[101,102] D. Töyrä,[8] A. Trapananti,[196,59] F. Travasso,[59,196] G. Traylor,[6] M. Trevor,[88] M. C. Tringali,[33] A. Tripathee,[162] L. Troiano,[220,81] A. Trovato,[30] L. Trozzo,[4] R. J. Trudeau,[1] D. S. Tsai,[110] D. Tsai,[110] K. W. Tsang,[40,221,98] M. Tse,[54] R. Tso,[113] L. Tsukada,[99] D. Tsuna,[99] T. Tsutsui,[99] K. Turbang,[222,170] M. Turconi,[79] A. S. Ubhi,[14] R. P. Udall,[1] K. Ueno,[99] C. S. Unnikrishnan,[159] A. L. Urban,[2] A. Utina,[133,40] H. Vahlbruch,[9,10] G. Vajente,[1] A. Vajpeyi,[5] G. Valdes,[163] M. Valentini,[75,76] V. Valsan,[7] N. van Bakel,[40] M. van Beuzekom,[40] J. F. J. van den Brand,[133,223,40] C. Van Den Broeck,[98,40] D. C. Vander-Hyde,[45] L. van der Schaaf,[40] J. V. van Heijningen,[39] J. Vanosky,[1] N. van Remortel,[170] M. Vardaro,[189,40] A. F. Vargas,[100] V. Varma,[157] M. Vasúth,[55] A. Vecchio,[14] G. Vedovato,[62] J. Veitch,[53] P. J. Veitch,[67] J. Venneberg,[9,10] G. Venugopalan,[1] D. Verkindt,[24] P. Verma,[184] Y. Verma,[71] D. Veske,[35] F. Vetrano,[36] A. Viceré,[36,37] S. Vidyant,[45] A. D. Viets,[195] A. Vijaykumar,[19] V. Villa-Ortega,[92] J.-Y. Vinet,[79] A. Virtuoso,[164,28] S. Vitale,[54] T. Vo,[45] H. Vocca,[60,59] E. R. G. von Reis,[51] J. S. A. von Wrangel,[9,10] C. Vorvick,[51] S. P. Vyatchanin,[74] L. E. Wade,[153] M. Wade,[153] K. J. Wagner,[109] R. C. Walet,[40] M. Walker,[43] G. S. Wallace,[26] L. Wallace,[1] S. Walsh,[7] J. Z. Wang,[162] W. H. Wang,[128] R. L. Ward,[8] J. Warner,[51] M. Was,[24] N. Y. Washington,[1] J. Watchi,[123] B. Weaver,[51] S. A. Webster,[53] M. Weinert,[9,10] A. J. Weinstein,[1] R. Weiss,[54] C. M. Weller,[191] R. Weller,[155] F. Wellmann,[9,10] L. Wen,[70] P. Weßels,[9,10] K. Wette,[8] J. T. Whelan,[109] D. D. White,[31] B. F. Whiting,[56] C. Whittle,[54] D. Wilken,[9,10] D. Williams,[53] M. J. Williams,[53] A. R. Williamson,[134] J. L. Willis,[1] B. Willke,[9,10] D. J. Wilson,[119] W. Winkler,[9,10] C. C. Wipf,[1] T. Wlodarczyk,[89] G. Woan,[53] J. Woehler,[9,10] J. K. Wofford,[109] I. C. F. Wong,[93] D. S. Wu,[9,10] D. M. Wysocki,[7] L. Xiao,[1] H. Yamamoto,[1] F. W. Yang,[152] L. Yang,[145] Yang Yang,[56] Z. Yang,[47] M. J. Yap,[8] D. W. Yeeles,[17] A. B. Yelikar,[109] M. Ying,[110] J. Yoo,[157] Hang Yu,[113] Haocun Yu,[54] A. Zadrożny,[184] M. Zanolin,[29] T. Zelenova,[33] J.-P. Zendri,[62] M. Zevin,[141] J. Zhang,[70] L. Zhang,[1] T. Zhang,[14] Y. Zhang,[163] C. Zhao,[70] G. Zhao,[123] Yue Zhao,[152] R. Zhou,[167] Z. Zhou,[15] X. J. Zhu,[5] A. B. Zimmerman,[147] Y. Zlochower,[109] M. E. Zucker,[1,54] and J. Zweizig[1]

(The LIGO Scientific Collaboration and the Virgo Collaboration)

[1]*LIGO Laboratory, California Institute of Technology, Pasadena, California 91125, USA*
[2]*Louisiana State University, Baton Rouge, Louisiana 70803, USA*
[3]*Dipartimento di Farmacia, Università di Salerno, I-84084 Fisciano, Salerno, Italy*
[4]*INFN, Sezione di Napoli, Complesso Universitario di Monte S. Angelo, I-80126 Napoli, Italy*
[5]*OzGrav, School of Physics and Astronomy, Monash University, Clayton 3800, Victoria, Australia*
[6]*LIGO Livingston Observatory, Livingston, Louisiana 70754, USA*
[7]*University of Wisconsin-Milwaukee, Milwaukee, Wisconsin 53201, USA*
[8]*OzGrav, Australian National University, Canberra, Australian Capital Territory 0200, Australia*
[9]*Max Planck Institute for Gravitational Physics (Albert Einstein Institute), D-30167 Hannover, Germany*
[10]*Leibniz Universität Hannover, D-30167 Hannover, Germany*
[11]*Inter-University Centre for Astronomy and Astrophysics, Pune 411007, India*
[12]*University of Cambridge, Cambridge CB2 1TN, United Kingdom*
[13]*Theoretisch-Physikalisches Institut, Friedrich-Schiller-Universität Jena, D-07743 Jena, Germany*
[14]*University of Birmingham, Birmingham B15 2TT, United Kingdom*
[15]*Center for Interdisciplinary Exploration and Research in Astrophysics (CIERA),*
Northwestern University, Evanston, Illinois 60208, USA
[16]*Instituto Nacional de Pesquisas Espaciais, 12227-010 São José dos Campos, São Paulo, Brazil*
[17]*Gravity Exploration Institute, Cardiff University, Cardiff CF24 3AA, United Kingdom*
[18]*INFN, Sezione di Pisa, I-56127 Pisa, Italy*
[19]*International Centre for Theoretical Sciences, Tata Institute of Fundamental Research,*
Bengaluru 560089, India
[20]*INFN Sezione di Torino, I-10125 Torino, Italy*
[21]*Università di Napoli "Federico II", Complesso Universitario di Monte S. Angelo, I-80126 Napoli, Italy*
[22]*Université de Lyon, Université Claude Bernard Lyon 1, CNRS,*
Institut Lumière Matière, F-69622 Villeurbanne, France
[23]*Institut de Ciències del Cosmos (ICCUB), Universitat de Barcelona, C/ Martí i Franquès 1,*
Barcelona, 08028, Spain

[24]*Laboratoire d'Annecy de Physique des Particules (LAPP), Univ. Grenoble Alpes,*
Université Savoie Mont Blanc, CNRS/IN2P3, F-74941 Annecy, France
[25]*Gran Sasso Science Institute (GSSI), I-67100 L'Aquila, Italy*
[26]*SUPA, University of Strathclyde, Glasgow G1 1XQ, United Kingdom*
[27]*Dipartimento di Scienze Matematiche, Informatiche e Fisiche, Università di Udine, I-33100 Udine, Italy*
[28]*INFN, Sezione di Trieste, I-34127 Trieste, Italy*
[29]*Embry-Riddle Aeronautical University, Prescott, Arizona 86301, USA*
[30]*Université de Paris, CNRS, Astroparticule et Cosmologie, F-75006 Paris, France*
[31]*California State University Fullerton, Fullerton, California 92831, USA*
[32]*Université Paris-Saclay, CNRS/IN2P3, IJCLab, 91405 Orsay, France*
[33]*European Gravitational Observatory (EGO), I-56021 Cascina, Pisa, Italy*
[34]*Chennai Mathematical Institute, Chennai 603103, India*
[35]*Columbia University, New York, New York 10027, USA*
[36]*Università degli Studi di Urbino "Carlo Bo", I-61029 Urbino, Italy*
[37]*INFN, Sezione di Firenze, I-50019 Sesto Fiorentino, Firenze, Italy*
[38]*INFN, Sezione di Roma, I-00185 Roma, Italy*
[39]*Université catholique de Louvain, B-1348 Louvain-la-Neuve, Belgium*
[40]*Nikhef, Science Park 105, 1098 XG Amsterdam, Netherlands*
[41]*King's College London, University of London, London WC2R 2LS, United Kingdom*
[42]*Korea Institute of Science and Technology Information, Daejeon 34141, South Korea*
[43]*Christopher Newport University, Newport News, Virginia 23606, USA*
[44]*University of Oregon, Eugene, Oregon 97403, USA*
[45]*Syracuse University, Syracuse, New York 13244, USA*
[46]*Université de Liège, B-4000 Liège, Belgium*
[47]*University of Minnesota, Minneapolis, Minnesota 55455, USA*
[48]*Università degli Studi di Milano-Bicocca, I-20126 Milano, Italy*
[49]*INFN, Sezione di Milano-Bicocca, I-20126 Milano, Italy*
[50]*INAF, Osservatorio Astronomico di Brera sede di Merate, I-23807 Merate, Lecco, Italy*
[51]*LIGO Hanford Observatory, Richland, Washington 99352, USA*
[52]*Dipartimento di Medicina, Chirurgia e Odontoiatria "Scuola Medica Salernitana",*
Università di Salerno, I-84081 Baronissi, Salerno, Italy
[53]*SUPA, University of Glasgow, Glasgow G12 8QQ, United Kingdom*
[54]*LIGO Laboratory, Massachusetts Institute of Technology, Cambridge, Massachusetts 02139, USA*
[55]*Wigner RCP, RMKI, H-1121 Budapest, Konkoly Thege Miklós út 29-33, Hungary*
[56]*University of Florida, Gainesville, Florida 32611, USA*
[57]*Stanford University, Stanford, California 94305, USA*
[58]*Università di Pisa, I-56127 Pisa, Italy*
[59]*INFN, Sezione di Perugia, I-06123 Perugia, Italy*
[60]*Università di Perugia, I-06123 Perugia, Italy*
[61]*Università di Padova, Dipartimento di Fisica e Astronomia, I-35131 Padova, Italy*
[62]*INFN, Sezione di Padova, I-35131 Padova, Italy*
[63]*Montana State University, Bozeman, Montana 59717, USA*
[64]*Institute for Plasma Research, Bhat, Gandhinagar 382428, India*
[65]*Nicolaus Copernicus Astronomical Center, Polish Academy of Sciences, 00-716, Warsaw, Poland*
[66]*Dipartimento di Ingegneria, Università del Sannio, I-82100 Benevento, Italy*
[67]*OzGrav, University of Adelaide, Adelaide, South Australia 5005, Australia*
[68]*California State University, Los Angeles, 5151 State University Dr, Los Angeles, California 90032, USA*
[69]*INFN, Sezione di Genova, I-16146 Genova, Italy*
[70]*OzGrav, University of Western Australia, Crawley, Western Australia 6009, Australia*
[71]*RRCAT, Indore, Madhya Pradesh 452013, India*
[72]*GRAPPA, Anton Pannekoek Institute for Astronomy and Institute for High-Energy Physics,*
University of Amsterdam, Science Park 904, 1098 XH Amsterdam, Netherlands
[73]*Missouri University of Science and Technology, Rolla, Missouri 65409, USA*
[74]*Faculty of Physics, Lomonosov Moscow State University, Moscow 119991, Russia*
[75]*Università di Trento, Dipartimento di Fisica, I-38123 Povo, Trento, Italy*
[76]*INFN, Trento Institute for Fundamental Physics and Applications, I-38123 Povo, Trento, Italy*
[77]*SUPA, University of the West of Scotland, Paisley PA1 2BE, United Kingdom*
[78]*Bar-Ilan University, Ramat Gan, 5290002, Israel*
[79]*Artemis, Université Côte d'Azur, Observatoire de la Côte d'Azur, CNRS, F-06304 Nice, France*
[80]*Dipartimento di Fisica "E.R. Caianiello", Università di Salerno, I-84084 Fisciano, Salerno, Italy*

[81]*INFN, Sezione di Napoli, Gruppo Collegato di Salerno,*
Complesso Universitario di Monte S. Angelo, I-80126 Napoli, Italy
[82]*Università di Roma "La Sapienza", I-00185 Roma, Italy*
[83]*Univ Rennes, CNRS, Institut FOTON—MR6082, F-3500 Rennes, France*
[84]*Indian Institute of Technology Bombay, Powai, Mumbai 400 076, India*
[85]*INFN, Laboratori Nazionali del Gran Sasso, I-67100 Assergi, Italy*
[86]*Laboratoire Kastler Brossel, Sorbonne Université, CNRS, ENS-Université PSL,*
Collège de France, F-75005 Paris, France
[87]*Astronomical Observatory Warsaw University, 00-478 Warsaw, Poland*
[88]*University of Maryland, College Park, Maryland 20742, USA*
[89]*Max Planck Institute for Gravitational Physics (Albert Einstein Institute), D-14476 Potsdam, Germany*
[90]*L2IT, Laboratoire des 2 Infinis—Toulouse, Université de Toulouse, CNRS/IN2P3,*
UPS, F-31062 Toulouse Cedex 9, France
[91]*School of Physics, Georgia Institute of Technology, Atlanta, Georgia 30332, USA*
[92]*IGFAE, Campus Sur, Universidade de Santiago de Compostela, 15782 Spain*
[93]*The Chinese University of Hong Kong, Shatin, Hong Kong*
[94]*Stony Brook University, Stony Brook, New York 11794, USA*
[95]*Center for Computational Astrophysics, Flatiron Institute, New York, New York 10010, USA*
[96]*NASA Goddard Space Flight Center, Greenbelt, Maryland 20771, USA*
[97]*Dipartimento di Fisica, Università degli Studi di Genova, I-16146 Genova, Italy*
[98]*Institute for Gravitational and Subatomic Physics (GRASP), Utrecht University,*
Princetonplein 1, 3584 CC Utrecht, Netherlands
[99]*RESCEU, University of Tokyo, Tokyo, 113-0033, Japan*
[100]*OzGrav, University of Melbourne, Parkville, Victoria 3010, Australia*
[101]*Università degli Studi di Sassari, I-07100 Sassari, Italy*
[102]*INFN, Laboratori Nazionali del Sud, I-95125 Catania, Italy*
[103]*Università di Roma Tor Vergata, I-00133 Roma, Italy*
[104]*INFN, Sezione di Roma Tor Vergata, I-00133 Roma, Italy*
[105]*University of Sannio at Benevento, I-82100 Benevento, Italy and INFN,*
Sezione di Napoli, I-80100 Napoli, Italy
[106]*Villanova University, 800 Lancaster Ave, Villanova, Pennsylvania 19085, USA*
[107]*Departamento de Astronomía y Astrofísica, Universitat de València,*
E-46100 Burjassot, València, Spain
[108]*Universität Hamburg, D-22761 Hamburg, Germany*
[109]*Rochester Institute of Technology, Rochester, New York 14623, USA*
[110]*National Tsing Hua University, Hsinchu City, 30013 Taiwan, Republic of China*
[111]*OzGrav, Charles Sturt University, Wagga Wagga, New South Wales 2678, Australia*
[112]*OzGrav, Swinburne University of Technology, Hawthorn, Victoria 3122, Australia*
[113]*CaRT, California Institute of Technology, Pasadena, California 91125, USA*
[114]*Dipartimento di Ingegneria Industriale (DIIN), Università di Salerno, I-84084 Fisciano, Salerno, Italy*
[115]*Université Lyon, Université Claude Bernard Lyon 1, CNRS, IP2I Lyon / IN2P3,*
UMR 5822, F-69622 Villeurbanne, France
[116]*Seoul National University, Seoul 08826, South Korea*
[117]*Pusan National University, Busan 46241, South Korea*
[118]*INAF, Osservatorio Astronomico di Padova, I-35122 Padova, Italy*
[119]*University of Arizona, Tucson, Arizona 85721, USA*
[120]*Rutherford Appleton Laboratory, Didcot OX11 0DE, United Kingdom*
[121]*Université libre de Bruxelles, Avenue Franklin Roosevelt 50–1050 Bruxelles, Belgium*
[122]*Universitat de les Illes Balears, IAC3—IEEC, E-07122 Palma de Mallorca, Spain*
[123]*Université Libre de Bruxelles, Brussels 1050, Belgium*
[124]*Departamento de Matemáticas, Universitat de València, E-46100 Burjassot, València, Spain*
[125]*Texas Tech University, Lubbock, Texas 79409, USA*
[126]*The Pennsylvania State University, University Park, Pennsylvania 16802, USA*
[127]*University of Rhode Island, Kingston, Rhode Island 02881, USA*
[128]*The University of Texas Rio Grande Valley, Brownsville, Texas 78520, USA*
[129]*Bellevue College, Bellevue, Washington 98007, USA*
[130]*Scuola Normale Superiore, Piazza dei Cavalieri, 7–56126 Pisa, Italy*
[131]*MTA-ELTE Astrophysics Research Group, Institute of Physics, Eötvös University,*
Budapest 1117, Hungary
[132]*University of Szeged, Dóm tér 9, Szeged 6720, Hungary*

[133]*Maastricht University, P.O. Box 616, 6200 MD Maastricht, Netherlands*
[134]*University of Portsmouth, Portsmouth, PO1 3FX, United Kingdom*
[135]*The University of Sheffield, Sheffield S10 2TN, United Kingdom*
[136]*Université Lyon, Université Claude Bernard Lyon 1, CNRS, Laboratoire des Matériaux Avancés (LMA), IP2I Lyon / IN2P3, UMR 5822, F-69622 Villeurbanne, France*
[137]*Dipartimento di Scienze Matematiche, Fisiche e Informatiche, Università di Parma, I-43124 Parma, Italy*
[138]*INFN, Sezione di Milano Bicocca, Gruppo Collegato di Parma, I-43124 Parma, Italy*
[139]*Indian Institute of Technology Madras, Chennai 600036, India*
[140]*Physik-Institut, University of Zurich, Winterthurerstrasse 190, 8057 Zurich, Switzerland*
[141]*University of Chicago, Chicago, Illinois 60637, USA*
[142]*Université de Strasbourg, CNRS, IPHC UMR 7178, F-67000 Strasbourg, France*
[143]*West Virginia University, Morgantown, West Virginia 26506, USA*
[144]*Montclair State University, Montclair, New Jersey 07043, USA*
[145]*Colorado State University, Fort Collins, Colorado 80523, USA*
[146]*Institute for Nuclear Research, Hungarian Academy of Sciences, Bem t'er 18/c, H-4026 Debrecen, Hungary*
[147]*Department of Physics, University of Texas, Austin, Texas 78712, USA*
[148]*CNR-SPIN, c/o Università di Salerno, I-84084 Fisciano, Salerno, Italy*
[149]*Scuola di Ingegneria, Università della Basilicata, I-85100 Potenza, Italy*
[150]*Gravitational Wave Science Project, National Astronomical Observatory of Japan (NAOJ), Mitaka City, Tokyo 181-8588, Japan*
[151]*Observatori Astronòmic, Universitat de València, E-46980 Paterna, València, Spain*
[152]*The University of Utah, Salt Lake City, Utah 84112, USA*
[153]*Kenyon College, Gambier, Ohio 43022, USA*
[154]*Vrije Universiteit Amsterdam, 1081 HV, Amsterdam, Netherlands*
[155]*Vanderbilt University, Nashville, Tennessee 37235, USA*
[156]*Universiteit Gent, B-9000 Gent, Belgium*
[157]*Cornell University, Ithaca, New York 14850, USA*
[158]*University of British Columbia, Vancouver, British Columbia V6T 1Z4, Canada*
[159]*Tata Institute of Fundamental Research, Mumbai 400005, India*
[160]*INAF, Osservatorio Astronomico di Capodimonte, I-80131 Napoli, Italy*
[161]*The University of Mississippi, University, Mississippi 38677, USA*
[162]*University of Michigan, Ann Arbor, Michigan 48109, USA*
[163]*Texas A&M University, College Station, Texas 77843, USA*
[164]*Dipartimento di Fisica, Università di Trieste, I-34127 Trieste, Italy*
[165]*American University, Washington, District of Columbia 20016, USA*
[166]*Carleton College, Northfield, Minnesota 55057, USA*
[167]*University of California, Berkeley, California 94720, USA*
[168]*Maastricht University, 6200 MD, Maastricht, Netherlands*
[169]*Directorate of Construction, Services and Estate Management, Mumbai 400094, India*
[170]*Universiteit Antwerpen, Prinsstraat 13, 2000 Antwerpen, Belgium*
[171]*University of Białystok, 15-424 Białystok, Poland*
[172]*University of Southampton, Southampton SO17 1BJ, United Kingdom*
[173]*Chung-Ang University, Seoul 06974, South Korea*
[174]*Institut de Física d'Altes Energies (IFAE), Barcelona Institute of Science and Technology, and ICREA, E-08193 Barcelona, Spain*
[175]*University of Washington Bothell, Bothell, Washington 98011, USA*
[176]*Institute of Applied Physics, Nizhny Novgorod, 603950, Russia*
[177]*Ewha Womans University, Seoul 03760, South Korea*
[178]*Inje University Gimhae, South Gyeongsang 50834, South Korea*
[179]*Korea Astronomy and Space Science Institute, Daejeon 34055, South Korea*
[180]*National Institute for Mathematical Sciences, Daejeon 34047, South Korea*
[181]*Ulsan National Institute of Science and Technology, Ulsan 44919, South Korea*
[182]*Bard College, 30 Campus Rd, Annandale-On-Hudson, New York 12504, USA*
[183]*Institute of Mathematics, Polish Academy of Sciences, 00656 Warsaw, Poland*
[184]*National Center for Nuclear Research, 05-400 Świerk-Otwock, Poland*
[185]*Université de Montréal/Polytechnique, Montreal, Quebec H3T 1J4, Canada*
[186]*Laboratoire Lagrange, Université Côte d'Azur, Observatoire Côte d'Azur, CNRS, F-06304 Nice, France*

[187]*Sungkyunkwan University, Seoul 03063, South Korea*
[188]*NAVIER, École des Ponts, Univ Gustave Eiffel, CNRS, Marne-la-Vallée, France*
[189]*Institute for High-Energy Physics, University of Amsterdam, Science Park 904, 1098 XH Amsterdam, Netherlands*
[190]*NASA Marshall Space Flight Center, Huntsville, Alabama 35811, USA*
[191]*University of Washington, Seattle, Washington 98195, USA*
[192]*Dipartimento di Matematica e Fisica, Università degli Studi Roma Tre, I-00146 Roma, Italy*
[193]*INFN, Sezione di Roma Tre, I-00146 Roma, Italy*
[194]*ESPCI, CNRS, F-75005 Paris, France*
[195]*Concordia University Wisconsin, Mequon, Wisconsin 53097, USA*
[196]*Università di Camerino, Dipartimento di Fisica, I-62032 Camerino, Italy*
[197]*School of Physics Science and Engineering, Tongji University, Shanghai 200092, China*
[198]*Southern University and A&M College, Baton Rouge, Louisiana 70813, USA*
[199]*Centre Scientifique de Monaco, 8 quai Antoine Ier, MC-98000, Monaco*
[200]*Saha Institute of Nuclear Physics, Bidhannagar, West Bengal 700064, India*
[201]*Institut des Hautes Etudes Scientifiques, F-91440 Bures-sur-Yvette, France*
[202]*Indian Institute of Science Education and Research, Kolkata, Mohanpur, West Bengal 741252, India*
[203]*Department of Astrophysics/IMAPP, Radboud University Nijmegen, P.O. Box 9010, 6500 GL Nijmegen, Netherlands*
[204]*Consiglio Nazionale delle Ricerche—Istituto dei Sistemi Complessi, Piazzale Aldo Moro 5, I-00185 Roma, Italy*
[205]*Hobart and William Smith Colleges, Geneva, New York 14456, USA*
[206]*International Institute of Physics, Universidade Federal do Rio Grande do Norte, Natal RN 59078-970, Brazil*
[207]*Museo Storico della Fisica e Centro Studi e Ricerche "Enrico Fermi", I-00184 Roma, Italy*
[208]*Lancaster University, Lancaster LA1 4YW, United Kingdom*
[209]*Università di Trento, Dipartimento di Matematica, I-38123 Povo, Trento, Italy*
[210]*Indian Institute of Science Education and Research, Pune, Maharashtra 411008, India*
[211]*Dipartimento di Fisica, Università degli Studi di Torino, I-10125 Torino, Italy*
[212]*Indian Institute of Technology, Palaj, Gandhinagar, Gujarat 382355, India*
[213]*Departamento de Matemática da Universidade de Aveiro and Centre for Research and Development in Mathematics and Applications, Campus de Santiago, 3810-183 Aveiro, Portugal*
[214]*Marquette University, 11420 W. Clybourn St., Milwaukee, Wisconsin 53233, USA*
[215]*Università di Firenze, Sesto Fiorentino I-50019, Italy*
[216]*INAF, Osservatorio Astrofisico di Arcetri, Largo E. Fermi 5, I-50125 Firenze, Italy*
[217]*Indian Institute of Technology Hyderabad, Sangareddy, Khandi, Telangana 502285, India*
[218]*INAF, Osservatorio di Astrofisica e Scienza dello Spazio, I-40129 Bologna, Italy*
[219]*Andrews University, Berrien Springs, Michigan 49104, USA*
[220]*Dipartimento di Scienze Aziendali—Management and Innovation Systems (DISA-MIS), Università di Salerno, I-84084 Fisciano, Salerno, Italy*
[221]*Van Swinderen Institute for Particle Physics and Gravity, University of Groningen, Nijenborgh 4, 9747 AG Groningen, Netherlands*
[222]*Vrije Universiteit Brussel, Boulevard de la Plaine 2, 1050 Ixelles, Belgium*
[223]*Vrije Universiteit Amsterdam, 1081 HV Amsterdam, Netherlands*

(Received 10 May 2022; accepted 13 June 2023; published 5 January 2024)

The second Gravitational-Wave Transient Catalog, GWTC-2, reported on 39 compact binary coalescences observed by the Advanced LIGO and Advanced Virgo detectors between 1 April 2019 15:00 UTC and 1 October 2019 15:00 UTC. Here, we present GWTC-2.1, which reports on a deeper list of candidate events observed over the same period. We analyze the final version of the strain data over this period with improved calibration and better subtraction of excess noise, which has been publicly released. We employ three matched-filter search pipelines for candidate identification, and estimate the probability of astrophysical origin for each candidate event. While GWTC-2 used a false alarm rate threshold of 2 per year, we include in GWTC-2.1, 1201 candidates that pass a false alarm rate threshold of 2 per day. We calculate the source properties of a subset of 44 high-significance candidates that have a probability of astrophysical origin greater than 0.5. Of these candidates, 36 have been reported in GWTC-2. We also

---

[*]Deceased, August 2020.

calculate updated source properties for all binary black hole events previously reported in GWTC-1. If the eight additional high-significance candidates presented here are astrophysical, the mass range of events that are unambiguously identified as binary black holes (both objects $\geq 3M_\odot$) is increased compared to GWTC-2, with total masses from $\sim 14M_\odot$ for GW190924_021846 to $\sim 182M_\odot$ for GW190426_190642. Source properties calculated using our default prior suggest that the primary components of two new candidate events (GW190403_051519 and GW190426_190642) fall in the mass gap predicted by pair-instability supernova theory. We also expand the population of binaries with significantly asymmetric mass ratios reported in GWTC-2 by an additional two events (the mass ratio is less than 0.65 and 0.44 at 90% probability for GW190403_051519 and GW190917_114630 respectively), and find that two of the eight new events have effective inspiral spins $\chi_{\rm eff} > 0$ (at 90% credibility), while no binary is consistent with $\chi_{\rm eff} < 0$ at the same significance. We provide updated estimates for rates of binary black hole and binary neutron star coalescence in the local Universe.

DOI: 10.1103/PhysRevD.109.022001

I. INTRODUCTION

We are in the era of gravitational wave (GW) astronomy, started by the Advanced Laser Interferometer Gravitational-Wave Observatory (LIGO) [1] and the Advanced Virgo [2] detectors. The first observing run (O1) of the advanced detectors yielded the first detection of GWs from a binary black hole (BBH), GW150914 [3]. By the end of O1, the LIGO Scientific and Virgo Collaboration (LVC) had reported on three BBH events [4]. The second observing run (O2) of the advanced detectors saw the first direct detection of GWs from a binary neutron star (BNS), GW170817 [5]. This event was also detected in electromagnetic waves [6], expanding the field of multimessenger astronomy to include GWs. By the end of O2, the LVC had reported on a total of ten BBHs and one BNS event, described in the first Gravitational-Wave Transient Catalog, GWTC-1 [7]. The second Gravitational-Wave Transient Catalog, GWTC-2 [8], added 39 GW events from the first half of the third observing run (O3a), and included a total of 50 events. The GW data until the end of third observing run (O3) have been made available to the public by the LVC. Since the public release of the LIGO and Virgo data, groups other than the LVC have also performed analyses searching for GW signals [9–21] and reported additional candidate events in some cases.

GW events between 1 April 2019 15:00 UTC and 1 October 2019 15:00 UTC (O3a) that passed a false alarm rate (FAR) threshold of 2 per year were presented in GWTC-2. Here, we present GWTC-2.1, a deep catalog that includes 1201 candidates passing a low-significance FAR threshold of 2 per day. Although most of the candidates in this catalog are noise events, they can be used for multimessenger searches by comparing against other astronomical surveys. Temporal and spatial coincidences between candidates in distinct astrophysical channels could lead to multimessenger discoveries [22,23]. Multimessenger observations could enhance our understanding of the physical processes associated with such systems. Previous GW searches, both from the LVC [24] and independent groups [10,13,14,24,25], including the 3-OGC analysis of public data from O1 to O3a [17], have released subthreshold candidates. It is computationally unfeasible to determine detailed source properties of the large set of subthreshold GW candidates, therefore we identify a subset of compact binary coalescence (CBC) candidates that have a probability of astrophysical origin $p_{\rm astro}$ [26–28] greater than 0.5, and calculate the source properties of these events. This probability $p_{\rm astro}$ uses both the signal rate in addition to the noise rate in order to determine the significance of events. There are 44 such candidate events, 36 of which have already been reported in GWTC-2 and their source properties have been described in detail [8]. We present the source properties with a consistent set of state-of-the-art waveform models for all of these candidates, discussing the properties of the eight new events that have a $p_{\rm astro}$ greater than 0.5 in detail in the body of the paper, and our results for the previously reported candidates in the Appendix. A subset of the eight additional events have been found in the LVC search of O3a data [29] for faint gravitationally lensed counterpart images [30,31], and in the independent 3-OGC [17] analysis. While the eight new events presented here have a non-negligible probability of being from noise, some of these have astrophysically interesting source properties under the default prior. Two of the new candidates presented here have a primary component mass in the pair instability gap [32–40], and one of those shows support for high spin and unequal masses. We also find a new candidate whose masses are consistent with a neutron star black hole binary (NSBH), although as in the case of GW190814 [41], we cannot rule out the possibility that the secondary component of the candidate could be a low-mass black hole.

In this work, all the analyses make use of the final version of the strain data with improved calibration and noise subtraction, which includes nonlinear subtraction around the 60 Hz frequency of the US power grid [42,43]. The data used in this work have been released to the public [44–47]. We use three matched-filter pipelines for candidate identification: GstLAL [48–50], PyCBC [51–55], and MBTA [56]. MBTA is reporting results from an archival search for the first time. Previously, in GWTC-2, only the GstLAL matched-filter pipeline included Virgo data; now all three pipelines analyze the data from all three detectors. For inferring the source properties, we use waveform models that include effects of spin-induced precession of the binary orbit, contributions from both the dominant and subdominant spherical harmonic modes, and tidal effects as appropriate [57–66].

The paper is structured as follows. Section II describes the instruments and the data that are analyzed by the searches, including methods on calibration, data quality, and glitch mitigation. Section III describes the methods used by the search pipelines. Section IV describes the events in GWTC-2.1, comparison to GWTC-2, sensitivity of the search pipelines used, and inferred rates of BNSs and BBHs. Section V describes the methods used for estimating the source parameters of the GW candidates and results, and in Sec. VI, we discuss the astrophysically interesting events and their implications. In Sec. VII we describe the data products being released alongside this catalog and our conclusions. Finally, in the Appendix, we provide the source properties of events with p_{astro} greater than 0.5 that have previously been described in GWTC-1 and GWTC-2. Companion results from the second half of the third observing run (O3b) are presented in the third Gravitational-Wave Transient Catalog, GWTC-3 [67].

II. INSTRUMENTS AND DATA

The Advanced LIGO [1] and Advanced Virgo [2] instruments are kilometer-scale laser interferometers. The two LIGO detectors are located in Hanford, Washington and Livingston, Louisiana in the United States, and the Virgo detector near Pisa in Italy. The advanced generation of interferometers began operations in 2015, and observing periods have alternated with commissioning periods since then [68]. In the time between O2 and the O3, all three detectors underwent significant upgrades that substantially increased their sensitivity [8,69].

Major instrumentation upgrades on the LIGO detectors included; replacement of main lasers to increase beam stability, replacement of test masses to lower scattering and absorption losses, installation of acoustic mode dampers to mitigate parametric instabilities [70], installation of a squeezed vacuum source to reduce quantum noise [71], addressing issues with scattered light [72], and implementation of improved feedback control systems for the instruments. Compared to the O2 run, the Hanford BNS range [51,73] increased by 64% (from 66 Mpc to 108 Mpc), and for Livingston by 53% (from 88 Mpc to 135 Mpc).

For Virgo, major upgrades included; replacement of the steel wire suspensions of the four test masses with fused-silica fibers [74], modification of the vacuum system to avoid dust contamination of the lowest suspension stage, replacement of the main laser to increase power, installation of a squeezed vacuum source to reduce quantum noise [75], improvements in beam stability [76], and addressing issues with scattered light. Compared to the O2 run, the Virgo BNS range increased by 73% (from 26 Mpc to 45 Mpc).

The processing of the data recorded by the LIGO and Virgo detectors includes several steps that occur both in near-real time to allow for the broadcasting of public alerts, and in higher latency to shape the final data set and update the catalogs of GW events. Raw data calibration and the subtraction of noise from known instrumental sources, documented in Sec. II A, occur first and the GW strain data, reconstructed independently in each detector, are then jointly processed. Significant GW candidates are vetted with several data-quality tests as a part of the standard analysis procedure. This procedure is described in Sec. II B.

A. Calibration and noise subtraction

The strain data used for astrophysical analyses is derived from the optical power variations at the output ports of the interferometers. Calibration of the raw photodetector signal to GW strain requires a detailed understanding and modeling of the control system and optomechanical response of the interferometers throughout an observing run. This allows for accurate and reliable calibration of the strain and also for quantifying its systematic and statistical uncertainty. The detailed procedure for the calibration and the determination of the systematic and statistical uncertainty of the LIGO and Virgo detectors for O3 can be found in [77–79].

There are usually two calibrations applied to the data; a low-latency calibration and, if needed, an offline calibration. The low-latency (online) estimate of the strain uses the best models of the detector at the time of recording. However, over the course of any observing run, data drop-outs due to computer failures, incomplete modeling of the detector, and unknown residual systematic errors are often identified. The offline calibration incorporates the necessary corrections and improvements, producing a better calibrated strain with better known systematic uncertainty.

In addition, numerous noise sources and calibration lines that limit detectors' sensitivity are measured and linearly subtracted from the data [42,80–82]. This subtraction is performed online to generate the LIGO and Virgo low-latency strain data, and it is also performed when regenerating the LIGO offline strain data. Additionally, noise due to nonstationary coupling of the power mains with the LIGO detectors was subtracted from the offline data [42]. As an example of noise subtraction, Fig. 1 shows the improvement in the noise levels around the 60 Hz mains line in the Hanford detector, after nonlinear noise subtraction was applied to the strain time series. Taking as a figure of merit the BNS range of the detectors [51,73], the subtraction results in a median range increase of 0.9 Mpc for Hanford and 0.2 Mpc for Livingston.

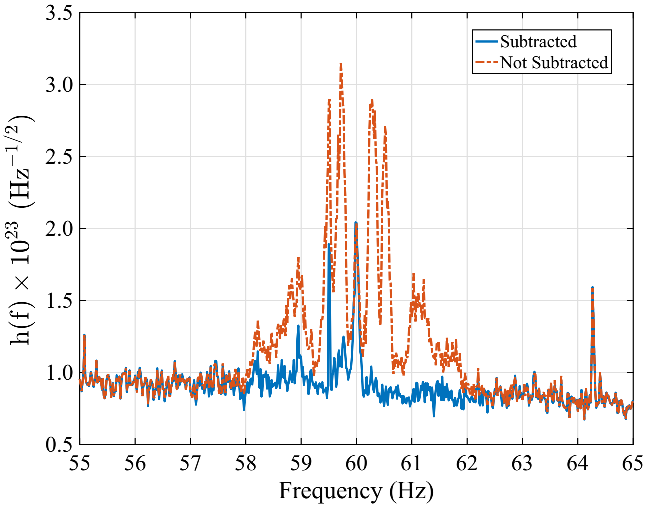

FIG. 1. Comparison of the amplitude spectral density at Hanford around the 60 Hz mains line, between data with subtracted nonstationary noise and data with no subtraction. The data correspond to a typical one-hour observation-ready data stretch during O3a.

In GWTC-2, search pipelines and parameter estimation analyses used a mix of low-latency and offline calibrated frames. In contrast to this, all searches and analyses presented in this paper use strain data with the best available calibration and noise subtraction for each detector. For LIGO, this corresponds to the offline recalibrated data with 60 Hz nonlinear subtraction. For Virgo, the online strain data stream was good enough to be used offline, except for the last two weeks of O3a which were reprocessed to improve subtraction of control and laser frequency noise [83]. The strain data used in this work are publicly accessible through the Gravitational Wave Open Science Center (GWOSC) [44,47].

In addition, the LIGO offline data are accompanied with a much improved systematic and statistical error estimate compared to the online data. The probability distribution of the calibration uncertainty estimate for LIGO in O3a is characterized in [77], with the systematic error over the detectors' bandwidth being under 3% in magnitude and under 2° in phase. The uncertainty in the Virgo strain data in O3a had a maximum systematic error over the detector's bandwidth under 5% in magnitude and under 2° in phase [78]. Parameter estimation takes into account calibration uncertainties, as described in Sec. V. Given the size of calibration uncertainties in O3, there is no evidence that they have a significant impact on the inference of source parameters [84,85].

B. Data quality, event validation and glitch mitigation

LIGO and Virgo data quality is continuously monitored during an observing run both on site and remotely, as reported in [86,87]. This can include, for example, internal detector summary pages which detail the status of the detectors and interferometer subsystems [88,89]. Feedback from GW searches also gives an indication of the impact of data quality on the sensitivity of a search. To exclude identified instances of poor data quality from the searches and produce the results in Sec. III, we used the same methods and data products as reported for GWTC-2 [8]. The data-quality products used in this work are publicly available [44,45].

TABLE I. List of candidate-specific data usage and mitigation methods for parameter estimates. Only candidate events for which mitigation of instrumental artifacts was performed are listed. The glitch-subtraction methods used for these candidate events are detailed in Sec. II B. The minimum frequency is the lower limit of data used in analyses of GW source properties for the listed interferometer.

Name	Mitigation
GW190413_134308	L1 glitch subtraction, glitch-only model
GW190425	L1 glitch subtraction, glitch-only model
GW190503_185404	L1 glitch subtraction, glitch-only model
GW190513_205428	L1 glitch subtraction, glitch-only model
GW190514_065416	L1 glitch subtraction, glitch-only model
GW190701_203306	L1 glitch subtraction, glitch + signal model
GW190727_060333	L1 f_{min}: 50 Hz
GW190814	L1 f_{min}: 30 Hz; H1 nonobserving data used
GW190924_021846	L1 glitch subtraction, glitch-only model

Once a GW event has been identified by the search pipelines, we check the quality of data around the time of the event. We followed the same procedures outlined in [8] to validate the data quality around each new GW candidate reported in this paper. The aim of these validation procedures is to identify any instrumental or environmental noise that may impact the estimation of GW signal parameters. As summarized for GWTC-2 [8], in some cases short-duration noise transients, or *glitches* [86,90–92], can be subtracted from the data [93–96]. When this is not possible, analyses use tailored configurations, for example, a modified low-frequency cutoff, to exclude data that could be corrupted by the presence of a nearby glitch. The full list of candidate events using candidate-specific glitch mitigation, along with the mitigation configuration, is found in Table I. These data, for the events where the glitch-mitigated data was used for the parameter estimation analysis in Sec. V, are publicly accessible [46]. No candidates in this catalog have clear evidence of instrumental origin identified through data-quality validation studies.

III. CANDIDATE IDENTIFICATION

GW data is analyzed to search for candidates in two stages; first in low-latency in order to generate public alerts that subsequently trigger followup astronomical observations, and then in higher latency in the form of an offline analysis of the archival strain data, which is used to create GW catalogs. Five pipelines were used in real time to analyze O3 data; a minimally modeled generic transient search (coherent WaveBurst [97–101]), and four matched-filter [51,52] pipelines (GstLAL [48–50], MBTA [56], PyCBC [53–55,102], and SPIIR [103]). Collectively, they identified 56 unretracted candidates during O3, 33 of which were found in O3a. GWTC-2 [8] presented 39 events identified by coherent WaveBurst, GstLAL, and PyCBC in the first offline search over O3a.

We present here results from a refined offline search of O3a. The search employs three matched-filter pipelines; GstLAL, PyCBC, and MBTA [56], marking the first time that MBTA results from archival data are presented and included in a GW catalog. All three pipelines analyze the data from all three detectors. While GWTC-2 imposed a FAR ceiling of 2 per year on candidates, here we release a deep list of GW candidates with a FAR smaller than 2 per day [104]. In addition, we identify the 44 CBC candidates with an estimated p_{astro} greater than 0.5 (Table II). There are also two candidates with p_{astro} below 0.5 that do meet the FAR criterion used in GWTC-2; these are presented as marginal candidates. This GW catalog contains the largest number of candidates with p_{astro} greater than 0.5 to date.

In Sec. III A, we first lay out a general description of matched filter searches and in Sec. III B, we describe the methods employed by the three CBC searches used in this work. We describe the search results in the following Sec. IV.

TABLE II. Above-threshold GW candidate list. We find 44 events that have p_{astro} in at least one of the searches as greater than 0.5. Bold-faced names indicate the events that were not previously reported in GWTC-2 [8]. The candidates marked with an asterisk were first published in 3-OGC [17]. The second column denotes the observing instruments. Candidate events in GWTC-2.1 which do not meet the p_{astro} threshold but were at the same time as above-threshold events are given in italics. The PyCBC and PyCBC -BBH, network SNRs do not include detectors with SNRs below 4; these events are marked with double dagger (‡) next to their network SNR. The four events marked with a dagger (†) next to their FARs were found only in one detector by the GstLAL search. All four were detected using the data from LIGO Livingston. For the single-detector candidate events, the FAR estimate involves extrapolation. All single-detector candidate events in this list according to the FAR assigned to them are rarer than the background data of about six months collected in this analysis. Therefore, a conservative bound on the FAR for candidates denoted by † is $\sim 2\ \mathrm{yr}^{-1}$. GstLAL FARs have been capped at $1 \times 10^{-5}\ \mathrm{yr}^{-1}$ to be consistent with the limiting FARs from other pipelines. Dashes indicate that a pipeline did not find the event with a FAR smaller than the subthreshold FAR threshold of 2 per day.

		MBTA			GstLAL			PyCBC			PyCBC-BBH,		
Name	Inst.	FAR (yr^{-1})	SNR	p_{astro}	FAR (yr^{-1})	SNR	p_{astro}	FAR (yr^{-1})	SNR	p_{astro}	FAR (yr^{-1})	SNR	p_{astro}
GW190403_051519	HLV	⋯	⋯	⋯	⋯	⋯	⋯	⋯	⋯	⋯	7.7	8.0	0.61
GW190408_181802	HLV	8.7×10^{-5}	14.4	1.00	$<1.0 \times 10^{-5}$	14.7	1.00	2.5×10^{-4}	13.1‡	1.00	$<1.2 \times 10^{-4}$	13.7‡	1.00
GW190412	HLV	$<1.0 \times 10^{-5}$	18.2	1.00	$<1.0 \times 10^{-5}$	19.0	1.00	$<1.1 \times 10^{-4}$	17.4‡	1.00	$<1.2 \times 10^{-4}$	17.9‡	1.00
GW190413_052954	HLV	⋯	⋯	⋯	⋯	⋯	⋯	170	*8.5*	*0.13*	0.82	8.5	0.93
GW190413_134308	HLV	0.34	10.3	0.99	39	*10.1*	*0.04*	21	*9.3*†	*0.48*	0.18	8.9‡	0.99
GW190421_213856	HL	1.2	9.7	0.99	0.0028	10.5	1.00	5.9	10.1	0.75	0.014	10.1	1.00
GW190425	LV	⋯	⋯	⋯	0.034†	12.9	0.78	⋯	⋯	⋯	⋯	⋯	⋯
GW190426_190642	HLV	⋯	⋯	⋯	⋯	⋯	⋯	⋯	⋯	⋯	4.1	9.6	0.75
GW190503_185404	HLV	0.013	12.8	1.00	$<1.0 \times 10^{-5}$	12.0	1.00	0.038	12.2‡	1.00	0.0026	12.2‡	1.00
GW190512_180714	HLV	0.038	11.7	0.99	$<1.0 \times 10^{-5}$	12.2	1.00	1.1×10^{-4}	12.4‡	1.00	$<1.1 \times 10^{-4}$	12.4‡	1.00
GW190513_205428	HLV	0.11	13.0	0.99	1.3×10^{-5}	12.3	1.00	19	*11.6*‡	*0.49*	0.044	11.8‡	1.00
GW190514_065416	HL	⋯	⋯	⋯	450	*8.3*	*0.00*	⋯	⋯	⋯	2.8	8.4	0.76
GW190517_055101	HLV	0.11	11.3	1.00	0.0045	10.8	1.00	0.0095	10.4‡	1.00	3.5×10^{-4}	10.3‡	1.00
GW190519_153544	HLV	7.0×10^{-5}	13.7	1.00	$<1.0 \times 10^{-5}$	12.4	1.00	$<1.0 \times 10^{-4}$	13.2‡	1.00	$<1.1 \times 10^{-4}$	13.2‡	1.00
GW190521	HLV	0.042	13.0	0.96	0.20	13.3	0.79	0.44	13.7‡	0.96	0.0013	13.6‡	1.00
GW190521_074359	HL	$<1.0 \times 10^{-5}$	22.2	1.00	$<1.0 \times 10^{-5}$	24.4	1.00	$<1.8 \times 10^{-5}$	24.0	1.00	$<2.3 \times 10^{-5}$	24.0	1.00
GW190527_092055	HL	⋯	⋯	⋯	0.23	8.7	0.85	⋯	⋯	⋯	19	*8.4*	*0.33*
GW190602_175927	HLV	3.0×10^{-4}	12.6	1.00	$<1.0 \times 10^{-5}$	12.3	1.00	0.29	11.9‡	0.98	0.013	11.9‡	1.00
GW190620_030421	LV	⋯	⋯	⋯	0.011‡	10.9	0.99	⋯	⋯	⋯	⋯	⋯	⋯
GW190630_185205	LV	⋯	⋯	⋯	$<1.0 \times 10^{-5}$	15.2	1.00	⋯	⋯	⋯	0.24	15.1	1.00
GW190701_203306	HLV	35	11.3	0.87	0.0057	11.7	0.99	0.064	11.9	0.99	0.56	11.7	1.00
GW190706_222641	HLV	0.0015	11.9	1.00	5.0×10^{-5}	12.5	1.00	3.7×10^{-4}	11.7‡	1.00	0.34	12.6‡	1.00
GW190707_093326	HL	0.032	12.6	1.00	$<1.0 \times 10^{-5}$	13.2	1.00	$<1.0 \times 10^{-5}$	13.0	1.00	$<1.9 \times 10^{-5}$	13.0	1.00
GW190708_232457	LV	⋯	⋯	⋯	$3.1 \times 10^{-4\dagger}$	13.1	1.00	⋯	⋯	⋯	⋯	⋯	⋯
GW190719_215514	HL	⋯	⋯	⋯	⋯	⋯	⋯	⋯	⋯	⋯	0.63	8.0	0.92

(Table continued)

TABLE II. *(Continued)*

		MBTA			GstLAL			PyCBC			PyCBC-BBH,		
Name	Inst.	FAR (yr^{-1})	SNR	p_{astro}	FAR (yr^{-1})	SNR	p_{astro}	FAR (yr^{-1})	SNR	p_{astro}	FAR (yr^{-1})	SNR	p_{astro}
GW190720_000836	HLV	0.094	11.6	1.00	$<1.0\times10^{-5}$	11.5	1.00	1.4×10^{-4}	$10.6^{\ddagger}$	1.00	$<7.8\times10^{-5}$	11.4	1.00
GW190725_174728 *	HLV	3.1	9.8	0.59	⋯	⋯	⋯	0.46	$9.1^{\ddagger}$	0.96	2.9	$8.8^{\ddagger}$	0.82
GW190727_060333	HLV	0.023	12.0	1.00	$<1.0\times10^{-5}$	12.1	1.00	0.0056	$11.4^{\ddagger}$	1.00	2.0×10^{-4}	$11.1^{\ddagger}$	1.00
GW190728_064510	HLV	7.5×10^{-4}	13.1	1.00	$<1.0\times10^{-5}$	13.4	1.00	$<8.2\times10^{-5}$	$13.0^{\ddagger}$	1.00	$<7.8\times10^{-5}$	$13.0^{\ddagger}$	1.00
GW190731_140936	HL	6.1	9.1	0.80	0.33	8.5	0.78	⋯	⋯	⋯	1.9	7.8	0.83
GW190803_022701	HLV	77	9.0	0.96	0.073	9.1	0.94	81	*8.7*‡	*0.17*	0.39	$8.7^{\ddagger}$	0.97
GW190805_211137	HLV	⋯	⋯	⋯	⋯	⋯	⋯	⋯	⋯	⋯	0.63	8.3	0.95
GW190814	LV	$<2.0\times10^{-4}$	20.4	1.00	$<1.0\times10^{-5}$	22.2	1.00	0.17	19.5	1.00	⋯	⋯	⋯
GW190828_063405	HLV	$<1.0\times10^{-5}$	15.2	1.00	$<1.0\times10^{-5}$	16.3	1.00	$<8.5\times10^{-5}$	$13.9^{\ddagger}$	1.00	$<7.0\times10^{-5}$	$15.9^{\ddagger}$	1.00
GW190828_065509	HLV	0.16	10.8	0.96	3.5×10^{-5}	11.1	1.00	2.8×10^{-4}	$10.5^{\ddagger}$	1.00	1.1×10^{-4}	$10.5^{\ddagger}$	1.00
GW190910_112807	LV	⋯	⋯	⋯	$0.0029^{\ddagger}$	13.4	1.00	⋯	⋯	⋯	⋯	⋯	⋯
GW190915_235702	HLV	0.0055	12.7	1.00	$<1.0\times10^{-5}$	13.0	1.00	6.8×10^{-4}	$13.0^{\ddagger}$	1.00	$<7.0\times10^{-5}$	$13.1^{\ddagger}$	1.00
GW190916_200658 *	HLV	6.9×10^{3}	8.2	0.66	12	*8.2*	*0.09*	⋯	⋯	⋯	4.7	7.9	0.64
GW190917_114630	HLV	⋯	⋯	⋯	0.66	9.5	0.77	⋯	⋯	⋯	⋯	⋯	⋯
GW190924_021846	HLV	0.0049	11.9	0.99	$<1.0\times10^{-5}$	13.0	1.00	$<8.2\times10^{-5}$	$12.4^{\ddagger}$	1.00	8.3×10^{-5}	$12.5^{\ddagger}$	1.00
GW190925_232845 *	HV	100	*9.4*	*0.35*	⋯	⋯	⋯	73	*9.0*	*0.02*	0.0072	9.9	0.99
GW190926_050336 *	HLV	⋯	⋯	⋯	1.1	9.0	0.54	⋯	⋯	⋯	87	*7.8*‡	*0.09*
GW190929_012149	HLV	2.9	10.3	0.6	4 0.16	10.1	0.87	120	*9.4*‡	*0.14*	14	*8.5*‡	*0.41*
GW190930_133541	HL	0.34	10.0	0.87	0.43	10.1	0.76	0.018	9.8	1.00	0.012	10.0	1.00

A. Matched-filter searches

The matched-filter method relies on having a model of the signal, as a function of the physical parameters. The parameters include those that are intrinsic to the source; two individual component masses m_1, m_2 and two dimensionless-spin vectors $\vec{\chi}_1,\vec{\chi}_2$ [related to each component's spin angular momentum $\vec{S}_i$ by $\vec{\chi}_i = c\vec{S}_i/(Gm_i^2)$], and seven extrinsic parameters that provide the orientation and position of the source in relation to the Earth; the luminosity distance D_{L}, two-dimensional sky position (right ascension α and declination δ), inclination between total angular momentum and line-of-sight θ_{JN}, time of merger t_{c}, a reference phase ϕ, and polarization angle ψ. The search pipelines create a template bank [105–107] of GW waveforms covering the desired intrinsic parameter space, and use these to filter against the data and produce signal-to-noise ratio (SNR) time series. The component masses describing template waveforms are affected by source redshift z as $m_i^{\mathrm{det}} = (1+z)m_i$.

For each set of intrinsic parameters, extrinsic parameters affecting the signal's amplitude and phase may be maximized over analytically [51], if the signal can be approximated as a pure quadrupole mode, i.e. $(\ell, |m|) = (2,2)$. In particular, for this search, the templates use only the dominant quadrupole mode and assume quasicircular orbits with component spins aligned with the total orbital angular momentum. Peaks in the resulting SNR time series are stored as triggers. GW candidates are formed by imposing consistency in time and in template intrinsic parameters between triggers in different detectors; in addition, GstLAL also considers noncoincident triggers as candidates [48].

When considering a single template in a single detector with stationary, Gaussian noise, the matched filter SNR is an optimal statistic for ranking candidates. However, additional terms are needed to optimize sensitivity in searches of real data covering a wide signal parameter space. To account for the multidetector network, the distribution of signals over relative times, phases and amplitudes between detectors is considered [49,55]. Since detector noise is not stationary or Gaussian, signal-consistency tests such as chi-squared [52] are calculated and used to rank candidates.

The distribution of noise triggers may vary strongly over the template masses and spins; we then model its variation empirically, as a function of combinations of parameters that are typically well-constrained by GW measurements. The binary's chirp mass [108],

$$\mathcal{M} = \frac{(m_1 m_2)^{3/5}}{(m_1 + m_2)^{1/5}}, \tag{1}$$

determines to lowest order the phase evolution during the inspiral, and is typically better constrained than the component masses. At higher orders, the binary phase evolution is affected by the mass ratio $q = m_2/m_1$ (where $m_2 \leq m_1$) and by the effective inspiral spin χ_{eff}, defined as [109]

$$\chi_{\mathrm{eff}} = \frac{(m_1\vec{\chi}_1 + m_2\vec{\chi}_2)\cdot\hat{L}_{\mathrm{N}}}{M}, \tag{2}$$

TABLE III. Source probabilities (p_{BBH}, p_{BNS}, p_{NSBH}) for the high significance GW candidates listed in Table II for which p_{BNS} or p_{NSBH} is greater than 1%. For other events in Table II, $p_{\mathrm{astro}} \approx p_{\mathrm{BBH}}$, and therefore we do not list them here. Results are provided from all three matched-filter pipelines. Dashes indicate that a pipeline did not find the event with a FAR smaller than the subthreshold FAR threshold of 2 per day. The classification provided here assumes a boundary of $3M_{\odot}$ between NSs and BHs in the case of GstLAL and PyCBC, and $2.5M_{\odot}$ in the case of MBTA.

Name	MBTA				GstLAL				PyCBC				PyCBC-BBH,		
	p_{BBH}	p_{NSBH}	p_{BNS}	p_{astro}	p_{BBH}	p_{NSBH}	p_{BNS}	p_{astro}	p_{BBH}	p_{NSBH}	p_{BNS}	p_{astro}	p_{BBH}	p_{NSBH}	p_{astro}
GW190425	⋯	⋯	⋯	⋯	0.00	0.00	0.78	0.78	⋯	⋯	⋯	⋯	⋯	⋯	⋯
GW190707_093326	1.00	0.00	0.00	1.00	1.00	0.00	0.00	1.00	0.93	0.07	0.00	1.00	0.93	0.07	1.00
GW190720_000836	1.00	0.00	0.00	1.00	1.00	0.00	0.00	1.00	0.95	0.05	0.00	1.00	1.00	0.00	1.00
GW190725_174728	0.59	0.00	0.00	0.59	⋯	⋯	⋯	⋯	0.79	0.17	0.00	0.96	0.58	0.24	0.82
GW190728_064510	1.00	0.00	0.00	1.00	1.00	0.00	0.00	1.00	0.97	0.03	0.00	1.00	0.97	0.03	1.00
GW190814	0.93	0.07	0.00	1.00	0.19	0.81	0.00	1.00	0.54	0.46	0.00	1.00	⋯	⋯	⋯
GW190924_021846	0.92	0.07	0.00	0.99	1.00	0.00	0.00	1.00	0.44	0.56	0.00	1.00	0.44	0.56	1.00
GW190930_133541	0.87	0.00	0.00	0.87	0.76	0.00	0.00	0.76	0.93	0.07	0.00	1.00	0.85	0.15	1.00

where $M = m_1 + m_2$ is the total mass and $\hat{L}_{\mathrm{N}}$ is the unit vector along the Newtonian orbital angular momentum. Finally, the ranking of events by the search pipelines may account for an assumed prior distribution of signals over masses and spins [110,111].

The significance of each candidate event is quantified by its FAR, the estimated rate of events due to noise with equal or higher ranking statistic value. The FAR is calculated by each search pipeline by constructing a set of background samples designed to have the same distribution over ranking statistic as search events in the absence of binary merger GW signals.

By considering also the expected distribution of GW signal events recovered by a given search, we may derive an estimate of the relative probabilities of noise (terrestrial) origin p_{terr}, and signal (astrophysical) origin p_{astro} [26–28]. For the bulk of released events, detailed estimates of source parameters are not calculated. Therefore, based only on the matched-filter search results we also estimate the probability for each event to belong to three possible astrophysical binary source classes, labeled BNS, NSBH, and BBH. The classes are defined by binary component masses; BNS corresponds to $\{m_1, m_2\} < 3M_{\odot}$, NSBH to $m_1 > 3M_{\odot}$, $m_2 < 3M_{\odot}$, and BBH to $\{m_1, m_2\} > 3M_{\odot}$. For MBTA, a $2.5M_{\odot}$ cut is used instead of $3M_{\odot}$, with a gap to $5M_{\odot}$ for BBH. These definitions are chosen for simplicity: they *do not* imply that every binary component within a given mass range is necessarily a neutron star (NS) or a black hole (BH). Such inference would ultimately require measurement of the effects of NS matter on observed signals, which is beyond the capabilities of the search pipelines. The probabilities for an event to belong to each class (p_{BNS}, p_{NSBH}, p_{BBH}, and p_{terr}) are calculated from the template masses and spins recovered by the searches, under the assumption that events from each class occur as independent Poisson processes. The calculation also requires the choice of a prior on the event counts in each category [28]. GstLAL used a uniform prior for the BNS and NSBH categories, and a Poisson-Jeffreys prior for the BBH category; MBTA used a uniform prior for the BNS category, and a Poisson-Jeffreys prior for the NSBH and BBH categories; and PyCBC used a Poisson-Jeffreys prior for all three categories. Given the number of candidates, the prior choice does not significantly impact the BBH results. Implementation details differ between pipelines, as summarized below; the resulting probability estimates are listed in Tables II and III.

While the p_{astro} values given here represent our best estimates of the origin of candidates using the information available from search pipelines, they are subject to statistical (random) and systematic errors, as well as in some cases clearly differing for a given candidate between different pipelines. One such uncertainty arises from methods used to rank events between pipelines, including tests for noise artifacts; such tests, such as chi-squared statistics, will in general add (different) random variations to the ranking of a given event, in addition to their differing power in distinguishing signals from artifacts. For single-detector candidates, there is an additional inherent uncertainty in estimating the rate of comparable noise events, which may only be bounded to (less than) 1 per observing time. An inherent source of potential systematic error also lies in the search ranking statistic used in the calculation of p_{astro}; such statistics are optimized to detect a specific (usually broad) distribution of signals over binary intrinsic parameters. The resulting p_{astro} estimates may be biased if this distribution deviates significantly from the (unknown) true signal distribution. The risk of such bias is largest for regions of parameter space containing few, or zero, confirmed detections. For all these reasons, our current p_{astro} values may be revised in the future, particularly as and when current uncertainties in the true signal rate and distributions are eventually reduced.

We next review specific methods used by individual matched-filter pipelines.

B. Search pipelines

In this section we describe the pipelines that were used to identify the candidates presented in GWTC-2.1.

1. GstLAL

The GstLAL analysis used in this search is similar to the one used in the previous analysis for GWTC-2 [8]. The template bank used in this analysis is identical to the one used by GstLAL for GWTC-2 [8]. It covers waveforms with redshifted total masses from $2M_\odot$ to $758M_\odot$, and spins that are aligned or antialigned with the binary's orbital angular momentum. The template bank is constructed using a stochastic placement method in five different regions of the parameter space [8]. The ranking statistic used by the analysis is the log-likelihood ratio $\mathcal{L}$ used in the previous analysis [8]. Improvements have been made to the input data products generated by iDQ, the statistical inference framework to autonomously detect non-Gaussian noise artifacts in strain data based on auxiliary witness sensors [112,113]. This iDQ timeseries is used to compute one of the terms in the log-likelihood ratio within the GstLAL analysis, that informs the search of the presence of non-Gaussian noise in close proximity to a GW candidate. Compared to GWTC-2, the timeseries generated by iDQ was reprocessed offline, having access to an expanded set of auxiliary witness sensors and trained with an acausal binning scheme [112]. As a result, the generated iDQ timeseries performs better in identifying noise artifacts in strain data. In addition, for GWTC-2 the iDQ term was only used when ranking single-detector triggers, whereas now it is used for both coincident and single-detector triggers. Because of changes in the iDQ term, the empirically determined penalty for single-detector candidates had to be retuned compared to GWTC-2, and was increased to a penalty of $\Delta\mathcal{L} = -12$ from $\Delta\mathcal{L} = -10$. The single-detector event penalty is determined by comparing the recovery of simulated signals in single detector versus combinations of detectors and the sensitive volume-time for each configuration.

For the GstLAL analysis, p_{terr} and p_{astro} shown in Tables II and III are estimated following the multicomponent population analysis [26,114]. The response of each GstLAL template to each astrophysical source class, computed semi-analytically [111], is used in estimating these probabilities. The volume–time sensitivity of the pipeline used in this calculation is estimated based on simulated sources injected into the pipeline and is rescaled to the astrophysical distribution [115]. The volume-time ratios are used to combine triggers from various observation runs and perform a multicomponent analysis yielding p_{astro} and merger rates [26,114] inferred from O1 to O3a. The astrophysical distribution assumed in this analysis uses a log-uniform distribution for the source component masses, the component spins aligned with the orbital angular momentum, and a uniform distribution for the component spin magnitudes. The BH masses in BBHs and NSBHs are distributed between $3M_\odot$ and $300M_\odot$ with aligned component spins distributed in the range $[-0.99, 0.99]$. The NS masses in NSBHs and BNSs are distributed between $1M_\odot$ and $3M_\odot$. In NSBHs, the NS spins are assumed to be aligned and distributed in the range $[-0.4, 0.4]$, whereas, in BNSs the NSs are assumed to have small spins in the range $[-0.05, 0.05]$. These choices match previous analyses [8].

2. MBTA

The Multiband Template Analysis (MBTA) pipeline [56] is based on matched filtering, relying on coincidences between triggers observed in different detectors. The version used for the offline search is close to the online version which contributed to the LVC public alerts [116]. The archival-search version benefits from offline-specific improvements, with a background estimate made over a longer duration, and with a reranking of the candidates using information collected not just before but also after the candidate.

The parameter space covered by this analysis ranges from $1M_\odot$ to $195M_\odot$ for the primary (more massive) component, with total masses up to $200M_\odot$; or from $1M_\odot$ to $100M_\odot$ for the primary when the mass of the secondary is between $1M_\odot$ and $2M_\odot$. Component spins are aligned with the total angular momentum and are limited to 0.05 for objects below $2M_\odot$, and going up to 0.997 for objects above $2M_\odot$. The waveform used for the search is SpinTaylorT4 [117–119] if both binary masses are lighter than $2M_\odot$, and SEOBNRv4 [120] if the mass of one of the components is above $2M_\odot$. The total number of templates in the bank used is 727,992. The SNR threshold for recording triggers in each detector is 4.5, or 4.8 if one of the components is above $2M_\odot$.

The FAR is calculated for each coincident event by forming random coincidences among single detector background triggers. This computation is performed independently for three large regions of the parameter space bounded by a $2M_\odot$ limit for the mass of each component. These three regions are allowed to contribute equally to the background, while within each of them we sum the background contributions from all the templates.

The p_{BNS}, p_{NSBH}, p_{BBH}, and derived p_{astro} quantities are computed as the fraction of recovered simulated events, representative of an astrophysical population, to this foreground plus background estimate provided by the pipeline [121]. The parametrizations of the populations are described in Sec. IV D, with the POWER LAW + PEAK model used for BBH [122]. The rate of each type of source is adjusted using a multicomponent population analysis [26]. To follow the population and background evolution across the parameter space, 165 subregions are used. This finer resolution has the benefit of revealing events in population-rich areas, even if the overall background rate for their ranking statistic value is larger than few per year, as in the case of the high-mass BBH event GW190916_200658 presented in Table II.

3. PyCBC

In previous LVC searches [4,7,8,123], the offline PyCBC [54,124] pipeline has analyzed data only from the two LIGO detectors. In this analysis, PyCBC was extended to search data from the three-detector LIGO-Virgo network, along with updates to the event ranking statistic [102] and the $p_{\rm astro}$ calculation and a new method to estimate source-class probability [125].

The PyCBC search uses the same template bank as in GWTC-2 [8], constructed using a hybrid geometric-random algorithm outlined in [126,127]. Peaks in SNR time series exceeding a threshold of four constitute single-detector triggers. Two-detector coincident events are formed from triggers with the same component masses and spins with a physically allowed time difference between detectors, allowing for timing errors. Three-detector triple coincidences require triggers in all pairs of detectors to pass this consistency test.

The detection statistic is given by the logarithm of the ratio of estimated signal-event rate density to noise-event rate density. We model the noise distribution in each detector as a decreasing exponential of the matched-filter SNR, reweighted based on a chi-squared signal-glitch discriminator [52,128], with parameters that depend on the template intrinsic parameters. The signal distribution includes terms accounting for dependence on relative times of arrival, phases and amplitudes between detectors, as well as relative sensitivities of the participating detectors [55]. We estimate the FAR separately for each combination of detectors via time-shifted analyses [54,129]. The significance for each candidate event is then found through addition of the FARs at the candidate's ranking statistic value over all active detector combinations [102].

In addition to the generic PyCBC search, which covers the full parameter space [8] including a range of possible signal types, we also conduct a focused PyCBC BBH search [8,14], capable of uncovering fainter BBH mergers by imposing a prior form for the signal distribution over the template bank [110]. This search is targeted at systems with mass ratios from 1 to $1/3$, primary component masses from $5M_\odot$ to $350M_\odot$, and aligned, equal component spins from $\chi = -0.998$ to 0.998.

The inference of $p_{\rm astro}$ and $p_{\rm terr}$ for each candidate event employs a Poisson mixture model of signal and noise events [26–28]. Here, the distribution of signal events is estimated via a set of simulated signals analyzed by the pipeline, and the rate and distribution of noise events are estimated from time-shifted analyses [54]. In GWTC-2 the calculation was only performed on potential BBH events with template chirp mass above $4.35M_\odot$ (which corresponds to equal $5M_\odot$ component masses). Here, we include potential BNS and NSBH events by performing independent calculations over ranges of template chirp mass below $2.18M_\odot$ (corresponding to equal $2.5M_\odot$ components), and between $2.18M_\odot$–$4.35M_\odot$, respectively. Although the implied signal distribution over template chirp mass does not correspond to any specific astrophysical model, it is adequate for assignment of $p_{\rm astro}$ given the current knowledge of BNS and NSBH merger populations. Systematic biases in $p_{\rm astro}$ calculation may arise if the (unknown) true mass distribution is different from that assumed. The calculation is also extended relative to previous analyses to account for different possible coincident combinations of detectors [130]. The results given here are obtained from events occurring during O3a only, except for the BNS region where prior information of one highly significant detection was applied to represent GW170817 [5].

The estimation method for binary source-class probabilities [125] uses the binary chirp mass as input, and assumes a uniform density of candidate signals over the plane of component masses $\{m_1, m_2\}$. Here we take the classes to be defined by boundaries between different types of binary component at $3M_\odot$. To estimate source chirp mass, we correct the search template masses for cosmological redshift, using an estimate of the luminosity distance derived from the search SNRs and the corresponding templates' sensitivity. We then derive the relative probabilities of each source class and enforce that the sum of astrophysical source probabilities is equal to $p_{\rm astro}$.

IV. SEARCH RESULTS

We recover 1201 candidates that have FAR less than 2 per day in any of the search pipelines. These events and their estimated source probabilities are shown in Fig. 2. The candidates are shown in decreasing order of $p_{\rm astro}$. The total sum of $p_{\rm astro}$ represents the Poisson rate of sources that pass the FAR threshold of 2 per day in each source class per O3a experiment, as estimated by the search pipelines. We find that this corresponds to between 24.95–44.50 signals in the BBH class, 0.66–3.80 signals in the NSBH class, and 0.22–0.81 signals in the BNS class in O3a. The range represents the difference in the search pipelines. We do not consider the PyCBC-BBH analysis in the estimate of the number of signals in the BNS class provided here, as the analysis does not search over the BNS parameter space. Names are marked for the candidate events with $p_{\rm BNS}$ or $p_{\rm NSBH}$ greater than 20%. The dashed vertical line shows the least significant event with $p_{\rm astro}$ greater than 0.5. An estimate of the rate of sources in the subthreshold candidate list per O3a experiment is obtained by the contribution to the sum from events with $p_{\rm astro}$ less than 0.5. This corresponds to between 2.55–12.40 signals in the BBH class, 0.36–2.39 signals in the NSBH class, and 0.02–0.49 signals in the BNS class in the subthreshold candidates in O3a.

We find 44 high probability CBC candidates that have $p_{\rm astro}$ greater than 0.5. These events are listed in Table II.

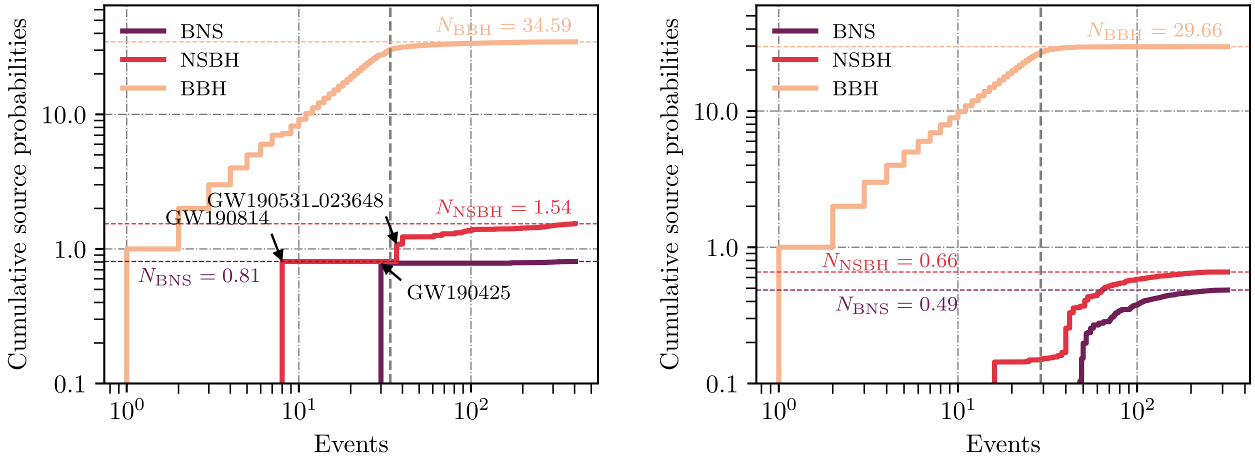

(a) GstLAL

(b) MBTA

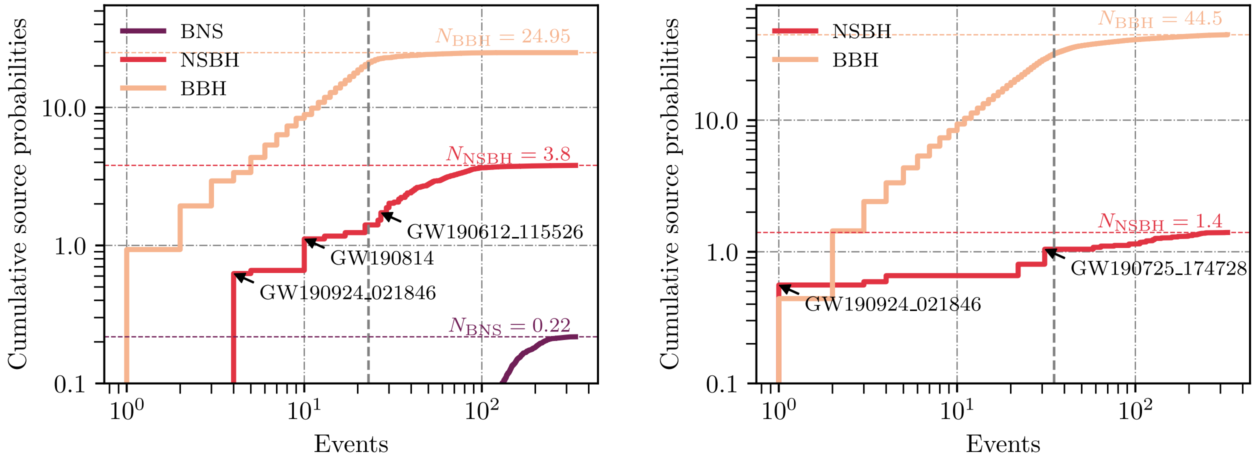

(c) PyCBC

(d) PyCBC-BBH

FIG. 2. Cumulative sum of p_{BNS}, p_{NSBH}, p_{BBH} as a function of the candidates that pass a FAR threshold of 2 per day. The events are shown in decreasing order of p_{astro}. The sum of the source probabilities shown here represents the estimated Poisson rate of sources in each source class per O3a experiment by the different search pipelines. An estimate of the rate of sources in the subthreshold candidate list is obtained by the contribution to the sum from events with p_{astro} less than 0.5. This estimate yields between 2.55–12.40 signals in the BBH class, 0.36–2.39 signals in the NSBH class, and 0.02–0.49 signals in the BNS class in the subthreshold candidates in O3a. The dashed vertical gray line shows where this threshold is for each pipeline. Names are marked for the candidate events with p_{BNS} or p_{NSBH} greater than 20%, since these are of particular interest for cross-correlation studies.

This list includes eight new candidates that were not present in GWTC-2 [8]. These are marked in bold in Table II. Out of the 44 candidates, four were found with significant SNR only in one of the detectors by the GstLAL search, which is the only pipeline that looked for GW signals in single-detector data. These are listed with a dagger (†) next to the FAR in Table II. For the majority of events listed in Table II, $p_{\mathrm{astro}} \approx p_{\mathrm{BBH}}$; the exceptions are listed in Table III, which provides the list of candidates that have p_{BNS} or p_{NSBH} greater than 0.01.

A. New high probability candidates

We recover all the events found in GWTC-2 as having p_{astro} above 0.5, with the exception of three: GW190424_180648, GW190426_152155, and GW190909_114149. Since the rate of BBH events detectable by the LIGO–Virgo detectors is greater than the rate of detectable BNS or NSBH events, the p_{astro} for events in the BBH class is higher than that of the events in the BNS or NSBH class at a fixed FAR. Therefore, in switching to a p_{astro} threshold from a FAR threshold, one can expect to add BBH events while dropping some low-mass events.

All the eight new candidates with p_{astro} greater than 0.5 are classified as BBHs, that is, p_{BBH} is greater than p_{NSBH} and p_{BNS}. Only one new candidate, GW190725_174728, has a non-negligible probability in a source class other than BBH, with nonzero p_{NSBH} (Table III). Out of the eight candidates, only two (GW190725_174728 and GW190916_200658) are assigned $p_{\mathrm{astro}} > 0.5$ by more than one pipeline. Differences between pipelines are expected, due to the effects of random noise fluctuations

TABLE IV. Marginal-significance GW event candidate list. There are two candidates that are found in at least one of the searches with a FAR less than 2 per year, but with a $p_{\rm astro}$ smaller than 0.5 in all searches. The candidate in bold, GW190531_023648, is a new candidate identified in GWTC-2.1, not included in GWTC-2. The column max $p_{\rm astro}$ shows the astrophysical class assigned with highest probability. Both candidates are detected by GstLAL with a small FAR, and are assigned to the NSBH class with $p_{\rm astro}$ and $p_{\rm NSBH}$ smaller than 0.5.

		MBTA			GstLAL			PyCBC		
Name	Inst.	FAR (yr^{-1})	SNR	Max $p_{\rm astro}$	FAR (yr^{-1})	SNR	Max $p_{\rm astro}$	FAR (yr^{-1})	SNR	Max $p_{\rm astro}$
GW190426_152155	HLV	32	9.8	$p_{\rm NSBH} = 0.01$	0.91	10.1	$p_{\rm NSBH} = 0.14$	43	8.8	$p_{\rm NSBH} = 0.01$
GW190531_023648	HLV	8.1	9.8	$p_{\rm BNS} = 0.05$	0.41	10.0	$p_{\rm NSBH} = 0.28$	29	9.2	$p_{\rm NSBH} = 0.01$

on the different ranking statistics used, and due to different assumed signal distributions and other choices. In principle, a more accurate assessment of the candidates' origins could be obtained by considering information from all pipelines; however, this is not currently implemented as a quantitative measure. One of the events, GW190917_114630, is identified as a BBH by the GstLAL pipeline, with $p_{\rm BBH} = 0.77$ (Table II). However, when its source properties are inferred by followup pipelines, the mass parameters are found to be consistent with NSBH systems. Had it been classified as an NSBH to begin with by the search pipeline, the resulting $p_{\rm astro}$ would not have made the threshold of 0.5. There is also nonstationary noise in the LIGO Livingston detector at the time of this event, but we have no evidence that the FAR of the event is misestimated. Out of the eight new candidates, five candidates (GW190426_190642, GW190725_174728, GW190805_211137, GW190916_200658, and GW190925_232845) were identified in the LVC search for gravitationally lensed candidates in O3a data [29], while four candidates (GW190725_174728, GW190916_200658, GW190925_232845, and GW190926_050336) were also independently identified and presented in 3-OGC [17]. The source properties of all eight candidates are discussed in Sec. V D.

B. GWTC-2 candidates with $p_{\rm astro} < 0.5$

The three events in GWTC-2 that have a $p_{\rm astro}$ smaller than 0.5 in GWTC-2.1 analyses are as follows:

1. **GW190424_180648**: This event was found by GstLAL as a single detector BBH event in Livingston. However, the data surrounding this event recorded periodic glitching from a camera shutter and iDQ (Sec. III B 1) heavily downranked the time span surrounding this event [113]. Figure 4 of the paper describing this iDQ [113] shows both the inspiral track and the surrounding glitches in the time-frequency spectrogram surrounding this event and the response of iDQ. While the down-ranking due to iDQ for this particular event remains largely the same between GWTC-2 and GWTC-2.1, the retuning of the singles penalty (Sec. III B 1) in GstLAL for GWTC-2.1 caused the significance of the event to go down. Consequently, in GWTC-2.1, this event does not meet either the FAR threshold of 2 per year or the $p_{\rm astro}$ threshold of 0.5.
2. **GW190426_152155**: This event is in the marginal-significance candidate list for GWTC-2.1 (Table IV); the FAR is similar to the one in GWTC-2 and still passed the threshold of 2 per year considered in the previous catalog. However, based on the masses recovered by the pipeline, it is assigned to the NSBH class with $p_{\rm NSBH} = 0.14$. The low $p_{\rm astro}$ in the NSBH class is due to the fact that the inferred rate of detectable NSBHs is lower than that of detectable BBHs.
3. **GW190909_114149**: This candidate BBH event was found as a coincident event in Hanford and Livingston detectors by GstLAL. It is recovered now with smaller SNR in the Hanford detector and is therefore ranked lower.

C. Marginal-significance candidates

The two GW candidates that satisfy the FAR criteria used by GWTC-2, but do not have $p_{\rm astro}$ greater than 0.5 are listed as marginal candidates in Table IV. Both these events were detected by GstLAL with a small FAR, and were assigned to the NSBH class with $p_{\rm astro}$ and $p_{\rm NSBH}$ smaller than 0.5. Since the rate of detectable signals in the NSBH class is smaller than that in the BBH class, the $p_{\rm astro}$ for these are smaller than they would be in the BBH class at the same FAR.

D. Search sensitivity

As in GWTC-2 [8], we quantify the sensitivity of the search via a campaign of simulated signals injected into the O3a data and analyzed by the search pipelines. We use a BBH signal distribution adjusted over that used for GWTC-2 to give more even coverage of the inferred distribution from O1–O3a [122], changing specifically the distributions over binary mass ratio and redshift. In addition to the BBH set, we also inject BNS and NSBH sets of simulated signals into the data. The sets are generated in two stages: first, points are sampled out to the maximum redshift considered for each set, then the samples are reduced to sets of potentially detectable signals by imposing that the expected LIGO Hanford–LIGO Livingston network SNR, calculated using a representative noise

TABLE V. Measures of sensitivity for the search pipelines. We state the sensitive hypervolume $\mathcal{V}$ for each of four assumed signal populations: a BBH population following the injected distribution, a BBH population given by the POWER LAW + PEAK model of [122], and BNS and NSBH populations following the injected distributions. We give estimates for each search pipeline independently at a FAR threshold of 2 per year, and for all pipelines combined, i.e. counting all injections detected in at least one pipeline at the given threshold.

	Injection populations					Sensitive hypervolume $\mathcal{V}$ (Gpc^3 yr)				
	Mass distribution	Mass range ($M_\odot$)	Spin range	Redshift evolution	Max. redshift	GstLAL	MBTA	PyCBC	PyCBC BBH	All
BBH (INJ)	$p(m_1) \propto {m_1}^{-2.35}$ $p(m_2 \vert m_1) \propto m_2$	$2 < m_1 < 100$ $2 < m_2 < 100$	$\vert\chi_{1,2}\vert < 0.998$	$\kappa = 1$	1.9	0.258	0.196	0.194	0.234	0.308
BBH (POP)	POWER LAW + PEAK	(see text)	$\vert\chi_{1,2}\vert < 0.998$	$\kappa = 0$	1.9	1.22	0.885	0.914	1.20	1.44
BNS	uniform	$1 < m_1 < 2.5$ $1 < m_2 < 2.5$	$\vert\chi_{1,2}\vert < 0.4$	$\kappa = 0$	0.15	0.00594	0.00631	0.00657	⋯	0.00781
NSBH	$p(m_1) \propto {m_1}^{-2.35}$ uniform	$2.5 < m_1 < 60$ $1 < m_2 < 2.5$	$\vert\chi_1\vert < 0.998$ $\vert\chi_2\vert < 0.4$	$\kappa = 0$	0.25	0.0174	0.0165	0.0181	⋯	0.0221

power spectral density (PSD), be above a threshold of 6. Although this threshold is below the matched-filter SNRs of events we consider as high-significance candidates, for detection thresholds corresponding to FARs significantly higher than 2 per year (the value used in GWTC-2), the cut may remove a non-negligible fraction of potentially detectable signals, due to random fluctuations in matched-filter SNR. The results of this simulation campaign for all the search pipelines have been made available [131].

The BNS signals are generated using the SpinTaylorT4 waveform model [117,119], while the BBH and NSBH sets are generated using the SEOBNRv4PHM model [61–63]. For simulated signals with redshifted total mass below $9M_\odot$, the SEOBNRv4P model without higher-order multipole emission was used, as higher-order multipoles would lie above the data sampling Nyquist frequency. The component spin magnitudes $|\chi_i|$ are distributed uniformly up to a maximum of 0.4 for NS components and 0.998 for BBH, with isotropically distributed orientations.

The signal distributions over sky direction and binary orientation are isotropic. The distributions over redshift are proportional to the comoving volume element $\mathrm{d}V_\mathrm{c}/\mathrm{d}z$, multiplied by a factor $(1+z)^{-1}$ accounting for time dilation, and by a factor $(1+z)^\kappa$ modeling possible evolution of the comoving merger rate density with redshift (as in Appendix E of the GWTC-2 population analysis [122]). A summary of the distributions of the three injection sets is given in Table V.

Given the merger distribution used for each injection set, the sensitivity of each search over the O3 data is quantified by relating the expected number of detections, at a specified significance threshold, to the local astrophysical merger rate as $N_\mathrm{det} = \mathcal{V}R(z=0)$, where $\mathcal{V}$ is an effective sensitive hypervolume with units of volume × time. This effective hypervolume is estimated by counting the number of injected signals that are detected at the given threshold, here a FAR of 2 per year.

In addition to assumed merger distributions that follow those used for the injection sets, we also provide $\mathcal{V}$ for a fiducial BBH population model representative of those found to have high-posterior probability in our population analysis of GWTC-2 [122]. We choose the POWER LAW + PEAK model (defined in Appendix B.2 of the GWTC-2 population analysis [122]) with parameters $\alpha = 2.5, \beta = 1.5$, $m_\mathrm{min} = 5M_\odot$, $m_\mathrm{max} = 80M_\odot$, $\lambda_\mathrm{peak} = 0.1$, $\mu_m = 34M_\odot$, $\sigma_m = 5M_\odot$, $\delta_m = 3.5M_\odot$, setting the redshift evolution to $\kappa = 0$. The sensitivity for this BBH population is evaluated via importance sampling [115,132] implemented via GWPOPULATION [133]. The effective hypervolume for each search and signal population is given in Table V.

E. Rates of BBH and BNS events

The rates of BBH and BNS binary mergers in the local Universe were estimated in a companion paper [122] to GWTC-2, using the count of detected events with FAR below 1 per year, combined with estimates of search sensitivity to the respective populations. The BBH rate estimate was marginalized over uncertainties in the parameters of the population models used, while the BNS rate estimate assumed a population uniform in component masses between $1M_\odot$ and $2.5M_\odot$. The merger rate of NSBHs was calculated following the discovery of GW200105_162426 and GW200115_042309 [134], and we do not update it here.

Here, we present complementary BBH and BNS rate estimates based solely on the matched filter search pipeline outputs, with methods that allow us to incorporate a large number of likely noise (background) events [26] and thus avoid potential bias due to an arbitrary choice of significance threshold. Such methods allow for both foreground (signal) and background event distributions with *a priori* unknown rates, considered as independent Poisson processes. Furthermore, for the GstLAL pipeline we employ a multicomponent mixture analysis [114] to estimate the rates of events in several astrophysical classes (BNS, NSBH, and BBH) and terrestrial. Every trigger is assigned probabilities of membership in each class, as described in Sec. III B 1. For the MBTA and PyCBC rate estimates, only the BBH class is considered.

The merger rate estimate then arises from the number of search events assigned to each class, divided by the estimated search sensitivity obtained via injection campaigns reweighted to an astrophysical population model [115], as discussed in the previous section. The population models used here to quantify search sensitivity are in general different from those used to obtain source classification probabilities, described in Sec. III A.

In both the BBH and BNS cases, as for other rate interval estimates derived from search results [7], a Poisson-Jeffreys ($\propto R^{-1/2}$) prior was used. The choice of prior has little influence on estimated BBH rate due to the large count of signals, but it has a nontrivial effect on the BNS rate estimate as compared to, for instance, a uniform prior.

BBH merger rate estimates are provided by the GstLAL, PyCBC-BBH, and MBTA pipelines. The astrophysical population assumed for measuring search sensitivities is given by the POWER LAW + PEAK model [122] with fiducial parameters as in Sec. IV D. The resulting merger rates are $25.0^{+7.2}_{-6.1}\ \mathrm{Gpc^{-3}\,yr^{-1}}$ for GstLAL, $26.0^{+8.2}_{-6.8}\ \mathrm{Gpc^{-3}\,yr^{-1}}$ for PyCBC -BBH, and $25.6^{+9.6}_{-7.8}\ \mathrm{Gpc^{-3}\,yr^{-1}}$ for MBTA. These estimates are fully consistent with the estimate of $23.9^{+14.3}_{-8.6}\ \mathrm{Gpc^{-3}\,yr^{-1}}$ as derived from GWTC-2 [122] using only significant ($\mathrm{FAR} < 1\ \mathrm{yr^{-1}}$) events, and allowing for uncertainties in the population model parameters. Following the GWTC-2 analysis [122], we have not included the effect of calibration uncertainties in our rate estimates. A full quantitative analysis of such uncertainties would require accounting for possible frequency- and time-dependent amplitude systematic errors [77]; these are typically $\sim 3\%$ or less, corresponding to a $\lesssim 10\%$ sensitive volume uncertainty which remains subdominant to the Poisson uncertainty in the signal counts [122].

Since the only significant event consistent with BNS merger in O3a, GW190425 [135], was observed in a single detector, it is present only in the GstLAL search results. Hence, we quote a BNS merger rate estimate only from the GstLAL pipeline, as we expect this to be more informative than estimates from pipelines that did not consider single-detector triggers. For measuring the search sensitivity to BNS mergers, we use the injected population described above in Sec. IV D, yielding an estimated merger rate $286^{+510}_{-237}\ \mathrm{Gpc^{-3}\,yr^{-1}}$. This estimate is fully consistent within uncertainties with the simpler estimate of $320^{+490}_{-240}\ \mathrm{Gpc^{-3}\,yr^{-1}}$ derived using a fixed threshold in expected SNR to determine sensitivity to simulated signals [122].

V. ESTIMATION OF SOURCE PARAMETERS

The physical parameters $\vec{\vartheta}$ describing each GW source binary, corresponding to individual entries from the list of events in Table II, are inferred directly from the data d and represented as a posterior probability distribution $p(\vec{\vartheta}|d)$. This probability distribution is evaluated through Bayes' theorem as

$$p(\vec{\vartheta}|d) \propto p(d|\vec{\vartheta})\pi(\vec{\vartheta}), \tag{3}$$

with $p(d|\vec{\vartheta})$ being the likelihood of d given a set of source parameters $\vec{\vartheta}$, and $\pi(\vec{\vartheta})$ being the prior probability distribution assumed for those parameters.

The likelihood itself describes the assumptions of the underlying stochastic process generating the noise present in d from a given detector. This noise is assumed to be Gaussian, stationary and uncorrelated between pairs of detectors [136,137], as further discussed in Sec. II B. This yields a Gaussian likelihood [138,139], which for the ith detector used in a given analysis takes the form

$$p(d^i|\vec{\vartheta}) \propto \exp\left[-\frac{1}{2}\langle d^i - h^i_{\mathrm{M}}(\vec{\vartheta})|d^i - h^i_{\mathrm{M}}(\vec{\vartheta})\rangle\right], \tag{4}$$

with d^i representing the data from this instrument. $h^i_{\mathrm{M}}(\vec{\vartheta})$ is the binary waveform model $h(\vec{\vartheta})$ calculated for $\vec{\vartheta}$ after being projected onto the detector and adjusted to account for the uncertainty present in the offline calibration (as described in Sec. II) of d^i [140]. The final likelihood is evaluated coherently across the network of available detectors and is obtained by multiplication of the likelihoods in each detector.

The term from Eq. (4) in angle brackets, $\langle a|b\rangle$, represents a noise-weighted inner product [138,141]. In addition to d^i and $h^i_M(\vec{\vartheta})$, evaluating this inner product requires specification of the bandwidth to be used in the analysis as well as the PSD characterizing the noise process. The low-frequency cutoff used in our analysis is set at $f_{\mathrm{low}} = 20$ Hz. Time-domain waveform models are generated starting at a frequency f_{start} such that the $(\ell, |m|) = (3, 3)$ spherical harmonic mode of the binary inspiral signal, as estimated from a set of preliminary analyses [7,8], is present at f_{low}. The high-frequency cutoff f_{high} is selected for each analysis as $f_{\mathrm{high}} = \alpha^{\mathrm{roll-off}} f_{\mathrm{Nyquist}}$ such that the ringdown frequency of the $(\ell, |m|) = (3, 3)$ spherical harmonic mode, inferred from waveforms taken from the same set of preliminary analyses as mentioned above [7,8], occurs below f_{high}. The parameter $\alpha^{\mathrm{roll-off}}$ in this expression is a scale factor chosen in order to minimize the frequency roll-off effects caused by the application of a tapering window to the time-domain data [142]. The Nyquist frequency f_{Nyquist} is then selected as the smallest power-of-two-valued frequency which together with $\alpha^{\mathrm{roll-off}} = 0.875$ satisfies the constraint on

f_{high} specified above. Similarly, the duration of data d used in each analysis is determined from a requirement that the waveforms from previous analyses [7,8] as evaluated from $f_{\mathrm{low}} = 20$ Hz and rounding up to the next power-of-two number of seconds, are contained in the selected data segment. The PSD for each event is inferred directly from the same data that is to be used in the likelihood, through the parametrized model implemented in BayesWave [143,144]. From the inferred posterior distribution of PSDs, the median value at each frequency is then used in the final analysis [144,145].

A GW signal emitted from a binary containing two BHs can be fully characterized by $\vec{\vartheta}$ containing a set of fifteen parameters, as introduced in Sec. III A, if the binary orbit is assumed to have negligible eccentricity.[1] The mass and spin of the postmerger remnant BH, together with the peak GW luminosity, are calculated from the initial binary parameters using fits to numerical relativity (NR) [146–151].

For binaries expected to contain at least one NS, the time-evolution of the binary orbit is modified by the presence of matter and quantified in terms of the dimensionless quadrupole tidal deformability $\Lambda_{1,2}$, adding one more parameter for each NS. In addition to the quadrupole tidal effects, other matter effects are parametrized in terms of $\Lambda_{1,2}$ using equation of state (EOS)-insensitive relations [152]. When a GW event is assumed to contain one or more neutron star, we do not report final masses or spins for the remnant object.

A. Waveform models

The binary properties of the observed GW events are characterized through matching against a set of waveform models. For the events identified as BBHs, with both components inferred to have masses above $3M_{\odot}$, we use the independently developed IMRPhenomXPHM [57–60] and SEOBNRv4PHM [61–63] models. Both waveform models capture effects from spin-induced precession of the binary orbit, as well as contributions from both the dominant and subdominant multipole moments of the emitted gravitational radiation.

IMRPhenomXPHM [57] describes the GW signal from precessing noneccentric BBHs and is part of the fourth generation of phenomenological frequency domain models. Precession is implemented via a twisting-up procedure, as for its predecessors IMRPhenomPv2 [153,154] and IMRPhenomPv3HM [155,156]. For this, an aligned-spin model defined in the coprecessing frame is mapped through a suitable frame rotation to approximate the multipolar emission of a precessing system in the inertial frame. The stationary phase approximation is used to obtain closed form expressions in the frequency domain [157]. The description for the precession dynamics is derived using a multiple scale analysis of the post-Newtonian (PN) equations of motion [158]. The underlying aligned spin model for IMRPhenomXPHM is IMRPhenomXHM [58–60], which calibrates the $(\ell, |m|) = (2,2), (2,1), (3,2), (3,3)$ and $(4,4)$ spherical harmonic modes to hybrid waveforms constructed from NR waveforms and information from the PN and effective-one-body (EOB) descriptions for the inspiral. IMRPhenomXHM represents the amplitudes and phases of spherical or spheroidal harmonic modes in terms of piecewise closed form expressions, with coefficients that vary across the compact binary parameter space, which results in extreme compression of the waveform information and computational efficiency.

SEOBNRv4PHM comes from another waveform family that is primarily based on the EOB formalism where the relativistic two-body problem is mapped to motion of a single body in an effective metric. In this framework, analytical information from several sources, such as PN theory and the test-particle limit, is combined in a resummed form. This is complemented with insights from NR simulations that accurately model the strong-field regime and incorporated into the EOB waveforms via a calibration procedure. We use the SEOBNRv4PHM [61–63] model, which includes precession and modes beyond the dominant quadrupole. This model is based on the aligned-spin model SEOBNRv4HM [64] and is calibrated to NR in that regime. It features full two-spin treatment of the precession equations and relies on a twisting-up procedure to map aligned spin waveforms in the coprecessing frame to the precessing waveforms in the inertial frame [62,63].

For GW190917_114630, the less massive component is indicated to lie below $3M_{\odot}$ and hence to have a strong likelihood of being a NS instead of a BH. Following the discussion for GW190814 [41], the nature of the less massive compact object in GW190917_114630 cannot be discerned from the GW data at present. This is primarily dependent on the unequal masses [159–161] which will lead the merger of the binary to occur before an eventual NS component could have been tidally disrupted for any realistic NS EOS [159]. The lack of an observable NS disruption thus removes the potential for the observed signal to contain any additional information above a point-particle baseline. For this reason, we present results for GW190917_114630 and GW190814 based on the BBH waveform models discussed above.

For GW190425, the only O3a event in this catalog classified as a BNS, we follow previous analyses [8,135], and report findings using the IMRPhenomP_NRTidal waveform model [65,66], which is based upon the BBH model IMRPhenomPv2 [153,162,163] with the addition of EOS dependent self-spin effects and contributions from tidal interactions tuned against NR and tidal EOB models. In order to reduce computational cost for the analysis of GW190425, a reduced-order quadrature method was applied to the IMRPhenomP_NRTidal model used [164,165].

---

[1] See Table E1 in [142] for precise definitions of all parameters used.

B. Sampling methods

To represent the continuous posterior probability density functions in $\vec{\vartheta}$, we draw discrete samples from those distributions using three different methods. For analyses using IMRPhenomXPHM and IMRPhenomP_NRTidal we use the Bilby inference package [142,166], together with the nested sampling [167] method implemented in the Dynesty sampler [168], or the Markov-chain Monte Carlo sampler implemented in the LALInference package [139,169–171]. An extensive set of comparison and verification studies for analyses done with both Bilby and LALInference shows consistency between the two inference variants [142]. For analyses using SEOBNRv4PHM, we use the RIFT package [172–175] which, due to a hybrid exploration of the parameter space split into intrinsic (masses and spins) and extrinsic parameters, is better suited for use with this more computationally expensive waveform model. The robustness and performance of RIFT is verified through a set of tests [175]. The Asimov library [176] is used to manage all stages of the parameter-estimation analyses. This includes the automated creation of common configurations used for the Bilby, LALInference and RIFT runs, and the actual initialization, maintenance and completion of the analyses. The results from all analyses are collected, again managed by Asimov, and presented in a common format using the PESummary package [177,178].

C. Priors

The prior probability on $\vec{\vartheta}$ is defined similar to GWTC-2 [8] as uniform in spin magnitudes and redshifted component masses (specified in the geocenter rest frame), and isotropic in spin orientations, sky location and orientation of the binary orbit. We also assume uncorrelated and uniform prior probabilities for the tidal deformability parameters of the NSs in GW190425. The prior on the luminosity distance follows a distribution uniform in comoving volume, using a flat ΛCDM cosmology with Hubble constant $H_0 = 67.90\ \mathrm{km\,s^{-1}\,Mpc^{-1}}$ and matter density $\Omega_\mathrm{m} = 0.3065$ [179]. Masses reported in Sec. V D are defined in the rest frame of the original binary, and computed by dividing the redshifted masses by $(1+z)$, with z calculated from the same cosmological model. For GW190425 we perform two separate analyses, differing in the spin magnitudes they allow with a low spin ($|\vec{\chi}_1| < 0.05$) and a high spin ($|\vec{\chi}_1| < 0.89$), consistent with the choices made in GWTC-2 [8] for this binary.

All analyses account for uncertainties in the reported strain calibration [77,180]. The calibration uncertainties are described as frequency-dependent splines, defined separately for the strain amplitude and phase [181]. The coefficients at the spline nodes are allowed to vary alongside the binary signal parameters according to a Gaussian prior distribution set by the measured uncertainty at each node [140]. For analyses performed with the LALInference or Bilby inference packages, calibration uncertainties are marginalized over through direct sampling of the spline coefficients whereas RIFT analyses implement a likelihood reweighting method through importance sampling over an initial analysis where perfect calibration is assumed [182].

D. Source properties

In this subsection we report the inferred source properties of the eight new events reported in Table II. The source properties for the BBH events from the first and second observation runs, reported in GWTC-1 [7], together with the remaining 36 events from Table II are reported in

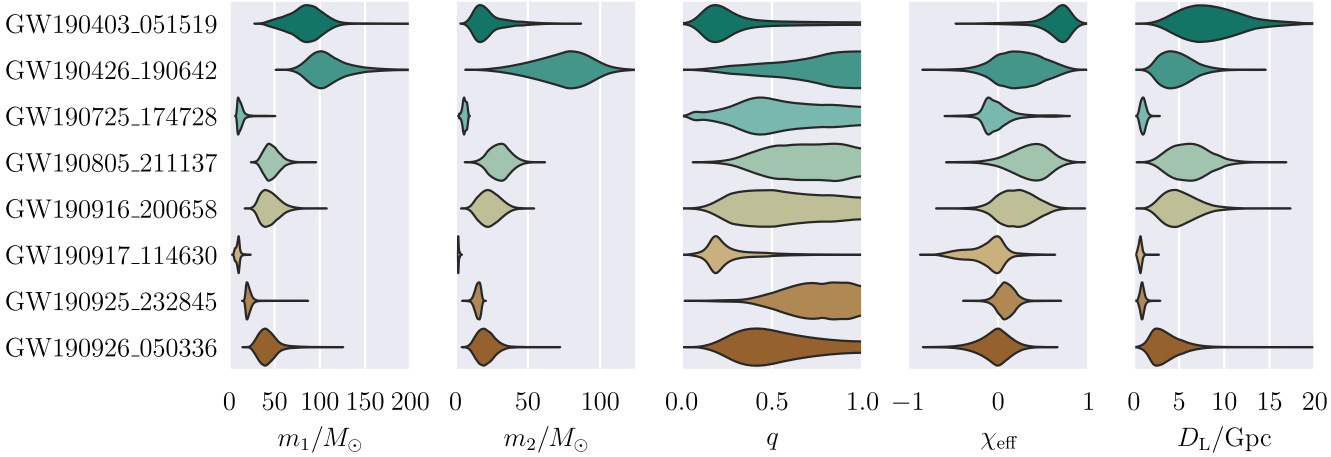

FIG. 3. Marginal posterior distributions on the primary mass m_1, secondary mass m_2, mass ratio q, effective inspiral spin χ_eff and luminosity distance D_L for the eight events that are new to this catalog with $p_\mathrm{astro} > 0.5$, highlighted in bold in Table II. The vertical span for each region is constructed to be proportional to the one-dimensional marginal posterior at a given parameter value for the corresponding event. The posterior distributions are also represented numerically in terms of their one-dimensional median and 90% credible intervals in Table VI.

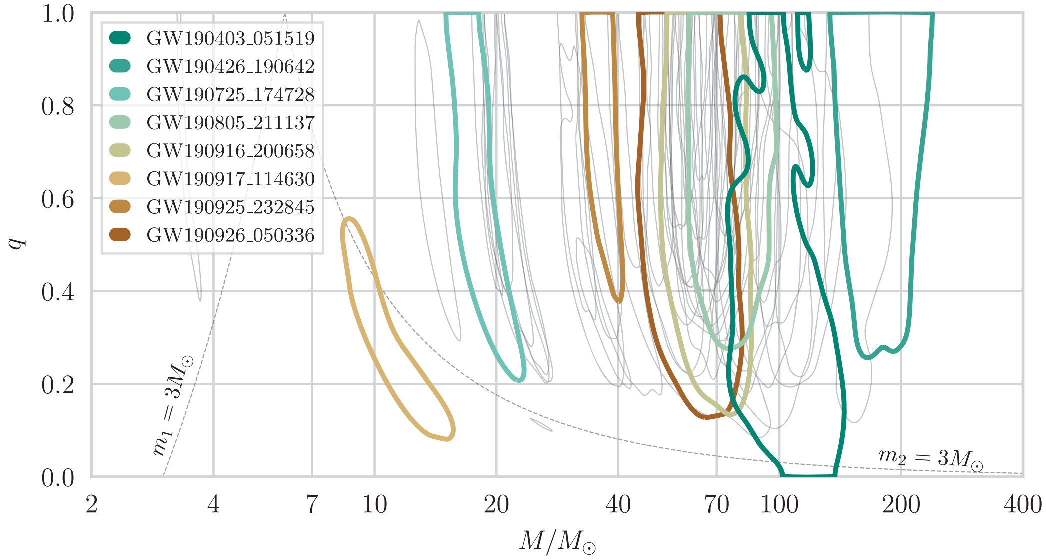

FIG. 4. Contours representing the 90% credible regions in the total mass M and mass ratio q plane for all events reported in this catalog. The events that are new to this catalog with $p_{\rm astro} > 0.5$, highlighted in bold in Table II, are highlighted in this figure following the same color scheme used in Fig. 3. The dashed lines act to separate regions where the primary and secondary binary component can have a mass below $3M_\odot$.

the Appendix. For the vast majority of the events reported both in this section and in the Appendix, the quoted source properties are taken from a set of posterior samples constructed from the two IMRPhenomXPHM and SEOBNRv4PHM analyses with each given equal weight. For a subset of events (GW151226, GW190413_052954, GW190413_134308, GW190421_213856, GW190426_190642, GW190521, GW190602_175927, GW190719_215514, GW190725_174728, GW190803_022701, GW190814, GW190828_063405, GW190828_065509, GW190917_114630, GW190926_050336, and GW190929_012149) the respective SEOBNRv4PHM analyses did not converge in a timely manner, hence we report results from the IMRPhenomXPHM only for these events.

A selection of the one-dimensional marginal posterior distributions are shown in Fig. 3, with two-dimensional projections on the M–q and $\mathcal{M}$–$\chi_{\rm eff}$ planes in Figs. 4 and 5

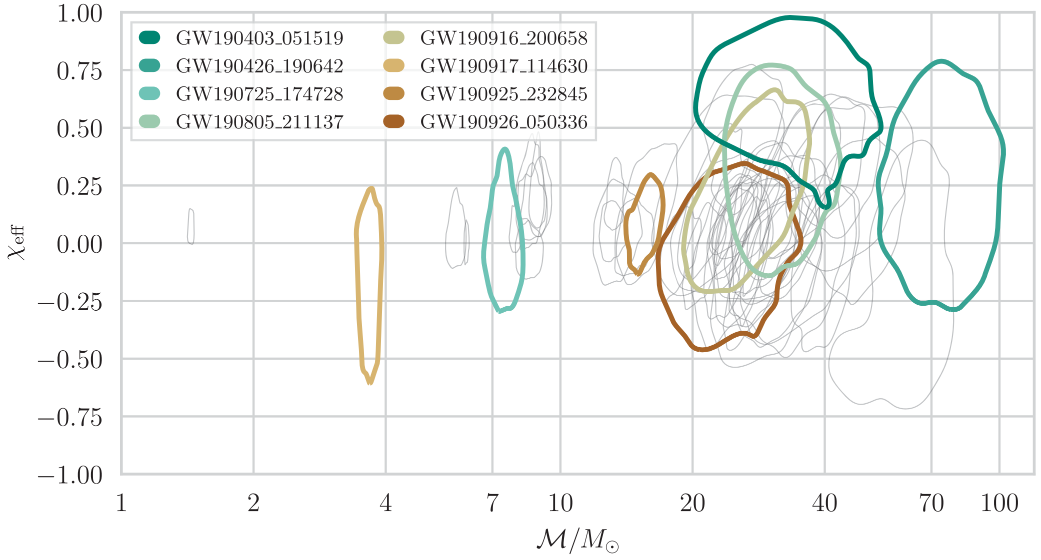

FIG. 5. Contours representing the 90% credible regions in the plane of chirp mass $\mathcal{M}$ and effective inspiral spin $\chi_{\rm eff}$ for all events reported in this catalog. The events that are new to this catalog with $p_{\rm astro} > 0.5$, highlighted in bold in Table II, are highlighted in this figure following the same color scheme used in Fig. 3.

TABLE VI. Median and 90% symmetric credible intervals for the one-dimensional marginal posterior distributions on selected source parameters for the eight events that are new to this catalog with $p_{\mathrm{astro}} > 0.5$, highlighted in bold in Table II. The columns show source total mass M, chirp mass $\mathcal{M}$ and component masses m_i, dimensionless effective inspiral spin χ_{eff}, luminosity distance D_L, redshift z, final mass M_f, final spin χ_{f}, sky localization $\Delta\Omega$ and the network matched-filter SNR. The sky localization is the area of the 90% credible region. All quoted results are calculated from a set of posterior samples drawn with equal weight from the IMRPhenomXPHM and SEOBNRv4PHM analyses, with the exception of the SNRs that are taken from the IMRPhenomXPHM analysis alone (as RIFT, which was used for the SEOBNRv4PHM analysis, does not output that quantity). Additionally, following Sec. V D, the results presented for GW190426_190642, GW190725_174728, GW190917_114630, and GW190926_050336 are taken from an analysis using the IMRPhenomXPHM model only. A subset of the one-dimensional posterior distributions are visualized in Fig. 3. Two-dimensional projections of the 90% credible regions in the M–q and $\mathcal{M}$–χ_{eff} planes are shown in Figs. 4 and 5.

Event	M ($M_\odot$)	$\mathcal{M}$ ($M_\odot$)	m_1 ($M_\odot$)	m_2 ($M_\odot$)	χ_{eff}	D_{L} (Gpc)	z	M_{f} ($M_\odot$)	χ_{f}	$\Delta\Omega$ (deg^2)	SNR
GW190403_051519	$106.6^{+26.7}_{-23.6}$	$34.0^{+15.1}_{-8.4}$	$85.0^{+27.8}_{-33.0}$	$20.0^{+26.3}_{-8.4}$	$0.68^{+0.16}_{-0.43}$	$8.28^{+6.72}_{-4.29}$	$1.18^{+0.73}_{-0.53}$	$102.2^{+26.3}_{-24.3}$	$0.91^{+0.05}_{-0.17}$	3900	$7.6^{+0.6}_{-1.1}$
GW190426_190642	$182.3^{+40.2}_{-35.7}$	$76.0^{+19.1}_{-17.4}$	$105.5^{+45.3}_{-24.1}$	$76.0^{+26.2}_{-36.5}$	$0.23^{+0.42}_{-0.41}$	$4.58^{+3.40}_{-2.28}$	$0.73^{+0.41}_{-0.32}$	$172.9^{+37.7}_{-33.6}$	$0.77^{+0.14}_{-0.16}$	4600	$8.7^{+0.4}_{-0.6}$
GW190725_174728	$18.3^{+7.4}_{-1.9}$	$7.4^{+0.5}_{-0.5}$	$11.8^{+10.1}_{-3.0}$	$6.3^{+2.1}_{-2.5}$	$-0.04^{+0.36}_{-0.16}$	$1.03^{+0.52}_{-0.43}$	$0.20^{+0.09}_{-0.08}$	$17.6^{+7.7}_{-1.8}$	$0.65^{+0.09}_{-0.07}$	2200	$9.1^{+0.4}_{-0.7}$
GW190805_211137	$76.7^{+19.5}_{-13.8}$	$31.9^{+8.8}_{-6.3}$	$46.2^{+15.4}_{-11.2}$	$30.6^{+11.8}_{-11.3}$	$0.37^{+0.29}_{-0.39}$	$6.13^{+3.72}_{-3.08}$	$0.92^{+0.43}_{-0.40}$	$72.4^{+18.2}_{-13.2}$	$0.82^{+0.09}_{-0.16}$	1600	$8.1^{+0.5}_{-0.7}$
GW190916_200658	$68.0^{+18.3}_{-13.1}$	$26.9^{+8.2}_{-5.4}$	$43.8^{+19.9}_{-12.6}$	$23.3^{+12.5}_{-10.0}$	$0.20^{+0.33}_{-0.31}$	$4.94^{+3.71}_{-2.38}$	$0.77^{+0.45}_{-0.32}$	$65.0^{+17.3}_{-12.6}$	$0.74^{+0.13}_{-0.24}$	2400	$8.1^{+0.3}_{-0.5}$
GW190917_114630	$11.8^{+3.0}_{-2.8}$	$3.7^{+0.2}_{-0.2}$	$9.7^{+3.4}_{-3.9}$	$2.1^{+1.1}_{-0.4}$	$-0.08^{+0.21}_{-0.43}$	$0.72^{+0.30}_{-0.31}$	$0.15^{+0.05}_{-0.06}$	$11.6^{+3.1}_{-2.9}$	$0.42^{+0.14}_{-0.05}$	1700	$8.3^{+0.5}_{-0.8}$
GW190925_232845	$36.7^{+3.6}_{-2.8}$	$15.6^{+1.1}_{-1.1}$	$20.8^{+6.5}_{-2.9}$	$15.5^{+2.5}_{-3.6}$	$0.09^{+0.16}_{-0.15}$	$0.93^{+0.46}_{-0.35}$	$0.19^{+0.08}_{-0.07}$	$34.9^{+3.5}_{-2.6}$	$0.71^{+0.06}_{-0.06}$	2900	$9.7^{+0.3}_{-0.6}$
GW190926_050336	$61.9^{+22.7}_{-12.0}$	$24.4^{+9.0}_{-4.9}$	$41.1^{+20.8}_{-12.5}$	$20.4^{+11.4}_{-8.2}$	$-0.02^{+0.25}_{-0.32}$	$3.28^{+3.40}_{-1.73}$	$0.55^{+0.44}_{-0.26}$	$59.6^{+22.1}_{-11.8}$	$0.64^{+0.14}_{-0.20}$	2000	$8.1^{+0.6}_{-0.8}$

respectively. A more detailed set of results are presented in Table VI in the form of median and 90% credible intervals for the one-dimensional marginal posterior distributions for all eight events. The complete multidimensional posterior distributions are available as part of the public data release accompanying this paper [183], as detailed further in Sec. VII.

1. Masses

The masses inferred for the eight events presented in this section are generally comparable to, or higher, than the binaries reported in GWTC-2 [7,8], as shown in Fig. 4. We find that the most massive BBH in GWTC-2.1 is GW190426_190642 with a total mass of $182.3^{+40.2}_{-35.7} M_\odot$ and a remnant mass of $172.9^{+37.7}_{-33.6} M_\odot$; it probably supersedes the previous most massive BBH GW190521[2] with total mass of $153.1^{+42.2}_{-16.2} M_\odot$ and a remnant mass of $147.4^{+40.0}_{-16.0} M_\odot$ as reported in Appendix A 2. Both GW190426_190642 and GW190403_051519 join GW190519_153544, GW190521, GW190602_175927, and GW190706_222641 in a population of BBHs with over 50% posterior support for total mass $M > 100 M_\odot$ [8].

While the majority of the new events show a preference for mass ratios near unity, following the trend already observed in GWTC-2 [7,8], both GW190403_051519 and GW190917_114630 recover posteriors with median $q \sim 1/5$ with $q = 0.23^{+0.57}_{-0.12}$ and $q = 0.21^{+0.32}_{-0.09}$ respectively. As shown in Fig. 4, this constraint for unequal masses is robust at the 90% credible level for both GW190403_051519 and GW190917_114630. Although the contour indicating the 90% credible region for GW190403_051519 includes support at $q \sim 0$ in Fig. 4, this is an artifact of the bounded kernel density estimation used to construct the contours, and for this event there are no samples at the prior boundary of $q = 0.05$.

2. Spins

The best measured spin parameter for CBCs with observable inspiral signals tends to be the effective inspiral spin χ_{eff} [184–186], introduced in Eq. (2), which is approximately conserved under spin-induced precession of the binary orbit [187–190]. Consequently, the angles between the spin-vectors and the orbital angular momentum at a formally infinite separation are well defined [190]. We therefore report χ_{eff}, as well as the spin-tilt angles themselves, at this fiducial reference point of infinite binary separation, or equivalently at an infinite time before the binary merger. The spins are evolved to infinite separation [191] using a precession-averaged evolution scheme [158,190] where the orbital angular momentum is computed using higher-order PN expressions.

The posterior distributions for χ_{eff} for all eight events are shown in Figs. 3 and 5. Again, the majority of the binaries are consistent with containing two nonspinning BHs with only GW190403_051519 and GW190805_211137 recovering a nonzero χ_{eff} at 90% credibility. Both binaries report predominantly positive χ_{eff}, further strengthening the pattern of a surplus of events with $\chi_{\mathrm{eff}} > 0$ relative to those with $\chi_{\mathrm{eff}} < 0$ reported in GWTC-2 [8] and investigated further in a companion paper [122].

---

[2] In GWTC-2, GW190521 was inferred to have a total mass of $163.9^{+39.2}_{-23.5} M_\odot$ and remnant mass of $156.3^{+36.8}_{-22.4} M_\odot$ [8].

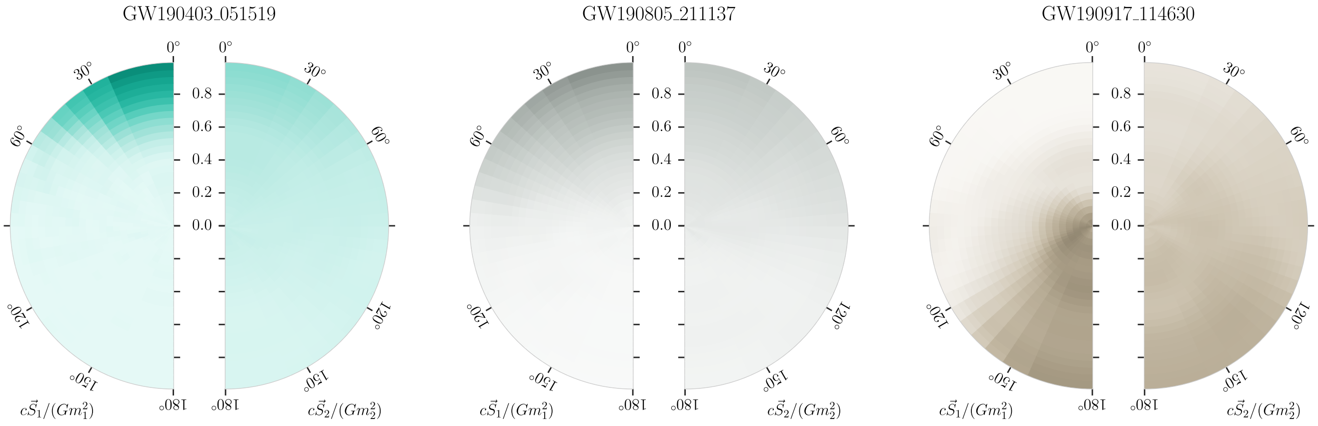

FIG. 6. The dimensionless spin parameters $\vec{\chi}_i = c\vec{S}_i/(Gm_i^2)$ estimated for individual binary components of selected sources. The radial distance of a given pixel on the left (right) of each disk, away from the center of the circle, corresponds to $|\vec{\chi}|$ for the more (less) massive compact object. Each pixel's angle from the vertical axis represents θ_{LS}, the angle between the spin vector $\vec{S}$ and the Newtonian orbital angular momentum. All pixels have equal prior probability with the shading denoting the relative posterior probability of the pixels, after marginalization over azimuthal angles. The events follow the same color scheme used in Fig. 3.

Similar to the compact objects reported in GWTC-2 [7,8], the majority of the compact-object spins reported in GWTC-2.1 have magnitudes consistent with zero. Two of the new events show evidence for large BH spins. In the case of GW190403_051519, 82% of the posterior probability lies in a region where at least one of the component spin magnitudes is above 0.8 whereas for GW190805_211137 this holds for 59% of the posterior probability.

For binaries with very unequal masses, measurements of χ_{eff} can translate into strong measurement constraints of χ_1, the spin magnitude of the more massive object, whose spin angular momentum dominates over the secondary. This is the case for GW190403_051519, whose primary dimensionless spin is measured to be $\chi_1 = 0.89^{+0.09}_{-0.31}$. This represents the most nearly extremal spin observed using GWs. Similarly, GW190805_211137 is recovered with $\chi_1 = 0.75^{+0.22}_{-0.59}$ and GW190917_114630 with $\chi_1 = 0.23^{+0.63}_{-0.21}$. Both GW190403_051519 and GW190805_211137 are recovered as strongly preferring large χ_1, with the inferred posterior distributions railing against the extremal BH-spin bound at $\chi_1 = 1$. Hence, we also report the one-sided 90% lower bounds of $\chi_1 > 0.69$ for GW190403_051519 and $\chi_1 > 0.29$ for GW190805_211137. The posterior distributions for the spin magnitudes and tilt angles for these three events are shown in Fig. 6.

3. Three-dimensional localization

As the eight new events are all detected at relatively modest SNRs, together with several identifications as high-mass BBHs, the inferred luminosity distances D_{L} are generally larger than the binaries from GWTC-2 [7,8]. GW190403_051519 is identified as probably the most distant event, with a recovered $D_{\mathrm{L}} = 8.28^{+6.72}_{-4.29}$ Gpc corresponding to a redshift $z = 1.18^{+0.73}_{-0.53}$ approximately twice as distant as the most distant events that were reported in GWTC-2 [7,8] as also shown in Appendix A 2. In addition GW190426_190642, GW190805_211137, GW190916_200658 and GW190926_050336 all have inferred distances comparable to, or larger than, GW190413_134308, further highlighting the access to the distant Universe provided in GWTC-2.1.

Another effect of the modest SNR of the new events is their comparatively poor localization on the sky. The best localized event is GW190805_211137 with a 90% credible region of $\Delta\Omega = 1600\ \mathrm{deg}^2$. The credible intervals for the inferred distances and sky areas are shown in Table VI. The inferred localizations for all events are available as part of the accompanying data release to this paper, detailed further in Sec. VII.

4. Waveform comparisons: Model systematics

The use of both the IMRPhenomXPHM [57–60] and SEOBNRv4PHM [61–63] models in the analyses of these events are motivated by the need to capture, and account for, potential differences in the inferred source parameters caused by the different methods used in the constructions of the models themselves. The vast majority of the posterior distributions reported in this section are constructed by combining an equal number of samples drawn from each of the IMRPhenomXPHM and SEOBNRv4PHM analyses [140]. For the majority of the eight new events, the differences between the two single-model analyses, as well as to the combined-model results, are found to be comparable to the impact of model systematics effects identified in GWTC-2 [7,8] being generally subdominant to the statistical uncertainty caused by the noisy data. For GW190403_051519 there are, however, slight differences identified between the IMRPhenomXPHM and

SEOBNRv4PHM analyses, most noticeably in the shape and structure of the marginal posterior distribution of some of the recovered mass and spin parameters. In these cases, the differences between analyses using either the IMRPhenomXPHM or SEOBNRv4PHM models are dominating over the other systematic uncertainties of the analysis, such as the estimation of the noise PSD. A deeper investigation into the broader impact of these model systematic effects, and their impact on the inferred source parameters for the population of GW events presented here, is left for a future study.

5. Comparison to 3-OGC

Out of the eight new events presented in this section, GW190725_174728, GW190916_200658, GW190925_232845 and GW190926_050336 were also independently identified and analyzed as part of 3-OGC [17] using the PyCBC Inference package [192] and the IMRPhenomXPHM waveform model. We compare the inferred source properties for these events as presented in 3-OGC [193] and, to minimize potential model systematic effects, the IMRPhenomXPHM analysis performed for GWTC-2.1 presented here. Overall, we find a broad agreement between the two analyses. While there are differences found in the two sets of posterior distributions, they appear consistent within expectations from the differing choices of the analysis configurations and the assumed prior distributions between the two analyses for low SNR signals [194].

VI. ASTROPHYSICAL IMPLICATIONS

Our analysis reports eight new candidates with $p_{\mathrm{astro}} > 0.5$ in at least one pipeline. None of these candidates have p_{astro} equal to 1 (Table II). Four of them were found only by a single analysis, and none were detected by all the pipelines (Table II). As discussed above in Sec. III A, p_{astro} values are subject to statistical uncertainties, and are also subject to uncertainties arising from the true rate and distribution of signals. Such uncertainties are larger for events which, if astrophysical, fall within populations with few or zero significant detections. Here, we highlight such uncertainties for specific candidates, and discuss possible astrophysical implications under the hypothesis that the candidates do originate from compact object mergers.

Parameter estimation indicates that two of the new candidates, GW190403_051519 and GW190426_190642, if astrophysical, have sources with a large total mass ($\gtrsim 100 M_\odot$, Table VI). Both were found only by the PyCBC-BBH, analysis with a low SNR and relatively low p_{astro}. They were also not recovered as significant events in the focused search of O3 data for intermediate-mass BH binaries [195]. Since there is only one significant detection to date of a comparable BBH system, GW190521 [196,197], the calculation of p_{astro} for these candidates is subject to significant potential systematic error. These events are confidently above the break mass in the broken power-law mass distribution model, at $39.7^{+20.3}_{-9.1} M_\odot$, or the Gaussian in the POWER LAW + PEAK model at $33.1^{+4.0}_{-5.6} M_\odot$ [122,198,199]. The estimated primary component masses, assuming astrophysical origin, are both above the lower edge of the pair-instability mass gap m_{low} [200–203], even considering the large uncertainties about its value (≈ 40–$70 M_\odot$, [32–40]). Adopting a conservative estimate of $m_{\mathrm{low}} = 65 M_\odot$, the primary component of GW190403_051519 ($m_1 = 85.0^{+27.8}_{-33.0} M_\odot$) has a probability 0.16 of being below m_{low} with our standard mass prior. Similarly, GW190426_190642's secondary component ($m_2 = 76.0^{+26.2}_{-36.5} M_\odot$) has a probability of 0.30 of being below m_{low}, while its primary component ($m_1 = 105.5^{+45.3}_{-24.1} M_\odot$) has a negligible probability of being below m_{low}. The upper edge of the mass gap is even more uncertain, with theoretical predictions suggesting $m_{\mathrm{up}} \approx 120 M_\odot$ [204,205]. The primary mass component of GW190403_051519 (GW190426_190642) has a probability 0.021 (0.25) of being above this value of m_{up}. Thus, if astrophysical, GW190403_051519 and GW190426_190642 lie in the same group with GW190521; their primary components might be either inside or above the mass gap. Moreover, the estimated final mass of the merger remnant of GW190426_190642 ($M_{\mathrm{f}} = 172.9^{+37.7}_{-33.6} M_\odot$) is in the intermediate-mass black hole regime (10^2–$10^5 M_\odot$).

These features are suggestive of a dynamical formation channel, such as the hierarchical merger of smaller BHs [206–217] or repeated stellar collisions in dense star clusters [218–221]. In active galactic nuclei, the dense gaseous disk surrounding the central BH also triggers the hierarchical assembly of BHs [222–228]. Alternatively, extreme gas accretion from a dense gaseous disk [229–231] or from a stellar companion [232] might assist the growth of BH mass above the pair-instability threshold. Finally, primordial BHs might also have masses in the pair-instability gap [233,234]. However, even the formation of BHs in this mass range from stellar collapse cannot be excluded, given the large uncertainties in stellar-evolution models [36,39,40,235–237]. For example, very massive ($\gtrsim 230 M_\odot$) extremely metal-poor ($Z < 10^{-4}$) stars might turn into BHs with mass above the pair-instability gap [238–241].

Parameter-estimation analysis indicates a large positive value of the effective inspiral spin $\chi_{\mathrm{eff}} = 0.68^{+0.16}_{-0.43}$ and of the primary's spin magnitude $\chi_1 = 0.89^{+0.09}_{-0.31}$ for GW190403_051519. From a theoretical perspective, BH spin magnitudes are highly uncertain [235,242], with some models [243,244] predicting very low spins (~ 0.01) for single BHs because of efficient angular momentum transport in the stellar interior [245]. Observations of high-mass x-ray binaries in the local Universe indicate that BH spins can be nearly maximal [246,247], while the majority of mergers in GWTC-2 are associated with low values of χ_{eff}, with a slight preference for positive values [122]. Even if single stars form BHs with low spins [244], BHs in binaries may still develop high spins because of mass transfer [248], tidal interactions [242,249,250], or chemically homogeneous evolution [251,252]. Alternatively, BHs born from the merger of two smaller BHs are expected to have high natal spins (~0.7–0.9, [147,148,150]). This might suggest that the primary component of GW190403_051519 is a second-generation BH, which is also consistent with its large mass [208,209,217,253,254]. However, the positive effective inspiral spin χ_{eff} of GW190403_051519 indicates a significant alignment of the spin vectors of (any of) the two components with the orbital angular momentum vector of the BBH. Nearly aligned spins are preferentially associated with isolated binary evolution [255,256], while dynamically formed binaries tend to have an isotropically distributed spin orientations [257,258].

Finally, GW190403_051519 is associated with a comparatively small mass ratio q (Fig. 3). Such low values of the mass ratio are unusual in isolated binary evolution, especially for the chemically homogeneous evolution [251,259] but also for the common-envelope scenario [235,260–263]. In contrast, low mass ratios are expected if the primary and secondary components are a second- and a first-generation BH, respectively [211,212,214], or if the primary BH is the result of a stellar merger in a young star cluster [219].

Four of the other new candidates (GW190805_211137, GW190916_200658, GW190925_232845, GW190926_050336) fall in the mass range of the bulk of GWTC-2 BBHs, while the secondary component of GW190725_174728 has a 0.18 probability of lying in the lower mass gap (~ 2–$5 M_\odot$). The existence of a lower mass gap was inferred from observations of Galactic x-ray binaries [264–266], but there are a few observations of BHs with mass ≈ 3–$4 M_\odot$ in noninteracting binary systems [267,268] and microlensing surveys find no evidence for a mass gap between NSs and BHs [269,270]. GWTC-2 BBH observations also suggest a dearth of systems between $2.6 M_\odot$ and $6 M_\odot$ [122,271]. The only confirmed GW event in GWTC-2 with a component in the lower mass gap is GW190814 [41]. Numerical and theoretical models do not exclude the formation of compact objects in this mass range from a core-collapse supernova [272–275]. Other scenarios to explain the formation of binary compact objects in this mass range include mergers in multiple systems [276–279], primordial BHs [233,280] and mass accretion onto a neutron star [281].

Finally, GW190917_114630 has component masses consistent with an NSBH ($m_1 = 9.7^{+3.4}_{-3.9} M_\odot$, $m_2 = 2.1^{+1.1}_{-0.4} M_\odot$), but was identified only as a BBH candidate, with $p_{\mathrm{NSBH}} = 0$ and $p_{\mathrm{BBH}} = 0.77$, by the pipeline that detected it (GstLAL). Since GW190426_152155 is a marginal candidate in this catalog, due to its low p_{astro} (Table IV), GW190917_114630 is the only high-probability candidate with mass components in the NSBH range. However, as discussed in Sec. IVA, had it been classified as an NSBH to begin with, its p_{astro} measured by GstLAL would have been smaller due to the lower foreground rate of NSBHs as compared to BBHs in the detection pipelines, and not passed the threshold of 0.5 considered by the followup pipelines. As with the unusually high-mass BBH candidates, the assignment of p_{astro} for NSBHs is subject to potential systematic error since no NSBH events have been confidently detected in the data set up to O3a used here, although there were NSBH discoveries in O3b [67,134]. The masses and effective inspiral spin of this candidate are consistent with prior expectations for NSBH systems [260,282–288]. Inferring the impact on the overall population of binary compact objects of the new candidates, including those with non-negligible probability of noise origin, requires a more involved analysis which is beyond this scope of this work [289,290].

VII. CONCLUSION

We have presented GWTC-2.1, which includes results from a refined search for CBCs in the first part of the third observing run of the Advanced LIGO and Advanced Virgo detectors. This is an extension to the previous GW catalog, GWTC-2 [8], over the same data, and provides a deeper list of GW candidates. The search we presented here was carried out using three matched-filter pipelines, MBTA, GstLAL, and PyCBC, and includes a list of candidates that have a FAR less than 2 per day in any of the pipelines. We provide detailed source properties of the eight events that have p_{astro} greater than 0.5 and were not present in GWTC-2. In addition, the source properties of previously reported events with p_{astro} greater than 0.5 are presented in the Appendix.

Out of the eight new candidates presented here, all events have masses consistent with BBH sources with the exception of GW190917_114630, whose source masses are consistent with being an NSBH (Sec. V D). If astrophysical, these events expand the scope of observed BBHs, with several binaries inferred at larger distances than previous detections and with both a new broader range of recovered BH masses and the addition of two binaries with significantly unequal masses. The primary components of two of the new candidates (GW190403_051519 and GW190426_190642) lie inside or, less likely, above the pair-instability mass gap. GW190403_051519 also shows support for high-spin, unequal masses, and remnant mass in the intermediate-mass BH regime. These features are suggestive of dynamical formation, by hierarchical BH merger or by stellar collisions in dense stellar clusters or active galactic nuclei. However, we cannot exclude that GW190403_051519 and GW190426_190642 originated from isolated binary systems, because of the large uncertainties in the mass range of the pair-instability mass gap. Among the new candidates, GW190725_174728 shows some support for a secondary component mass in the lower mass gap ($2 - 5M_\odot$). GW190917_114630, the only candidate with component masses consistent with an NSBH was initially classified as a BBH by the search pipeline, and therefore the p_astro assigned to it is subject to systematics due to uncertainty in classification.

The data products associated with GWTC-2.1 include candidate information from relevant search pipeline(s) and localizations for all events that pass a threshold of 2 per day in any search pipeline. The information from each search pipeline includes the template mass and spin parameters, the SNR time series, chi-squared values, the time and phase of coalescence in each detector, FAR, and p_astro (Sec. III A). These data can be found at Zenodo [104]. The source localizations are computed using the rapid localization tool BAYESTAR [291,292], which was also used to produce the localizations in near real time during the observing runs while sending out GW alerts. We also release the results of the search pipelines running over simulated signal sets classified as BNS, NSBH, and BBH [131] that were used to calculate the sensitivities shown in Table V. For candidates that have a $p_\mathrm{astro} > 0.5$, we perform followup parameter estimation and also release the posterior samples associated with these events. These are available via Zenodo [183]. Finally, the strain data for O3a used for the analyses in this paper are also available [44,47].

The LVK have already announced the first observations from NSBHs [134] in the data from O3b, and the catalog that extends events up to O3b, GWTC-3 [67], has been released. GWTC-3 adds 35 GW candidates with p_astro greater than 0.5 from O3b. O3 marks the most sensitive GW data published upon so far. The LIGO, Virgo, and KAGRA [293] detectors are currently offline and undergoing commissioning to enhance their sensitivities, and plan to all collect data simultaneously during the fourth observing run (O4) [68]. With further improvement in sensitivities and planning for premerger BNS detections [294–296], O4 offers improved prospects for GW and multimessenger astronomy, and promises to build upon our current knowledge of binary populations.

ACKNOWLEDGMENTS

This material is based upon work supported by NSF's LIGO Laboratory which is a major facility fully funded by the National Science Foundation. The authors also gratefully acknowledge the support of the Science and Technology Facilities Council (STFC) of the United Kingdom, the Max-Planck-Society (MPS), and the State of Niedersachsen/Germany for support of the construction of Advanced LIGO and construction and operation of the GEO600 detector. Additional support for Advanced LIGO was provided by the Australian Research Council. The authors gratefully acknowledge the Italian Istituto Nazionale di Fisica Nucleare (INFN), the French Centre National de la Recherche Scientifique (CNRS) and the Netherlands Organization for Scientific Research, for the construction and operation of the Virgo detector and the creation and support of the EGO consortium. The authors also gratefully acknowledge research support from these agencies as well as by the Council of Scientific and Industrial Research of India, the Department of Science and Technology, India, the Science & Engineering Research Board (SERB), India, the Ministry of Human Resource Development, India, the Spanish Agencia Estatal de Investigación, the Vicepresidència i Conselleria d'Innovació, Recerca i Turisme and the Conselleria d'Educació i Universitat del Govern de les Illes Balears, the Conselleria d'Innovació, Universitats, Ciència i Societat Digital de la Generalitat Valenciana and the CERCA Programme Generalitat de Catalunya, Spain, the National Science Centre of Poland and the Foundation for Polish Science (FNP), the Swiss National Science Foundation (SNSF), the Russian Foundation for Basic Research, the Russian Science Foundation, the European Commission, the European Regional Development Funds (ERDF), the Royal Society, the Scottish Funding Council, the Scottish Universities Physics Alliance, the Hungarian Scientific Research Fund (OTKA), the French Lyon Institute of Origins (LIO), the Belgian Fonds de la Recherche Scientifique (FRS-FNRS), Actions de Recherche Concertées (ARC) and Fonds Wetenschappelijk Onderzoek—Vlaanderen (FWO), Belgium, the Paris Île-de-France Region, the National Research, Development and Innovation Office Hungary (NKFIH), the National Research Foundation of Korea, the Natural Science and Engineering Research Council Canada, Canadian Foundation for Innovation (CFI), the Brazilian Ministry of Science, Technology, and Innovations, the International Center for Theoretical Physics South American Institute for Fundamental Research (ICTP-SAIFR), the Research Grants Council of Hong Kong, the National Natural Science Foundation of China (NSFC), the Leverhulme Trust, the Research Corporation, the Ministry of Science and Technology (MOST), Taiwan, the United States Department of Energy, and the Kavli Foundation. The authors gratefully acknowledge the support of the NSF, STFC, INFN and CNRS for provision of computational resources. Additional acknowledgements for support of individual authors may be found in the following document [297]. For the purpose of open access, the authors have applied a Creative Commons Attribution (CC BY) license to any Author Accepted Manuscript version arising. We request that citations to this article use "R. Abbott *et al.* (LIGO - Virgo Collaboration), ..." or similar phrasing, depending on journal convention. We thank the anonymous journal referee (s) for helpful comments. *We would like to thank all of the essential workers who put their health at risk during the COVID-19 pandemic, without whom we would not have been able to complete this work.* Analyses in this catalog relied upon the LALSuite software library [171]. The detection of the signals and subsequent significance evaluations were performed with the GstLAL -based inspiral software pipeline [48–50,298], with the MBTA pipeline [56,299], and with the PyCBC [54,55,102,124] package. Estimates of the noise spectra and glitch models were obtained using BayesWave [93,96,300]. Source parameter estimation was performed with the Bilby library [142,166] using the DYNESTY nested sampling package [301], the RIFT library [172–174] and the LALInference library [139]. PESummary was used to post-process and collate parameter-estimation results [177]. The various stages of the parameter-estimation analysis were managed with the Asimov library [176]. Plots were prepared with Matplotlib [302], SEABORN [303] and GWpy [88]. NumPy [304] and SciPy [305] were used in the preparation of the manuscript.

APPENDIX: ESTIMATION OF SOURCE PARAMETERS

1. Binary black holes from the first and second observing runs

In order to provide a self-consistent set of source properties, inferred using the state-of-the-art BBH waveform models described in Sec. V A, we have reanalyzed the 10 BBH events observed during O1 and O2, and reported in GWTC-1 [7]. We present results combining samples from analyses using both the IMRPhenomXPHM and SEOBNRv4PHM, with the exception of GW151226 which, as mentioned earlier in Sec. V D, was analyzed using IMRPhenomXPHM only. As the BNS models available at the time of GWTC-1 still can be considered state-of-the-art in the NS-physics they describe, we have elected to not reanalyze the BNS event GW170817 as part of this study. For the source properties of GW170817, we instead refer to GWTC-1 [7] and its accompanying data release [306].

The source properties for the 10 BBH events from the O1 and O2 are reported in Table VII, with a selection of the one-dimensional marginal posterior distributions shown in Fig. 7. The two-dimensional projections on the M–q and $\mathcal{M}$–$\chi_{\rm eff}$ planes are shown as light-gray contours in Figs. 4 and 5 respectively. The full 15-dimensional posterior distributions are available as part of the public data release accompanying this paper [183], as detailed further in Sec. VII.

Generally, the inferred source properties for these ten BBHs are consistent with those presented in GWTC-1 [7], but there are some new features worth highlighting. Where most binaries have a nominal support for $\chi_{\rm eff} = 0$, GW151226 was in GWTC-1 identified to exclude this value at $> 90\%$ probability [7,307], a conclusion which is strengthened further as of the analysis presented here in GWTC-2.1. The other BBH in GWTC-1 with only marginal support for $\chi_{\rm eff} = 0$, GW170729, is now found to include support for negative $\chi_{\rm eff}$ in its 90% credible interval while also simultaneously preferring BH components with more unequal masses relative to what was inferred in GWTC-1.

Previous independent analyses of these ten events with the IMRPhenomXPHM model show broad consistency with the results presented in this section [308].

2. Previously reported binaries from the first half of the third observing run

The high-significance events from O3a are reported in Table II. Out of these events, 36 were included in GWTC-2 [8] with its accompanying data release [309]. Again, to

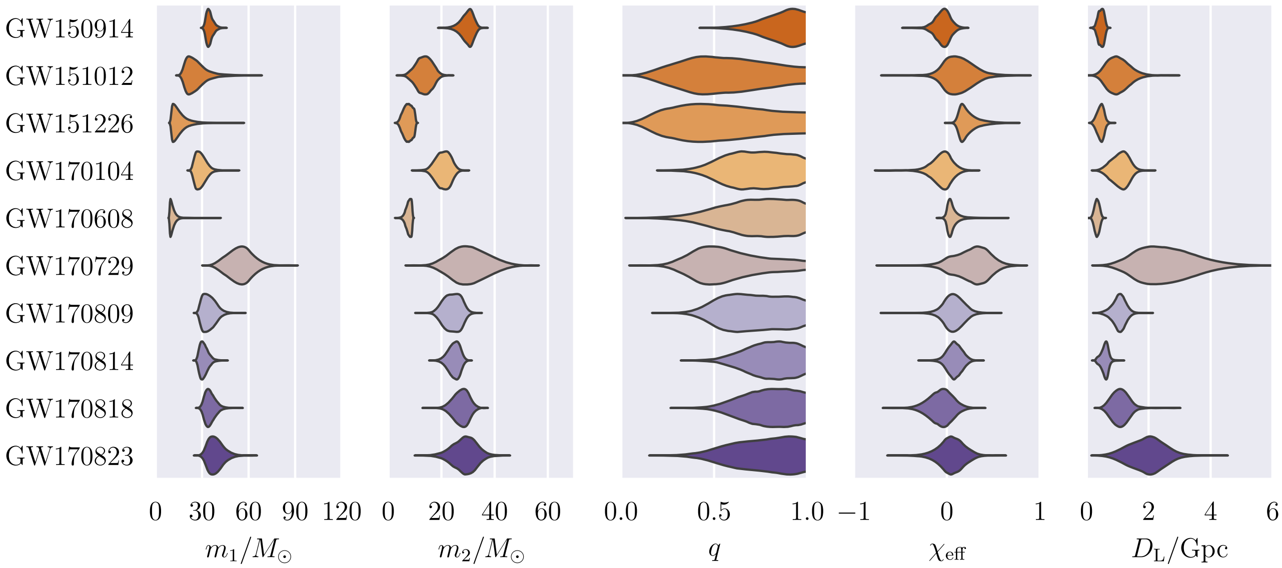

FIG. 7. Marginal posterior distributions on the primary mass m_1, secondary mass m_2, mass ratio q, effective inspiral spin $\chi_{\rm eff}$ and luminosity distance $D_{\rm L}$ for the 10 BBH events observed during O1 and O2. The vertical span for each region is constructed to be proportional to the one-dimensional marginal posterior at a given parameter value for the corresponding event. The posterior distributions are also represented numerically in terms of their one-dimensional median and 90% credible intervals in Table VII.

TABLE VII. Median and 90% symmetric credible intervals for the one-dimensional marginal posterior distributions on selected source parameters for the 10 BBH events observed during the O1 and O2. These binaries were reported in GWTC-1 [7]. The columns show source total mass M, chirp mass $\mathcal{M}$ and component masses m_i, dimensionless effective inspiral spin χ_{eff}, luminosity distance D_{L}, redshift z, final mass M_f, final spin χ_{f}, sky localization $\Delta\Omega$ and the network matched-filter SNR. The sky localization is the area of the 90% credible region. All quoted results are calculated from a set of posterior samples drawn with equal weight from the IMRPhenomXPHM and SEOBNRv4PHM analyses, with the exception of the SNRs that are taken from the IMRPhenomXPHM analysis alone (as RIFT, which was used for the SEOBNRv4PHM analysis, does not output that quantity). Additionally, following Sec. V D, the results presented for GW151226 are taken from an analysis using the IMRPhenomXPHM model only. A subset of the one-dimensional posterior distributions are visualized in Fig. 7. Two-dimensional projections of the 90% credible regions in the M–q and $\mathcal{M}$–χ_{eff} planes are shown in gray in Figs. 4 and 5.

Event	M $(M_\odot)$	$\mathcal{M}$ $(M_\odot)$	m_1 $(M_\odot)$	m_2 $(M_\odot)$	χ_{eff}	D_{L} (Gpc)	z	M_{f} $(M_\odot)$	χ_{f}	$\Delta\Omega$ (deg^2)	SNR
GW150914	$64.5^{+3.7}_{-3.2}$	$27.9^{+1.7}_{-1.5}$	$34.6^{+4.4}_{-2.6}$	$30.0^{+2.9}_{-4.6}$	$-0.04^{+0.12}_{-0.14}$	$0.47^{+0.14}_{-0.16}$	$0.10^{+0.03}_{-0.03}$	$61.5^{+3.4}_{-2.9}$	$0.68^{+0.05}_{-0.05}$	250	$26.05^{+0.1}_{-0.2}$
GW151012	$38.8^{+10.3}_{-4.7}$	$15.6^{+2.3}_{-1.5}$	$24.8^{+14.5}_{-6.3}$	$13.6^{+4.5}_{-4.9}$	$0.12^{+0.28}_{-0.21}$	$1.00^{+0.64}_{-0.49}$	$0.20^{+0.11}_{-0.09}$	$37.1^{+10.6}_{-4.6}$	$0.69^{+0.13}_{-0.13}$	1700	$9.3^{+0.3}_{-0.5}$
GW151226	$21.7^{+8.3}_{-1.6}$	$8.9^{+0.3}_{-0.3}$	$14.2^{+11.1}_{-3.6}$	$7.5^{+2.4}_{-2.8}$	$0.20^{+0.23}_{-0.08}$	$0.46^{+0.16}_{-0.20}$	$0.10^{+0.03}_{-0.04}$	$20.7^{+8.6}_{-1.6}$	$0.75^{+0.12}_{-0.05}$	950	$12.7^{+0.3}_{-0.4}$
GW170104	$49.6^{+4.7}_{-3.6}$	$21.1^{+2.0}_{-1.5}$	$28.7^{+6.6}_{-4.2}$	$20.8^{+4.1}_{-4.7}$	$-0.04^{+0.15}_{-0.19}$	$1.11^{+0.39}_{-0.48}$	$0.22^{+0.07}_{-0.09}$	$47.5^{+4.5}_{-3.4}$	$0.67^{+0.06}_{-0.08}$	1000	$13.8^{+0.2}_{-0.3}$
GW170608	$18.5^{+2.0}_{-0.6}$	$7.9^{+0.2}_{-0.2}$	$10.6^{+4.0}_{-1.4}$	$7.8^{+1.2}_{-1.9}$	$0.05^{+0.13}_{-0.05}$	$0.34^{+0.12}_{-0.13}$	$0.07^{+0.03}_{-0.03}$	$17.7^{+2.1}_{-0.6}$	$0.69^{+0.03}_{-0.03}$	380	$15.3^{+0.2}_{-0.3}$
GW170729	$84.4^{+15.0}_{-10.9}$	$34.6^{+7.0}_{-5.7}$	$54.7^{+12.7}_{-12.8}$	$30.2^{+11.9}_{-10.2}$	$0.29^{+0.25}_{-0.33}$	$2.49^{+1.69}_{-1.23}$	$0.44^{+0.24}_{-0.19}$	$80.3^{+13.5}_{-10.2}$	$0.78^{+0.09}_{-0.22}$	830	$10.7^{+0.4}_{-0.5}$
GW170809	$58.5^{+5.3}_{-3.9}$	$24.8^{+2.2}_{-1.6}$	$34.1^{+8.0}_{-5.3}$	$24.2^{+4.8}_{-5.3}$	$0.07^{+0.17}_{-0.17}$	$1.07^{+0.31}_{-0.38}$	$0.21^{+0.05}_{-0.07}$	$55.7^{+5.0}_{-3.6}$	$0.71^{+0.08}_{-0.08}$	260	$12.8^{+0.2}_{-0.3}$
GW170814	$56.0^{+3.5}_{-3.0}$	$24.1^{+1.4}_{-1.2}$	$30.9^{+5.4}_{-3.3}$	$24.9^{+3.0}_{-4.0}$	$0.08^{+0.13}_{-0.12}$	$0.61^{+0.16}_{-0.23}$	$0.13^{+0.03}_{-0.05}$	$53.2^{+3.2}_{-2.7}$	$0.72^{+0.07}_{-0.06}$	92	$17.7^{+0.2}_{-0.3}$
GW170818	$62.5^{+5.3}_{-4.6}$	$26.8^{+2.3}_{-2.0}$	$34.8^{+6.5}_{-4.2}$	$27.6^{+4.1}_{-5.1}$	$-0.06^{+0.19}_{-0.22}$	$1.08^{+0.43}_{-0.41}$	$0.21^{+0.07}_{-0.07}$	$59.7^{+4.9}_{-4.2}$	$0.68^{+0.08}_{-0.08}$	35	$12.0^{+0.3}_{-0.4}$
GW170823	$67.0^{+10.3}_{-7.2}$	$28.6^{+4.5}_{-3.3}$	$38.3^{+9.5}_{-6.2}$	$29.0^{+6.5}_{-7.8}$	$0.05^{+0.21}_{-0.22}$	$1.97^{+0.84}_{-0.93}$	$0.36^{+0.13}_{-0.15}$	$63.9^{+9.6}_{-6.8}$	$0.71^{+0.08}_{-0.10}$	1800	$12.2^{+0.2}_{-0.3}$

ensure a self-consistent set of inferred source properties available for all CBC events observed by Advanced LIGO and Advanced Virgo, we provide a reanalysis of these 36 events using the BBH waveform models described in Sec. V A. We present results combining samples from analyses using both the IMRPhenomXPHM and SEOBNRv4PHM, with the exception of GW190413_052954, GW190413_134308, GW190421_213856, GW190521, GW190602_175927, GW190719_215514, GW190803_022701, GW190814, GW190828_063405, GW190828_065509 and GW190929_012149 which, as mentioned earlier in Sec. V D, were analyzed using IMRPhenomXPHM only. As also described in Sec. V A, for the BNS event GW190425, the IMRPhenomP_NRTidal waveform model [65,66] was used. The analyses of these events also used the GW strain data described in Sec. II A, an additional improvement over the analyses presented in GWTC-2 [8]. For the events listed in Table I all analyses made use of data which included glitch subtraction or a reduction in the bandwidth available for astrophysical inference.

The source properties for the 36 events from O3a are reported in Table VIII, with a selection of the

TABLE VIII. Median and 90% symmetric credible intervals for the one-dimensional marginal posterior distributions on selected source parameters for the 36 events from Table II that were not reported in Table VI. The columns show source total mass M, chirp mass $\mathcal{M}$ and component masses m_i, dimensionless effective inspiral spin χ_{eff}, luminosity distance D_{L}, redshift z, final mass M_{F} final spin χ_{f}, sky localization $\Delta\Omega$ and the network matched-filter SNR. The sky localization is the area of the 90% credible region. The results for the BBHs are calculated from a set of posterior samples drawn with equal weight from the IMRPhenomXPHM and SEOBNRv4PHM analyses, with the exception of the SNRs that are taken from the IMRPhenomXPHM analysis alone (as RIFT, which was used for the SEOBNRv4PHM analysis, does not output that quantity). Additionally, following Sec. V D, the results for GW190413_052954, GW190413_134308, GW190421_213856, GW190521, GW190602_175927, GW190719_215514, GW190803_022701, GW190814, GW190828_063405, GW190828_065509, and GW190929_012149 are from analyses using the IMRPhenomXPHM model only. For GW190425, we report results from the high-spin ($|\vec{\chi}_1| < 0.89$) analysis, and since the calculation of the BH remnant properties is only valid for BBH model input those properties are excluded for this BNS signal. A subset of the one-dimensional posterior distributions are visualized in Fig. 8. Two-dimensional projections of the 90% credible regions in the M–q and $\mathcal{M}$–χ_{eff} planes are shown in gray in Figs. 4 and 5.

Event	M $(M_\odot)$	$\mathcal{M}$ $(M_\odot)$	m_1 $(M_\odot)$	m_2 $(M_\odot)$	χ_{eff}	D_{L} (Gpc)	z	M_{f} $(M_\odot)$	χ_{f}	$\Delta\Omega$ (deg^2)	SNR
GW190408_181802	$43.4^{+4.2}_{-3.0}$	$18.5^{+1.9}_{-1.2}$	$24.8^{+5.4}_{-3.5}$	$18.5^{+3.3}_{-4.0}$	$-0.03^{+0.13}_{-0.17}$	$1.54^{+0.44}_{-0.62}$	$0.29^{+0.07}_{-0.11}$	$41.4^{+3.9}_{-2.9}$	$0.67^{+0.06}_{-0.07}$	290	$14.6^{+0.2}_{-0.3}$
GW190412	$36.8^{+4.7}_{-4.4}$	$13.3^{+0.5}_{-0.5}$	$27.7^{+6.0}_{-6.0}$	$9.0^{+2.0}_{-1.4}$	$0.21^{+0.12}_{-0.13}$	$0.72^{+0.24}_{-0.22}$	$0.15^{+0.04}_{-0.04}$	$35.6^{+4.8}_{-4.5}$	$0.66^{+0.05}_{-0.04}$	240	$19.8^{+0.2}_{-0.3}$
GW190413_052954	$58.0^{+10.6}_{-7.8}$	$24.5^{+4.6}_{-3.4}$	$33.7^{+10.4}_{-6.4}$	$24.2^{+6.5}_{-7.0}$	$-0.04^{+0.27}_{-0.32}$	$3.32^{+1.91}_{-1.40}$	$0.56^{+0.25}_{-0.21}$	$55.5^{+10.1}_{-7.3}$	$0.67^{+0.10}_{-0.12}$	650	$9.0^{+0.4}_{-0.8}$

(Table continued)

TABLE VIII. *(Continued)*

Event	M ($M_\odot$)	$\mathcal{M}$ ($M_\odot$)	m_1 ($M_\odot$)	m_2 ($M_\odot$)	$\chi_{\rm eff}$	$D_{\rm L}$ (Gpc)	z	$M_{\rm f}$ ($M_\odot$)	$\chi_{\rm f}$	$\Delta\Omega$ (deg^2)	SNR
GW190413_134308	$81.3^{+16.8}_{-11.8}$	$33.3^{+7.8}_{-6.3}$	$51.3^{+16.6}_{-12.6}$	$30.4^{+11.7}_{-12.7}$	$-0.01^{+0.28}_{-0.38}$	$3.80^{+2.48}_{-1.83}$	$0.62^{+0.32}_{-0.26}$	$78.0^{+16.1}_{-11.5}$	$0.68^{+0.12}_{-0.18}$	630	$10.6^{+0.4}_{-0.5}$
GW190421_213856	$73.6^{+13.2}_{-9.5}$	$31.4^{+6.0}_{-4.6}$	$42.0^{+10.1}_{-7.4}$	$32.0^{+8.3}_{-9.8}$	$-0.10^{+0.21}_{-0.27}$	$2.59^{+1.49}_{-1.24}$	$0.45^{+0.21}_{-0.19}$	$70.5^{+12.4}_{-9.0}$	$0.66^{+0.09}_{-0.12}$	1200	$10.7^{+0.2}_{-0.4}$
GW190425	$3.4^{+0.3}_{-0.1}$	$1.44^{+0.02}_{-0.02}$	$2.1^{+0.5}_{-0.4}$	$1.3^{+0.3}_{-0.2}$	$0.07^{+0.07}_{-0.05}$	$0.15^{+0.08}_{-0.06}$	$0.03^{+0.02}_{-0.01}$	…	…	8700	$12.4^{+0.4}_{-0.4}$
GW190503_185404	$69.4^{+10.1}_{-8.6}$	$29.3^{+4.5}_{-4.4}$	$41.3^{+10.3}_{-7.7}$	$28.3^{+7.5}_{-9.2}$	$-0.05^{+0.23}_{-0.30}$	$1.52^{+0.63}_{-0.60}$	$0.29^{+0.10}_{-0.10}$	$66.5^{+9.4}_{-7.9}$	$0.66^{+0.09}_{-0.15}$	100	$12.2^{+0.2}_{-0.4}$
GW190512_180714	$35.8^{+4.1}_{-3.5}$	$14.6^{+1.4}_{-0.9}$	$23.2^{+5.6}_{-5.6}$	$12.5^{+3.5}_{-2.6}$	$0.02^{+0.13}_{-0.14}$	$1.46^{+0.51}_{-0.59}$	$0.28^{+0.08}_{-0.10}$	$34.3^{+4.1}_{-3.4}$	$0.65^{+0.06}_{-0.07}$	230	$12.7^{+0.3}_{-0.4}$
GW190513_205428	$54.4^{+9.3}_{-6.7}$	$21.8^{+3.8}_{-2.2}$	$36.0^{+10.6}_{-9.7}$	$18.3^{+7.4}_{-4.7}$	$0.16^{+0.29}_{-0.22}$	$2.21^{+0.99}_{-0.81}$	$0.40^{+0.14}_{-0.13}$	$52.1^{+8.8}_{-6.6}$	$0.71^{+0.13}_{-0.13}$	450	$12.5^{+0.3}_{-0.4}$
GW190514_065416	$69.3^{+19.8}_{-12.1}$	$29.1^{+8.1}_{-5.4}$	$40.9^{+17.3}_{-9.3}$	$28.4^{+10.0}_{-10.1}$	$-0.08^{+0.29}_{-0.35}$	$3.89^{+2.61}_{-2.07}$	$0.64^{+0.33}_{-0.30}$	$66.4^{+19.0}_{-11.5}$	$0.66^{+0.12}_{-0.16}$	3400	$8.0^{+0.3}_{-0.6}$
GW190517_055101	$64.1^{+9.9}_{-9.8}$	$26.5^{+4.0}_{-4.2}$	$39.2^{+13.9}_{-9.2}$	$24.0^{+7.4}_{-7.9}$	$0.49^{+0.21}_{-0.28}$	$1.79^{+1.75}_{-0.88}$	$0.33^{+0.26}_{-0.15}$	$60.1^{+9.9}_{-9.4}$	$0.87^{+0.05}_{-0.07}$	510	$10.8^{+0.5}_{-0.6}$
GW190519_153544	$105.6^{+14.4}_{-13.9}$	$44.3^{+6.8}_{-7.5}$	$65.1^{+10.8}_{-11.0}$	$40.8^{+11.5}_{-12.7}$	$0.33^{+0.20}_{-0.24}$	$2.60^{+1.72}_{-0.96}$	$0.45^{+0.24}_{-0.15}$	$100.0^{+13.0}_{-12.9}$	$0.79^{+0.07}_{-0.12}$	570	$15.9^{+0.2}_{-0.3}$
GW190521	$153.1^{+42.2}_{-16.2}$	$63.3^{+19.6}_{-14.6}$	$98.4^{+33.6}_{-21.7}$	$57.2^{+27.1}_{-30.1}$	$-0.14^{+0.50}_{-0.45}$	$3.31^{+2.79}_{-1.80}$	$0.56^{+0.36}_{-0.27}$	$147.4^{+40.0}_{-16.0}$	$0.62^{+0.21}_{-0.23}$	1000	$14.3^{+0.5}_{-0.4}$
GW190521_074359	$76.3^{+7.0}_{-5.9}$	$32.8^{+3.2}_{-2.8}$	$43.4^{+5.8}_{-5.5}$	$33.4^{+5.2}_{-6.8}$	$0.10^{+0.13}_{-0.13}$	$1.08^{+0.58}_{-0.53}$	$0.21^{+0.10}_{-0.10}$	$72.6^{+6.5}_{-5.4}$	$0.71^{+0.06}_{-0.06}$	470	$25.9^{+0.1}_{-0.2}$
GW190527_092055	$58.1^{+18.1}_{-8.8}$	$23.9^{+6.8}_{-3.9}$	$35.6^{+18.7}_{-8.0}$	$22.2^{+9.0}_{-8.7}$	$0.10^{+0.22}_{-0.22}$	$2.52^{+2.08}_{-1.23}$	$0.44^{+0.29}_{-0.19}$	$55.5^{+17.9}_{-8.5}$	$0.71^{+0.10}_{-0.16}$	3500	$8.0^{+0.4}_{-0.9}$
GW190602_175927	$115.6^{+19.2}_{-14.8}$	$48.0^{+9.5}_{-9.7}$	$71.8^{+18.1}_{-14.6}$	$44.8^{+15.5}_{-19.6}$	$0.12^{+0.25}_{-0.28}$	$2.84^{+1.93}_{-1.28}$	$0.49^{+0.26}_{-0.20}$	$110.5^{+17.9}_{-13.9}$	$0.72^{+0.11}_{-0.17}$	740	$13.2^{+0.2}_{-0.3}$
GW190620_030421	$92.7^{+18.5}_{-13.2}$	$38.1^{+8.5}_{-7.2}$	$58.0^{+19.2}_{-13.3}$	$35.0^{+13.1}_{-14.5}$	$0.34^{+0.22}_{-0.29}$	$2.91^{+1.71}_{-1.32}$	$0.50^{+0.23}_{-0.20}$	$88.0^{+17.2}_{-12.4}$	$0.80^{+0.07}_{-0.15}$	7700	$12.1^{+0.3}_{-0.4}$
GW190630_185205	$59.4^{+4.7}_{-4.8}$	$25.1^{+2.2}_{-2.1}$	$35.1^{+6.5}_{-5.5}$	$24.0^{+5.5}_{-5.2}$	$0.10^{+0.14}_{-0.13}$	$0.87^{+0.53}_{-0.36}$	$0.18^{+0.09}_{-0.07}$	$56.6^{+4.4}_{-4.5}$	$0.70^{+0.06}_{-0.07}$	670	$16.4^{+0.2}_{-0.3}$
GW190701_203306	$94.3^{+12.0}_{-9.5}$	$40.2^{+5.4}_{-5.0}$	$54.1^{+12.6}_{-8.0}$	$40.5^{+8.7}_{-12.1}$	$-0.08^{+0.23}_{-0.31}$	$2.09^{+0.77}_{-0.74}$	$0.38^{+0.11}_{-0.12}$	$90.2^{+11.2}_{-8.9}$	$0.66^{+0.09}_{-0.13}$	45	$11.2^{+0.2}_{-0.4}$
GW190706_222641	$112.6^{+27.4}_{-16.8}$	$45.6^{+13.0}_{-9.1}$	$74.0^{+20.1}_{-16.9}$	$39.4^{+18.4}_{-15.4}$	$0.28^{+0.25}_{-0.31}$	$3.63^{+2.60}_{-2.00}$	$0.60^{+0.33}_{-0.29}$	$107.3^{+25.2}_{-15.9}$	$0.78^{+0.09}_{-0.19}$	2600	$13.4^{+0.2}_{-0.4}$
GW190707_093326	$20.1^{+1.7}_{-1.2}$	$8.4^{+0.6}_{-0.4}$	$12.1^{+2.6}_{-2.0}$	$7.9^{+1.6}_{-1.3}$	$-0.04^{+0.10}_{-0.09}$	$0.85^{+0.34}_{-0.40}$	$0.17^{+0.06}_{-0.08}$	$19.2^{+1.7}_{-1.2}$	$0.66^{+0.03}_{-0.03}$	1200	$13.1^{+0.2}_{-0.4}$
GW190708_232457	$31.4^{+2.8}_{-2.2}$	$13.1^{+0.9}_{-0.6}$	$19.8^{+4.3}_{-4.3}$	$11.6^{+3.1}_{-2.0}$	$0.05^{+0.10}_{-0.10}$	$0.93^{+0.31}_{-0.39}$	$0.19^{+0.06}_{-0.07}$	$30.1^{+2.9}_{-2.1}$	$0.68^{+0.04}_{-0.05}$	11000	$13.4^{+0.2}_{-0.3}$
GW190719_215514	$57.2^{+38.4}_{-11.6}$	$22.8^{+8.3}_{-4.3}$	$36.6^{+42.1}_{-11.1}$	$19.9^{+10.0}_{-9.3}$	$0.25^{+0.33}_{-0.32}$	$3.73^{+3.12}_{-2.07}$	$0.61^{+0.39}_{-0.30}$	$54.5^{+38.3}_{-11.1}$	$0.76^{+0.13}_{-0.18}$	3600	$7.9^{+0.3}_{-0.7}$
GW190720_000836	$21.8^{+3.8}_{-2.0}$	$9.0^{+0.4}_{-0.8}$	$14.2^{+5.6}_{-3.3}$	$7.5^{+2.2}_{-1.8}$	$0.19^{+0.14}_{-0.11}$	$0.77^{+0.65}_{-0.26}$	$0.16^{+0.11}_{-0.05}$	$20.8^{+3.9}_{-2.0}$	$0.71^{+0.05}_{-0.05}$	260	$10.9^{+0.3}_{-0.8}$
GW190727_060333	$68.8^{+10.2}_{-7.8}$	$29.4^{+4.6}_{-3.7}$	$38.9^{+8.9}_{-6.0}$	$30.2^{+6.5}_{-8.3}$	$0.09^{+0.25}_{-0.27}$	$3.07^{+1.30}_{-1.23}$	$0.52^{+0.18}_{-0.18}$	$65.4^{+9.5}_{-7.3}$	$0.73^{+0.09}_{-0.11}$	380	$11.7^{+0.2}_{-0.5}$
GW190728_064510	$20.7^{+4.2}_{-1.4}$	$8.6^{+0.6}_{-0.3}$	$12.5^{+6.9}_{-2.3}$	$8.0^{+1.7}_{-2.6}$	$0.13^{+0.19}_{-0.07}$	$0.88^{+0.26}_{-0.38}$	$0.18^{+0.05}_{-0.07}$	$19.7^{+4.4}_{-1.4}$	$0.71^{+0.04}_{-0.04}$	400	$13.1^{+0.3}_{-0.4}$
GW190731_140936	$70.7^{+16.3}_{-11.4}$	$29.7^{+7.4}_{-5.3}$	$41.8^{+12.7}_{-9.1}$	$29.0^{+10.2}_{-9.9}$	$0.07^{+0.28}_{-0.25}$	$3.33^{+2.35}_{-1.77}$	$0.56^{+0.31}_{-0.26}$	$67.4^{+15.3}_{-10.8}$	$0.71^{+0.12}_{-0.14}$	3600	$8.8^{+0.3}_{-0.4}$
GW190803_022701	$65.0^{+12.0}_{-8.1}$	$27.6^{+5.4}_{-3.8}$	$37.7^{+9.8}_{-6.7}$	$27.6^{+7.6}_{-8.5}$	$-0.01^{+0.23}_{-0.28}$	$3.19^{+1.63}_{-1.47}$	$0.54^{+0.22}_{-0.22}$	$62.1^{+11.2}_{-7.6}$	$0.68^{+0.09}_{-0.12}$	1000	$9.3^{+0.3}_{-0.5}$
GW190814	$25.9^{+1.3}_{-1.3}$	$6.11^{+0.06}_{-0.05}$	$23.3^{+1.4}_{-1.4}$	$2.6^{+0.1}_{-0.1}$	$0.00^{+0.07}_{-0.07}$	$0.23^{+0.04}_{-0.05}$	$0.05^{+0.01}_{-0.01}$	$25.7^{+1.3}_{-1.3}$	$0.28^{+0.03}_{-0.03}$	22	$25.3^{+0.1}_{-0.2}$
GW190828_063405	$57.2^{+7.9}_{-4.3}$	$24.6^{+3.6}_{-2.0}$	$31.9^{+5.4}_{-4.1}$	$25.8^{+4.9}_{-5.3}$	$0.15^{+0.15}_{-0.16}$	$2.07^{+0.65}_{-0.92}$	$0.38^{+0.10}_{-0.15}$	$54.3^{+7.3}_{-4.0}$	$0.74^{+0.07}_{-0.07}$	340	$16.5^{+0.2}_{-0.3}$
GW190828_065509	$34.3^{+5.2}_{-4.3}$	$13.4^{+1.4}_{-1.0}$	$23.7^{+6.8}_{-6.7}$	$10.4^{+3.8}_{-2.2}$	$0.05^{+0.16}_{-0.17}$	$1.54^{+0.69}_{-0.65}$	$0.29^{+0.11}_{-0.11}$	$33.0^{+5.3}_{-4.3}$	$0.64^{+0.08}_{-0.08}$	590	$10.2^{+0.4}_{-0.5}$
GW190910_112807	$78.0^{+9.3}_{-9.1}$	$33.5^{+4.2}_{-4.1}$	$43.8^{+7.6}_{-6.8}$	$34.2^{+6.6}_{-7.3}$	$0.00^{+0.17}_{-0.20}$	$1.52^{+1.09}_{-0.63}$	$0.29^{+0.17}_{-0.11}$	$74.4^{+8.5}_{-8.6}$	$0.69^{+0.07}_{-0.08}$	9600	$14.5^{+0.2}_{-0.3}$
GW190915_235702	$57.2^{+7.1}_{-5.3}$	$24.4^{+3.0}_{-2.3}$	$32.6^{+8.8}_{-4.9}$	$24.5^{+4.9}_{-5.8}$	$-0.03^{+0.19}_{-0.24}$	$1.75^{+0.71}_{-0.65}$	$0.32^{+0.11}_{-0.11}$	$54.7^{+6.6}_{-5.0}$	$0.69^{+0.08}_{-0.09}$	450	$13.1^{+0.2}_{-0.3}$
GW190924_021846	$13.9^{+2.8}_{-0.9}$	$5.8^{+0.2}_{-0.2}$	$8.8^{+4.3}_{-1.8}$	$5.1^{+1.2}_{-1.5}$	$0.03^{+0.20}_{-0.08}$	$0.55^{+0.22}_{-0.22}$	$0.11^{+0.04}_{-0.04}$	$13.3^{+3.0}_{-0.9}$	$0.67^{+0.05}_{-0.04}$	380	$12.0^{+0.3}_{-0.4}$
GW190929_012149	$93.3^{+23.3}_{-15.0}$	$35.6^{+10.2}_{-7.4}$	$66.3^{+21.6}_{-16.6}$	$26.8^{+14.7}_{-10.6}$	$-0.03^{+0.23}_{-0.28}$	$3.13^{+2.51}_{-1.37}$	$0.53^{+0.33}_{-0.20}$	$90.3^{+22.3}_{-14.6}$	$0.60^{+0.17}_{-0.22}$	1700	$9.7^{+0.4}_{-0.6}$
GW190930_133541	$21.2^{+5.9}_{-2.0}$	$8.5^{+0.5}_{-0.4}$	$14.2^{+8.0}_{-4.0}$	$6.9^{+2.4}_{-2.1}$	$0.19^{+0.22}_{-0.16}$	$0.77^{+0.32}_{-0.32}$	$0.16^{+0.06}_{-0.06}$	$20.2^{+6.1}_{-2.0}$	$0.71^{+0.07}_{-0.06}$	1600	$9.7^{+0.3}_{-0.5}$

one-dimensional marginal posterior distributions shown in Fig. 8. The two-dimensional projections on the M–q and $\mathcal{M}$–$\chi_{\rm eff}$ planes are shown as light-gray contours in Figs. 4 and 5 respectively. The full multidimensional posterior distributions are available as part of the public data release accompanying this paper [183], as detailed further in Sec. VII.

Similar to the results presented in Sec. A 1, the vast majority of the inferred source properties for these 36 binaries are consistent with those presented in GWTC-2 [8]. For a subset of binaries, their inferred masses have changed nominally with GW190706_222641 as of the GWTC-2.1 analysis preferring a higher total mass whereas both GW190521 and GW190929_012149 now are recovered as less massive than in GWTC-2. Additionally, GW190929_012149 as recovered in GWTC-2 had a comparatively broad and multimodal posterior distribution for its primary mass. The higher-mass mode is no longer present in the GWTC-2.1 analysis, which together with the secondary mass of GW190929_012149 remaining largely unchanged between the GWTC-2 and GWTC-2.1 analyses also leads to larger support for a more equal-mass binary. On the other hand, we now identify GW190707_093326, GW190708_232457 and GW190930_133541 more predominantly with an unequal q distribution as compared to the broad support, with stronger preference for equal masses, reported in GWTC-2. Finally, where in GWTC-2 GW190521 was identified with a unimodal q posterior distribution, GWTC-2.1 now also supports an additional subdominant mode at more unequal masses.

A more direct comparison between the source properties for the 36 events originally reported in GWTC-2 [8], with

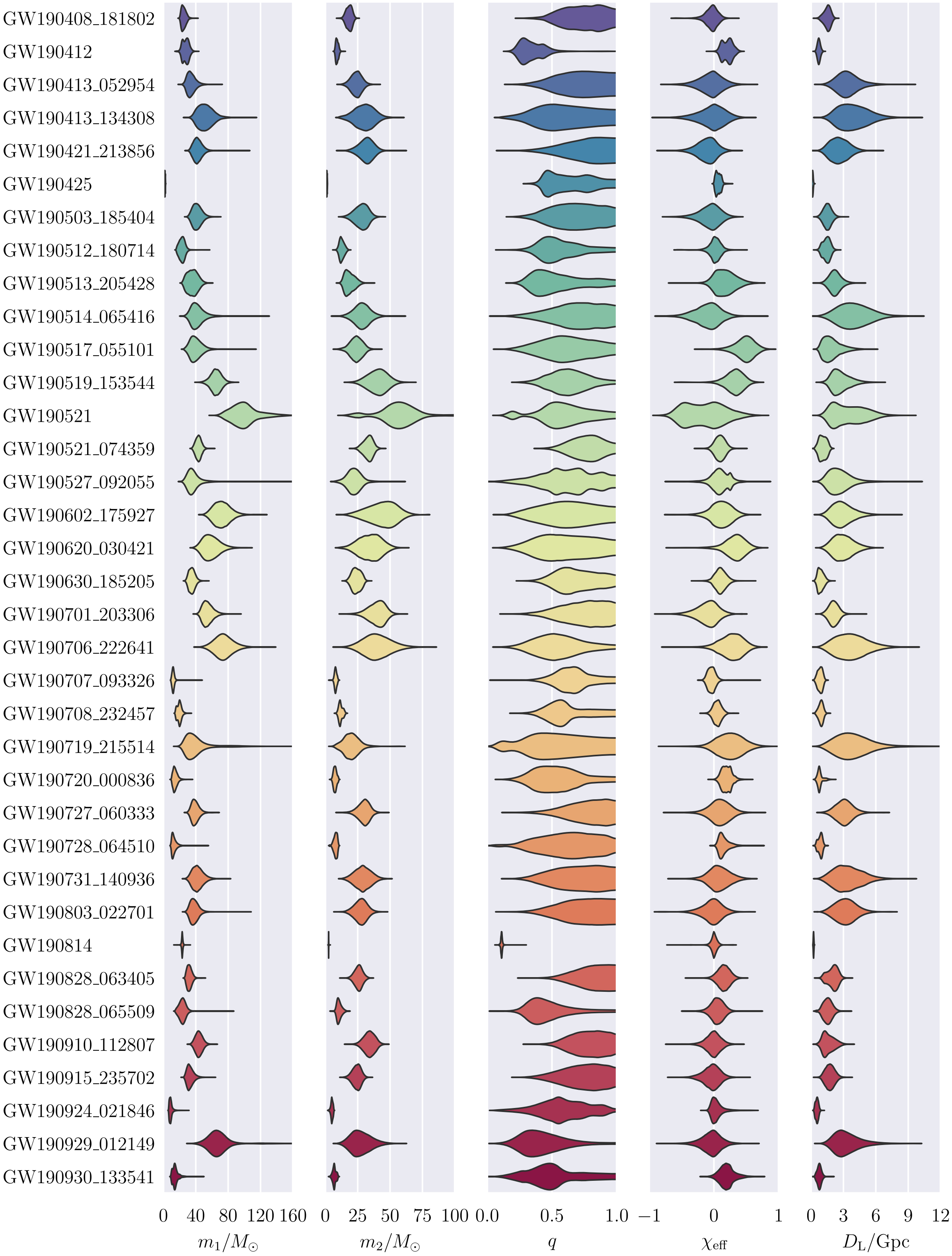

FIG. 8. Marginal posterior distributions on the primary mass m_1, secondary mass m_2, mass ratio q, effective inspiral spin $\chi_{\rm eff}$ and luminosity distance $D_{\rm L}$ for the 36 events from Table II that were not shown in Fig. 3. The vertical span for each region is constructed to be proportional to the one-dimensional marginal posterior at a given parameter value for the corresponding event. The posterior distributions are also represented numerically in terms of their one-dimensional median and 90% credible intervals in Table VIII.

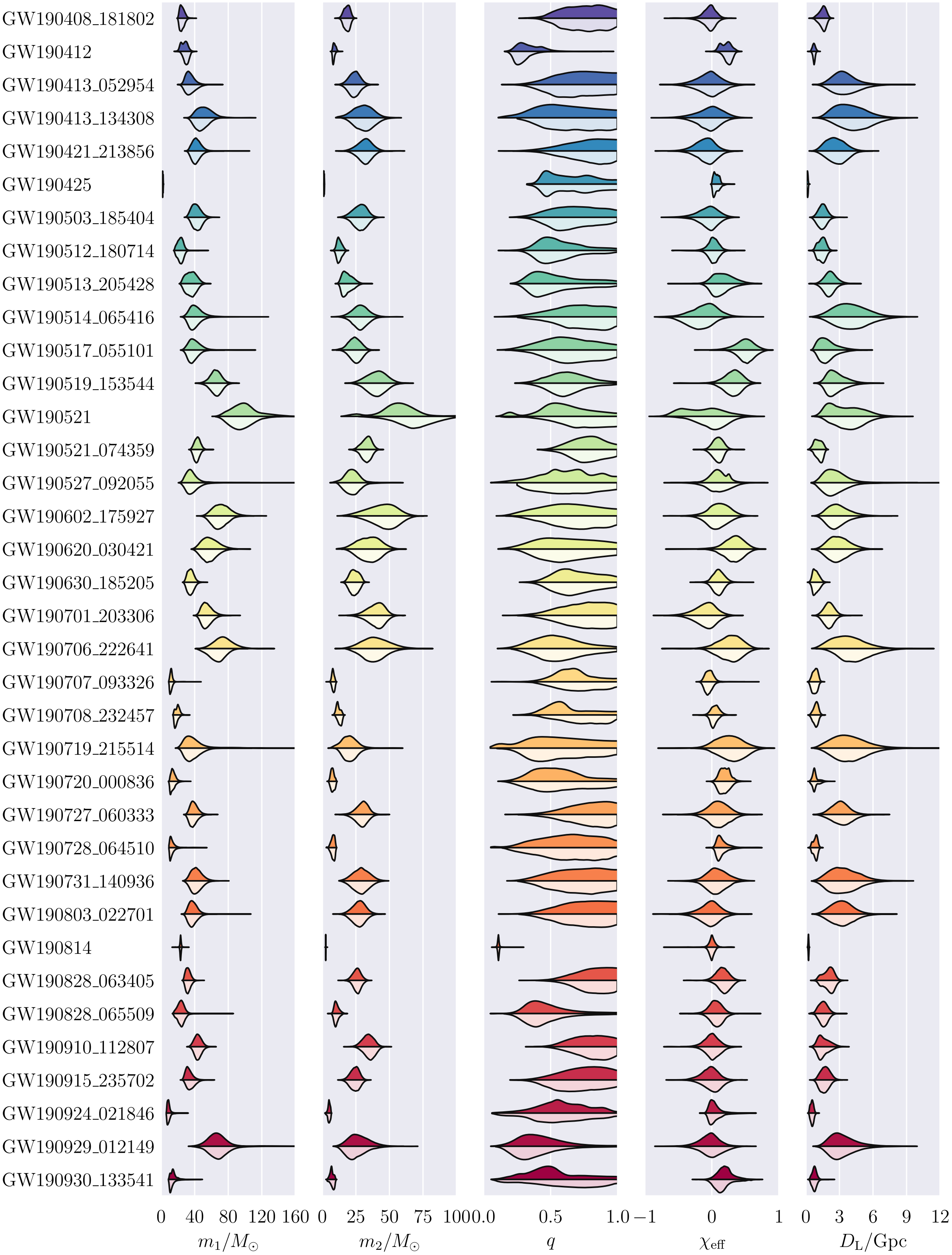

FIG. 9. Marginal posterior distributions of the primary mass m_1, secondary mass m_2, mass ratio q, effective inspiral spin $\chi_{\rm eff}$ and luminosity distance $D_{\rm L}$ for the 36 events from Table II that were not shown in Fig. 3. The top halves of each distribution match the results also presented in Fig. 8, with the bottom halves representing the analysis from the previous GWTC-2 [8,309]. The vertical span for each region is constructed to be proportional to the one-dimensional marginal posterior at a given parameter value for the corresponding event.

its associated public data release [309], and the analysis presented in this section is presented in Fig. 9. The main differences between the two sets of analyses were already presented in Sec. V, but where it is important to highlight the differing choices of waveform models used. As detailed in Sec. V A, the GWTC-2.1 analysis uses the same two models (IMRPhenomXPHM [57–60] and SEOBNRv4PHM [61–63]) for inferring the source properties of all BBHs whereas GWTC-2 makes use of a much broader set of models with significant variability between the analysis of specific events (the specific waveform model choices are laid out in Sec. V A and Table III of GWTC-2 [8]). These differences make the comparison presented in Fig. 9 more complicated than between two consistent sets of waveforms, but it nonetheless provides a measure for the evolution and improvement of the inference of the source properties of the observed events with the newer and more self-consistent analysis presented in GWTC-2.1 as the preferred results.

Independent results with the IMRPhenomXPHM model for many of these events were previously presented in 3-OGC [17]; other groups have also presented results with either the IMRPhenomXPHM, SEOBNRv4PHM or other precessing higher-mode models for, most prominently, the events GW190412 [310–313] and GW190521 [314–317]. While there is general agreement for the overall inferred source properties from many of these studies, there are significant differences present between them. These differences can however, as also explicitly stated in the studies themselves, be predominantly attributed to different prior assumptions or analysis configurations across the spread of the individual studies, in addition to the variance induced by waveform differences. This further highlights the need for the clear and public dissemination of both the exact analysis configurations used and the generated datasets containing the source properties inferred in order to encourage reproducibility and further model comparisons, especially as more events are added to the population of observed CBCs.

---

[1] J. Aasi *et al.* (LIGO Scientific Collaboration), Advanced LIGO, Classical Quantum Gravity **32**, 074001 (2015).

[2] F. Acernese *et al.* (Virgo Collaboration), Advanced Virgo: A second-generation interferometric gravitational wave detector, Classical Quantum Gravity **32**, 024001 (2015).

[3] B. P. Abbott *et al.* (LIGO Scientific Collaboration and Virgo Collaboration), Observation of Gravitational Waves from a Binary Black Hole Merger, Phys. Rev. Lett. **116**, 061102 (2016).

[4] B. P. Abbott *et al.* (LIGO Scientific Collaboration and Virgo Collaboration), Binary Black Hole Mergers in the first Advanced LIGO Observing Run, Phys. Rev. X **6**, 041015 (2016); **8**, 039903(E) (2018).

[5] B. P. Abbott *et al.* (LIGO Scientific Collaboration and Virgo Collaboration), GW170817: Observation of Gravitational Waves from a Binary Neutron Star Inspiral, Phys. Rev. Lett. **119**, 161101 (2017).

[6] B. P. Abbott *et al.* (LIGO Scientific Collaboration, Virgo Collaboration, Fermi GBM, INTEGRAL, IceCube, AstroSat Cadmium Zinc Telluride Imager Team, IPN, Insight-Hxmt, ANTARES, Swift, AGILE Team, 1M2H Team, Dark Energy Camera GW-EM, DES, DLT40, GRAWITA, Fermi-LAT, ATCA, ASKAP, Las Cumbres Observatory Group, OzGrav, DWF (Deeper Wider Faster Program), AST3, CAASTRO, VINROUGE, MASTER, J-GEM, GROWTH, JAGWAR, CaltechNRAO, TTU-NRAO, NuSTAR, Pan-STARRS, MAXI Team, TZAC Consortium, KU, Nordic Optical Telescope, ePESSTO, GROND, Texas Tech University, SALT Group, TOROS, BOOTES, MWA, CALET, IKI-GW Follow-up, H.E.S.S., LOFAR, LWA, HAWC, Pierre Auger, ALMA, Euro VLBI Team, Pi of Sky, Chandra Team at McGill University, DFN, ATLAS Telescopes, High Time Resolution Universe Survey, RIMAS, RATIR, and SKA South Africa/MeerKAT Collaborations), Multi-messenger observations of a binary neutron star merger, Astrophys. J. Lett. **848**, L12 (2017).

[7] B. P. Abbott *et al.* (LIGO Scientific Collaboration and Virgo Collaboration), GWTC-1: A Gravitational-Wave Transient Catalog of Compact Binary Mergers Observed by LIGO and Virgo during the First and Second Observing Runs, Phys. Rev. X **9**, 031040 (2019).

[8] R. Abbott *et al.* (LIGO Scientific and Virgo Collaborations), GWTC-2: Compact Binary Coalescences Observed by LIGO and Virgo During the First Half of the Third Observing Run, Phys. Rev. X **11**, 021053 (2021).

[9] Alexander H. Nitz, Collin Capano, Alex B. Nielsen, Steven Reyes, Rebecca White, Duncan A. Brown, and Badri Krishnan, 1-OGC: The first open gravitational-wave catalog of binary mergers from analysis of public Advanced LIGO data, Astrophys. J. **872**, 195 (2019).

[10] Ryan Magee *et al.*, Sub-threshold binary neutron star search in Advanced LIGO's first observing run, Astrophys. J. **878**, L17 (2019).

[11] Tejaswi Venumadhav, Barak Zackay, Javier Roulet, Liang Dai, and Matias Zaldarriaga, New search pipeline for compact binary mergers: Results for binary black holes in the first observing run of Advanced LIGO, Phys. Rev. D **100**, 023011 (2019).

[12] Barak Zackay, Tejaswi Venumadhav, Liang Dai, Javier Roulet, and Matias Zaldarriaga, Highly spinning and aligned binary black hole merger in the Advanced LIGO first observing run, Phys. Rev. D **100**, 023007 (2019).

[13] Tejaswi Venumadhav, Barak Zackay, Javier Roulet, Liang Dai, and Matias Zaldarriaga, New binary black hole

mergers in the second observing run of Advanced LIGO and Advanced Virgo, Phys. Rev. D **101**, 083030 (2020).

[14] Alexander H. Nitz, Thomas Dent, Gareth S. Davies, Sumit Kumar, Collin D. Capano, Ian Harry, Simone Mozzon, Laura Nuttall, Andrew Lundgren, and Márton Tápai, 2-OGC: Open gravitational-wave catalog of binary mergers from analysis of public Advanced LIGO and Virgo data, Astrophys. J. **891**, 123 (2019).

[15] Barak Zackay, Liang Dai, Tejaswi Venumadhav, Javier Roulet, and Matias Zaldarriaga, Detecting gravitational waves with disparate detector responses: Two new binary black hole mergers, Phys. Rev. D **104**, 063030 (2021).

[16] Alexander Harvey Nitz and Yi-Fan Wang, Search for Gravitational Waves from High-Mass-Ratio Compact-Binary Mergers of Stellar Mass and Subsolar Mass Black Holes, Phys. Rev. Lett. **126**, 021103 (2021).

[17] Alexander H. Nitz, Collin D. Capano, Sumit Kumar, Yi-Fan Wang, Shilpa Kastha, Marlin Schäfer, Rahul Dhurkunde, and Miriam Cabero, 3-OGC: Catalog of gravitational waves from compact-binary mergers, Astrophys. J. **922**, 76 (2021).

[18] Alexander H. Nitz and Yi-Fan Wang, Search for Gravitational Waves from the Coalescence of Subsolar-Mass Binaries in the First Half of Advanced LIGO and Virgo's Third Observing Run, Phys. Rev. Lett. **127**, 151101 (2021).

[19] Alexander H. Nitz, Sumit Kumar, Yi-Fan Wang, Shilpa Kastha, Shichao Wu, Marlin Schäfer, Rahul Dhurkunde, and Collin D. Capano, 4-OGC: Catalog of gravitational waves from compact-binary mergers, Astrophys. J. **946**, 59 (2023).

[20] Seth Olsen, Tejaswi Venumadhav, Jonathan Mushkin, Javier Roulet, Barak Zackay, and Matias Zaldarriaga, New binary black hole mergers in the LIGO-Virgo o3a data, Phys. Rev. D **106**, 043009 (2022).

[21] Alexander H. Nitz and Yi-Fan Wang, Broad search for gravitational waves from subsolar-mass binaries through LIGO and Virgo's third observing run, Phys. Rev. D **106**, 023024 (2022).

[22] M. W. E. Smith, D. B. Fox, D. F. Cowen, P. Mészáros, G. Tešić, J. Fixelle, I. Bartos, P. Sommers, Abhay Ashtekar, G. Jogesh Babu *et al.*, The astrophysical multimessenger observatory network (amon), Astropart. Phys. **45**, 56 (2013).

[23] E. Burns *et al.* (Fermi Gamma-ray Burst Monitor Team, LIGO Scientific, and Virgo Collaborations), A Fermi gamma-ray burst monitor search for electromagnetic signals coincident with gravitational-wave candidates in Advanced LIGO's first observing run, Astrophys. J. **871**, 90 (2019).

[24] LIGO Scientific Collaboration and Virgo Collaboration, Trigger data to accompany "GWTC-1: A gravitational-wave transient catalog of compact binary mergers observed by LIGO and Virgo during the first and second observing runs", Technical Report No. P1900392, LIGO DCC, 2020.

[25] Alexander H. Nitz, Alex B. Nielsen, and Collin D. Capano, Potential gravitational-wave and gamma-ray multi-messenger candidate from 2015 October 30, Astrophys. J. Lett. **876**, L4 (2019).

[26] Will M. Farr, Jonathan R. Gair, Ilya Mandel, and Curt Cutler, Counting and confusion: Bayesian rate estimation with multiple populations, Phys. Rev. D **91**, 023005 (2015).

[27] B. P. Abbott *et al.* (LIGO Scientific Collaboration and Virgo Collaboration), The rate of binary black hole mergers inferred from Advanced LIGO observations surrounding GW150914, Astrophys. J. Lett. **833**, L1 (2016).

[28] B. P. Abbott *et al.* (LIGO Scientific Collaboration and Virgo Collaboration), Supplement: The rate of binary black hole mergers inferred from Advanced LIGO observations surrounding GW150914, Astrophys. J. Suppl. Ser. **227**, 14 (2016).

[29] R. Abbott *et al.* (LIGO Scientific and Virgo Collaborations), Search for lensing signatures in the gravitational-wave observations from the first half of LIGO–Virgo's third observing run, Astrophys. J. **923**, 14 (2021).

[30] Alvin K. Y. Li, Rico K. L. Lo, Surabhi Sachdev, C. L. Chan, E. T. Lin, Tjonnie G. F. Li, and Alan J. Weinstein, Targeted subthreshold search for strongly lensed gravitational-wave events, Phys. Rev. D **107**, 123014 (2023).

[31] Connor McIsaac, David Keitel, Thomas Collett, Ian Harry, Simone Mozzon, Oliver Edy, and David Bacon, Search for strongly lensed counterpart images of binary black hole mergers in the first two LIGO observing runs, Phys. Rev. D **102**, 084031 (2020).

[32] S. E. Woosley, Pulsational pair-instability supernovae, Astrophys. J. **836**, 244 (2017).

[33] S. E. Woosley, The evolution of massive helium stars, including mass loss, Astrophys. J. **878**, 49 (2019).

[34] Simon Stevenson, Matthew Sampson, Jade Powell, Alejandro Vigna-Gómez, Coenraad J. Neijssel, Dorottya Szécsi, and Ilya Mandel, The impact of pair-instability mass loss on the binary black hole mass distribution, Astrophys. J. **882**, 121 (2019).

[35] R. Farmer, M. Renzo, S. E. de Mink, P. Marchant, and S. Justham, Mind the Gap: The location of the lower edge of the pair-instability supernova black hole mass gap, Astrophys. J. **887**, 53 (2019).

[36] R. Farmer, M. Renzo, S. E. de Mink, M. Fishbach, and S. Justham, Constraints from gravitational-wave detections of binary black hole mergers on the $^{12}\mathrm{C}(\alpha,\gamma)^{16}\mathrm{O}$ rate, Astrophys. J. **902**, L36 (2020).

[37] Michela Mapelli, Mario Spera, Enrico Montanari, Marco Limongi, Alessandro Chieffi, Nicola Giacobbo, Alessandro Bressan, and Yann Bouffanais, Impact of the rotation and compactness of progenitors on the mass of black holes, Astrophys. J. **888**, 76 (2020).

[38] Pablo Marchant and Takashi Moriya, The impact of stellar rotation on the black hole mass-gap from pair-instability supernovae, Astron. Astrophys. **640**, L18 (2020).

[39] Guglielmo Costa, Alessandro Bressan, Michela Mapelli, Paola Marigo, Giuliano Iorio, and Mario Spera, Formation of GW190521 from stellar evolution: The impact of the hydrogen-rich envelope, dredge-up, and $^{12}\mathrm{C}(\alpha,\gamma)^{16}\mathrm{O}$ rate on the pair-instability black hole mass gap, Mon. Not. R. Astron. Soc. **501**, 4514 (2021).

[40] Eoin Farrell, Jose H. Groh, Raphael Hirschi, Laura Murphy, Etienne Kaiser, Sylvia Ekström, Cyril Georgy, and Georges Meynet, Is GW190521 the merger of black holes from the first stellar generations?, Mon. Not. R. Astron. Soc. **502**, L40 (2021).

[41] R. Abbott *et al.* (LIGO Scientific and Virgo Collaborations), GW190814: Gravitational waves from the coalescence of a 23 solar mass black hole with a 2.6 solar mass compact object, Astrophys. J. Lett. **896**, L44 (2020).

[42] Gabriele Vajente, Yiwen Huang, Maximiliano Isi, Jenne C. Driggers, Jeffrey S. Kissel, Marek J. Szczepanczyk, and Salvatore Vitale, Machine-learning nonstationary noise out of gravitational-wave detectors, Phys. Rev. D **101**, 042003 (2020).

[43] Vaibhav Tiwari *et al.*, Regression of environmental noise in LIGO data, Classical Quantum Gravity **32**, 165014 (2015).

[44] LIGO Scientific Collaboration and Virgo Collaboration, The o3a data release, Gravitational Wave Open Science Center, 10.7935/nfnt-hm34 (2021).

[45] LIGO Scientific Collaboration and Virgo Collaboration, GWTC-2.1: Deep extended catalog of compact binary coalescences observed by LIGO and Virgo during the first half of the third observing run—data quality products for GW searches, Zenodo, 10.5281/zenodo.6477645 (2022).

[46] LIGO Scientific Collaboration and Virgo Collaboration, GWTC-2.1: Deep extended catalog of compact binary coalescences observed by LIGO and Virgo during the first half of the third observing run—Glitch modelling for events, Zenodo, 10.5281/zenodo.6477075 (2022).

[47] R. Abbott *et al.* (LIGO Scientific, Virgo, and KAGRA Collaborations), Open data from the third observing run of LIGO, Virgo, KAGRA and GEO, Astrophys. J. Suppl. Ser. **267**, 29 (2023).

[48] Surabhi Sachdev *et al.*, The GstLAL search analysis methods for compact binary mergers in Advanced LIGO's Second and Advanced Virgo's first observing runs, arXiv: 1901.08580.

[49] Chad Hanna *et al.*, Fast evaluation of multi-detector consistency for real-time gravitational wave searches, Phys. Rev. D **101**, 022003 (2020).

[50] Cody Messick *et al.*, Analysis framework for the prompt discovery of compact binary mergers in gravitational-wave data, Phys. Rev. D **95**, 042001 (2017).

[51] Bruce Allen, Warren G. Anderson, Patrick R. Brady, Duncan A. Brown, and Jolien D. E. Creighton, FINDCHIRP: An algorithm for detection of gravitational waves from inspiraling compact binaries, Phys. Rev. D **85**, 122006 (2012).

[52] Bruce Allen, χ^2 time-frequency discriminator for gravitational wave detection, Phys. Rev. D **71**, 062001 (2005).

[53] Tito Dal Canton *et al.*, Implementing a search for aligned-spin neutron star-black hole systems with advanced ground based gravitational wave detectors, Phys. Rev. D **90**, 082004 (2014).

[54] Samantha A. Usman *et al.*, The PyCBC search for gravitational waves from compact binary coalescence, Classical Quantum Gravity **33**, 215004 (2016).

[55] Alexander H. Nitz, Thomas Dent, Tito Dal Canton, Stephen Fairhurst, and Duncan A. Brown, Detecting binary compact-object mergers with gravitational waves: Understanding and Improving the sensitivity of the PyCBC search, Astrophys. J. **849**, 118 (2017).

[56] F. Aubin *et al.*, The MBTA pipeline for detecting compact binary coalescences in the third LIGO–Virgo observing run, Classical Quantum Gravity **38**, 095004 (2021).

[57] Geraint Pratten *et al.*, Computationally efficient models for the dominant and subdominant harmonic modes of precessing binary black holes, Phys. Rev. D **103**, 104056 (2021).

[58] Geraint Pratten, Sascha Husa, Cecilio Garcia-Quiros, Marta Colleoni, Antoni Ramos-Buades, Hector Estelles, and Rafel Jaume, Setting the cornerstone for a family of models for gravitational waves from compact binaries: The dominant harmonic for nonprecessing quasicircular black holes, Phys. Rev. D **102**, 064001 (2020).

[59] Cecilio García-Quirós, Marta Colleoni, Sascha Husa, Héctor Estellés, Geraint Pratten, Antoni Ramos-Buades, Maite Mateu-Lucena, and Rafel Jaume, Multimode frequency-domain model for the gravitational wave signal from nonprecessing black-hole binaries, Phys. Rev. D **102**, 064002 (2020).

[60] Cecilio García-Quirós, Sascha Husa, Maite Mateu-Lucena, and Angela Borchers, Accelerating the evaluation of inspiral–merger–ringdown waveforms with adapted grids, Classical Quantum Gravity **38**, 015006 (2021).

[61] Serguei Ossokine *et al.*, Multipolar effective-one-body waveforms for precessing binary black holes: Construction and validation, Phys. Rev. D **102**, 044055 (2020).

[62] Stanislav Babak, Andrea Taracchini, and Alessandra Buonanno, Validating the effective-one-body model of spinning, precessing binary black holes against numerical relativity, Phys. Rev. D **95**, 024010 (2017).

[63] Yi Pan, Alessandra Buonanno, Andrea Taracchini, Lawrence E. Kidder, Abdul H. Mroué, Harald P. Pfeiffer, Mark A. Scheel, and Béla Szilágyi, Inspiral-merger-ringdown waveforms of spinning, precessing black-hole binaries in the effective-one-body formalism, Phys. Rev. D **89**, 084006 (2014).

[64] Roberto Cotesta, Alessandra Buonanno, Alejandro Bohé, Andrea Taracchini, Ian Hinder, and Serguei Ossokine, Enriching the Symphony of gravitational waves from binary black holes by tuning higher harmonics, Phys. Rev. D **98**, 084028 (2018).

[65] Tim Dietrich, Sebastiano Bernuzzi, and Wolfgang Tichy, Closed-form tidal approximants for binary neutron star gravitational waveforms constructed from high-resolution numerical relativity simulations, Phys. Rev. D **96**, 121501 (2017).

[66] Tim Dietrich *et al.*, Matter imprints in waveform models for neutron star binaries: Tidal and self-spin effects, Phys. Rev. D **99**, 024029 (2019).

[67] R. Abbott *et al.* (LIGO Scientific, Virgo, and KAGRA Collaborations), GWTC-3: Compact binary coalescences observed by LIGO and Virgo during the second part of the third observing run, Phys. Rev. X **13**, 041039 (2023).

[68] B. P. Abbott *et al.* (KAGRA, LIGO Scientific, and Virgo Collaborations), Prospects for observing and localizing gravitational-wave transients with Advanced LIGO, Advanced Virgo and KAGRA, Living Rev. Relativity **23**, 3 (2020).

[69] Aaron Buikema *et al.* (aLIGO Collaboration), Sensitivity and performance of the Advanced LIGO detectors in the third observing run, Phys. Rev. D **102**, 062003 (2020).

[70] S. Biscans, S. Gras, C. D. Blair, J. Driggers, M. Evans, P. Fritschel, T. Hardwick, and G. Mansell, Suppressing parametric instabilities in LIGO using low-noise acoustic mode dampers, Phys. Rev. D **100**, 122003 (2019).

[71] M. Tse *et al.*, Quantum-Enhanced Advanced LIGO Detectors in the Era of Gravitational-Wave Astronomy, Phys. Rev. Lett. **123**, 231107 (2019).

[72] S. Soni *et al.* (LIGO Collaboration), Reducing scattered light in LIGO's third observing run, Classical Quantum Gravity **38**, 025016 (2020).

[73] Hsin-Yu Chen, Daniel E. Holz, John Miller, Matthew Evans, Salvatore Vitale, and Jolien Creighton, Distance measures in gravitational-wave astrophysics and cosmology, Classical Quantum Gravity **38**, 055010 (2021).

[74] D. Aisa *et al.*, The Advanced Virgo monolithic fused silica suspension, Nucl. Instrum. Methods Phys. Res., Sect. A **824**, 644 (2016).

[75] F. Acernese *et al.* (Virgo Collaboration), Increasing the Astrophysical Reach of the Advanced Virgo Detector via the Application of Squeezed Vacuum States of Light, Phys. Rev. Lett. **123**, 231108 (2019).

[76] M. Blom, M. G. Beker, A. Bertolini, J. F. J. van den Brand, H. J. Bulten, M. Doets, E. Hennes, F. A. Mul, D. S. Rabeling, and A. Schimmel, Vertical and horizontal seismic isolation performance of the Advanced Virgo external injection bench seismic attenuation system, Phys. Procedia **61**, 641 (2015).

[77] Ling Sun *et al.*, Characterization of systematic error in Advanced LIGO calibration, Classical Quantum Gravity **37**, 225008 (2020).

[78] F. Acernese *et al.* (Virgo Collaboration), Calibration of Advanced Virgo and reconstruction of detector strain $h(t)$ during the observing run O3, Classical Quantum Gravity **39**, 045006 (2022).

[79] D. Estevez, P. Lagabbe, A. Masserot, L. Rolland, M. Seglar-Arroyo, and D. Verkindt, The Advanced Virgo photon calibrators, Classical Quantum Gravity **38**, 075007 (2021).

[80] D. Davis, T. J. Massinger, A. P. Lundgren, J. C. Driggers, A. L. Urban, and L. K. Nuttall, Improving the sensitivity of Advanced LIGO using noise subtraction, Classical Quantum Gravity **36**, 055011 (2019).

[81] A. Viets and M. Wade, Subtracting narrow-band noise from LIGO strain data in the third observing run (2021), https://dcc.ligo.org/LIGO-T2100058/public.

[82] D. Estevez, B. Mours, L. Rolland, and D.Verkindt, Online h(t) reconstruction for Virgo O3 data: Start of O3, Technical Report No. VIR-0652B-19, Virgo, 2019.

[83] L. Rolland, M. Seglar-Arroyo, and D. Verkindt, Reprocessing of h(t) for the last two weeks of O3a, Technical Report No. VIR-1201A-19, Virgo, 2019.

[84] Ethan Payne, Colm Talbot, Paul D. Lasky, Eric Thrane, and Jeffrey S. Kissel, Gravitational-wave astronomy with a physical calibration model, Phys. Rev. D **102**, 122004 (2020).

[85] Salvatore Vitale, Carl-Johan Haster, Ling Sun, Ben Farr, Evan Goetz, Jeff Kissel, and Craig Cahillane, Physical approach to the marginalization of LIGO calibration uncertainties, Phys. Rev. D **103**, 063016 (2021).

[86] D. Davis *et al.* (LIGO Instrument Science Collaboration), LIGO detector characterization in the second and third observing runs, Classical Quantum Gravity **38**, 135014 (2021).

[87] F. Acernese *et al.*, Virgo detector characterization and data quality: Results from the O3 run, Classical Quantum Gravity **40**, 185006 (2023).

[88] Duncan Macleod, Alex L. Urban, Maximiliano Isi, Thomas Massinger, Matt Pitkin, paulaltin, Alex Nitz, and Evan Goetz, gwpy/gwsumm: 2.1.0, 10.5281/zenodo.4975045 (2021).

[89] G. Hemming and D. Verkindt, Virgo interferometer monitor (VIM) web user interface (WUI) user guide, Technical Report No. VIR-0546A-16, Virgo, 2016.

[90] B. P. Abbott *et al.* (LIGO Scientific Collaboration and Virgo Collaboration), Characterization of transient noise in Advanced LIGO relevant to gravitational wave signal GW150914, Classical Quantum Gravity **33**, 134001 (2016).

[91] L. K. Nuttall, Characterizing transient noise in the LIGO detectors, Phil. Trans. R. Soc. A **376**, 20170286 (2018).

[92] S. Soni *et al.*, Discovering features in gravitational-wave data through detector characterization, citizen science and machine learning, Classical Quantum Gravity **38**, 195016 (2021).

[93] Neil J. Cornish and Tyson B. Littenberg, Bayeswave: Bayesian inference for gravitational wave bursts and instrument glitches, Classical Quantum Gravity **32**, 135012 (2015).

[94] Bence Bécsy, Peter Raffai, Neil J. Cornish, Reed Essick, Jonah Kanner, Erik Katsavounidis, Tyson B. Littenberg, Margaret Millhouse, and Salvatore Vitale, Parameter estimation for gravitational-wave bursts with the BayesWave pipeline, Astrophys. J. **839**, 15 (2017).

[95] Chris Pankow *et al.*, Mitigation of the instrumental noise transient in gravitational-wave data surrounding GW170817, Phys. Rev. D **98**, 084016 (2018).

[96] Neil J. Cornish, Tyson B. Littenberg, Bence Bécsy, Katerina Chatziioannou, James A. Clark, Sudarshan Ghonge, and Margaret Millhouse, BayesWave analysis pipeline in the era of gravitational wave observations, Phys. Rev. D **103**, 044006 (2021).

[97] S. Klimenko and Guenakh Mitselmakher, A wavelet method for detection of gravitational wave bursts, Classical Quantum Gravity **21**, S1819 (2004).

[98] S. Klimenko, S. Mohanty, Malik Rakhmanov, and Guenakh Mitselmakher, Constraint likelihood analysis for a network of gravitational wave detectors, Phys. Rev. D **72**, 122002 (2005).

[99] S. Klimenko, S. Mohanty, Malik Rakhmanov, and Guenakh Mitselmakher, Constraint likelihood method: Generalization for colored noise, J. Phys. Conf. Ser. **32**, 12 (2006).

[100] S. Klimenko, G. Vedovato, M. Drago, G. Mazzolo, G. Mitselmakher, C. Pankow, G. Prodi, V. Re, F. Salemi, and I. Yakushin, Localization of gravitational wave sources with networks of advanced detectors, Phys. Rev. D **83**, 102001 (2011).

[101] S. Klimenko *et al.*, Method for detection and reconstruction of gravitational wave transients with networks of advanced detectors, Phys. Rev. D **93**, 042004 (2016).

[102] Gareth S. Davies, Thomas Dent, Márton Tápai, Ian Harry, Connor McIsaac, and Alexander H. Nitz, Extending the PyCBC search for gravitational waves from compact binary mergers to a global network, Phys. Rev. D **102,** 022004 (2020).

[103] Qi Chu, Low-latency detection and localization of gravitational waves from compact binary coalescences, Ph.D. thesis, The University of Western Australia, 2017.

[104] LIGO Scientific Collaboration and Virgo Collaboration, GWTC-2.1: Deep extended catalog of compact binary coalescences observed by LIGO and Virgo during the first half of the third observing run—candidate data release, Zenodo, 10.5281/zenodo.5117761 (2022).

[105] Benjamin J. Owen and B. S. Sathyaprakash, Matched filtering of gravitational waves from inspiraling compact binaries: Computational cost and template placement, Phys. Rev. D **60**, 022002 (1999).

[106] Ian W. Harry, Bruce Allen, and B. S. Sathyaprakash, A stochastic template placement algorithm for gravitational wave data analysis, Phys. Rev. D **80**, 104014 (2009).

[107] Stephen Privitera, Satyanarayan R. P. Mohapatra, Parameswaran Ajith, Kipp Cannon, Nickolas Fotopoulos, Melissa A. Frei, Chad Hanna, Alan J. Weinstein, and John T. Whelan, Improving the sensitivity of a search for coalescing binary black holes with nonprecessing spins in gravitational wave data, Phys. Rev. D **89**, 024003 (2014).

[108] Luc Blanchet, Thibault Damour, Bala R. Iyer, Clifford M. Will, and Alan G. Wiseman, Gravitational Radiation Damping of Compact Binary Systems to Second Post-Newtonian Order, Phys. Rev. Lett. **74**, 3515 (1995).

[109] P. Ajith *et al.*, Inspiral-Merger-Ringdown Waveforms for Black-Hole Binaries with Non-Precessing Spins, Phys. Rev. Lett. **106**, 241101 (2011).

[110] T. Dent and J. Veitch, Optimizing gravitational-wave searches for a population of coalescing binaries: Intrinsic parameters, Phys. Rev. D **89**, 062002 (2014).

[111] Heather Kin Yee Fong, From simulations to signals: Analyzing gravitational waves from compact binary coalescences, Ph.D. thesis, Toronto University, 2018.

[112] Reed Essick, Patrick Godwin, Chad Hanna, Lindy Blackburn, and Erik Katsavounidis, iDQ: Statistical inference of non-gaussian noise with auxiliary degrees of freedom in gravitational-wave detectors, Mach. Learn. **2**, 015004 (2020).

[113] Patrick Godwin *et al.*, Incorporation of statistical data quality information into the GstLAL search analysis, arXiv:2010.15282.

[114] Shasvath J. Kapadia *et al.*, A self-consistent method to estimate the rate of compact binary coalescences with a Poisson mixture model, Classical Quantum Gravity **37**, 045007 (2020).

[115] Vaibhav Tiwari, Estimation of the sensitive volume for gravitational-wave source populations using weighted Monte Carlo integration, Classical Quantum Gravity **35**, 145009 (2018).

[116] LIGO Scientific Collaboration, Virgo Collaboration, and KAGRA Collaboration, "O3 Public Alerts," GraceDB, https://gracedb.ligo.org/superevents/public/O3/.

[117] Alessandra Buonanno, Yan-bei Chen, and Michele Vallisneri, Detecting gravitational waves from precessing binaries of spinning compact objects: Adiabatic limit, Phys. Rev. D **67**, 104025 (2003); **74**, 029904(E) (2006).

[118] Alessandra Buonanno, Yanbei Chen, Yi Pan, and Michele Vallisneri, Erratum: Quasiphysical family of gravity-wave templates for precessing binaries of spinning compact objects: Application to double-spin precessing binaries [Phys. Rev. D **70**, 104003 (2004)], **74**, 029902(E) (2006).

[119] Alessandra Buonanno, Bala Iyer, Evan Ochsner, Yi Pan, and B. S. Sathyaprakash, Comparison of post-Newtonian templates for compact binary inspiral signals in gravitational-wave detectors, Phys. Rev. D **80**, 084043 (2009).

[120] Alejandro Bohé *et al.*, Improved effective-one-body model of spinning, nonprecessing binary black holes for the era of gravitational-wave astrophysics with advanced detectors, Phys. Rev. D **95**, 044028 (2017).

[121] Nicolas Andres *et al.*, Assessing the compact-binary merger candidates reported by the MBTA pipeline in the LIGO–Virgo O3 run: Probability of astrophysical origin, classification, and associated uncertainties, Classical Quantum Gravity **39**, 055002 (2022).

[122] R. Abbott *et al.* (LIGO Scientific and Virgo Collaborations), Population properties of compact objects from the second LIGO-Virgo gravitational-wave transient catalog, Astrophys. J. Lett. **913**, L7 (2021).

[123] Benjamin P. Abbott *et al.* (LIGO Scientific Collaboration and Virgo Collaboration), All-sky search for short gravitational-wave bursts in the first Advanced LIGO run, Phys. Rev. D **95**, 042003 (2017).

[124] Alex Nitz *et al.*, gwastro/pycbc: PyCBC Release v1.16.13, (2020).

[125] Tito Dal Canton, Alexander H. Nitz, Bhooshan Gadre, Gareth S. Cabourn Davies, Veronica Villa-Ortega, Thomas Dent, Ian Harry, and Liting Xiao, Real-time search for compact binary mergers in Advanced LIGO and Virgo's third observing run using PyCBC live, Astrophys. J. **923**, 254 (2021).

[126] Soumen Roy, Anand S. Sengupta, and Nilay Thakor, Hybrid geometric-random template-placement algorithm for gravitational wave searches from compact binary coalescences, Phys. Rev. D **95**, 104045 (2017).

[127] Soumen Roy, Anand S. Sengupta, and Parameswaran Ajith, Effectual template banks for upcoming compact binary searches in Advanced-LIGO and Virgo data, Phys. Rev. D **99**, 024048 (2019).

[128] Alexander Harvey Nitz, Distinguishing short duration noise transients in LIGO data to improve the PyCBC search for gravitational waves from high mass binary black hole mergers, Classical Quantum Gravity **35**, 035016 (2018).

[129] Collin Capano, Thomas Dent, Chad Hanna, Martin Hendry, Yi-Ming Hu, Chris Messenger, and John Veitch, Systematic errors in estimation of gravitational-wave candidate significance, Phys. Rev. D **96**, 082002 (2017).

[130] Thomas Dent, Technical note: Extending the PyCBC pastro calculation to a global network, Technical Report No. T2100060, LIGO DCC, 2021, https://dcc.ligo.org/LIGO-T2100060/public.

[131] LIGO Scientific Collaboration and Virgo Collaboration, GWTC-2.1: Deep extended-catalog of compact binary coalescences observed by LIGO and Virgo during the first half of the third observing run—sensitivity of search pipelines to simulated signals, Zenodo, 10.5281/zenodo.5117798 (2021).

[132] LIGO Scientific Collaboration and Virgo Collaboration, GWTC-2 data release: Sensitivity of matched filter searches to binary black hole merger populations, LIGO DCC Technical Report No. P2000217, 2020.

[133] Colm Talbot, Rory Smith, Eric Thrane, and Gregory B. Poole, Parallelized inference for gravitational-wave astronomy, Phys. Rev. D **100**, 043030 (2019).

[134] R. Abbott *et al.* (LIGO Scientific, KAGRA, and VIRGO Collaborations), Observation of gravitational waves from two neutron star–black hole coalescences, Astrophys. J. Lett. **915**, L5 (2021).

[135] B. P. Abbott *et al.* (LIGO Scientific Collaboration and Virgo Collaboration), GW190425: Observation of a compact binary coalescence with total mass $\sim 3.4 M_{\odot}$, Astrophys. J. Lett. **892**, L3 (2020).

[136] Benjamin P. Abbott *et al.* (LIGO Scientific and Virgo Collaboration), A guide to LIGO–Virgo detector noise and extraction of transient gravitational-wave signals, Classical Quantum Gravity **37**, 055002 (2020).

[137] Christopher P. L. Berry *et al.*, Parameter estimation for binary neutron-star coalescences with realistic noise during the Advanced LIGO era, Astrophys. J. **804**, 114 (2015).

[138] Curt Cutler and Eanna E. Flanagan, Gravitational waves from merging compact binaries: How accurately can one extract the binary's parameters from the inspiral wave form?, Phys. Rev. D **49**, 2658 (1994).

[139] J. Veitch *et al.*, Parameter estimation for compact binaries with ground-based gravitational-wave observations using the lalinference software library, Phys. Rev. D **91**, 042003 (2015).

[140] B. P. Abbott *et al.* (LIGO Scientific Collaboration and Virgo Collaboration), Properties of the Binary Black Hole Merger GW150914, Phys. Rev. Lett. **116**, 241102 (2016).

[141] Lee S. Finn, Detection, measurement and gravitational radiation, Phys. Rev. D **46**, 5236 (1992).

[142] I. M. Romero-Shaw *et al.*, Bayesian inference for compact binary coalescences with bilby: Validation and application to the first LIGO–Virgo gravitational-wave transient catalogue, Mon. Not. R. Astron. Soc. **499**, 3295 (2020).

[143] Tyson B. Littenberg and Neil J. Cornish, Bayesian inference for spectral estimation of gravitational wave detector noise, Phys. Rev. D **91**, 084034 (2015).

[144] Katerina Chatziioannou, Carl-Johan Haster, Tyson B. Littenberg, Will M. Farr, Sudarshan Ghonge, Margaret Millhouse, James A. Clark, and Neil Cornish, Noise spectral estimation methods and their impact on gravitational wave measurement of compact binary mergers, Phys. Rev. D **100**, 104004 (2019).

[145] Sylvia Biscoveanu, Carl-Johan Haster, Salvatore Vitale, and Jonathan Davies, Quantifying the effect of power spectral density uncertainty on gravitational-wave parameter estimation for compact binary sources, Phys. Rev. D **102**, 023008 (2020).

[146] Benjamin P. Abbott *et al.* (LIGO Scientific Collaboration and Virgo Collaboration), GW170104: Observation of a 50-Solar-Mass Binary Black Hole Coalescence at Redshift 0.2, Phys. Rev. Lett. **118**, 221101 (2017); **121**, 129901(E) (2018).

[147] Fabian Hofmann, Enrico Barausse, and Luciano Rezzolla, The final spin from binary black holes in quasi-circular orbits, Astrophys. J. Lett. **825**, L19 (2016).

[148] Xisco Jiménez-Forteza, David Keitel, Sascha Husa, Mark Hannam, Sebastian Khan, and Michael Pürrer, Hierarchical data-driven approach to fitting numerical relativity data for nonprecessing binary black holes with an application to final spin and radiated energy, Phys. Rev. D **95**, 064024 (2017).

[149] James Healy and Carlos O. Lousto, Remnant of binary black-hole mergers: New simulations and peak luminosity studies, Phys. Rev. D **95**, 024037 (2017).

[150] Nathan K. Johnson-McDaniel, Anuradha Gupta, P. Ajith, David Keitel, Ofek Birnholtz, Frank Ohme, and Sascha Husa, Determining the final spin of a binary black hole system including in-plane spins: Method and checks of accuracy, Technical Report No. T1600168, LIGO DCC, 2016.

[151] David Keitel *et al.*, The most powerful astrophysical events: Gravitational-wave peak luminosity of binary black holes as predicted by numerical relativity, Phys. Rev. D **96**, 024006 (2017).

[152] Kent Yagi and Nicolás Yunes, Approximate universal relations for neutron stars and quark stars, Phys. Rep. **681**, 1 (2017).

[153] Mark Hannam, Patricia Schmidt, Alejandro Bohé, Leïla Haegel, Sascha Husa, Frank Ohme, Geraint Pratten, and Michael Pürrer, Simple Model of Complete Precessing Black-Hole-Binary Gravitational Waveforms, Phys. Rev. Lett. **113**, 151101 (2014).

[154] Alejandro Bohé, Mark Hannam, Sascha Husa, Frank Ohme, Pürrer Michael, and Patricia Schmidt, PhenomPv2—technical notes for the LAL implementation, Technical Report No. T1500602, LIGO DCC, 2016.

[155] Sebastian Khan, Katerina Chatziioannou, Mark Hannam, and Frank Ohme, Phenomenological model for the gravitational-wave signal from precessing binary black holes with two-spin effects, Phys. Rev. D **100**, 024059 (2019).

[156] Sebastian Khan, Frank Ohme, Katerina Chatziioannou, and Mark Hannam, Including higher order multipoles in gravitational-wave models for precessing binary black holes, Phys. Rev. D **101**, 024056 (2020).

[157] Antoni Ramos-Buades, Patricia Schmidt, Geraint Pratten, and Sascha Husa, Validity of common modeling approximations for precessing binary black holes with higher-order modes, Phys. Rev. D **101**, 103014 (2020).

[158] Katerina Chatziioannou, Antoine Klein, Nicolás Yunes, and Neil Cornish, Constructing gravitational waves from generic spin-precessing compact binary inspirals, Phys. Rev. D **95**, 104004 (2017).

[159] Francois Foucart, Luisa Buchman, Matthew D. Duez, Michael Grudich, Lawrence E. Kidder, Ilana MacDonald, Abdul Mroue, Harald P. Pfeiffer, Mark A. Scheel, and Bela Szilagyi, First direct comparison of

nondisrupting neutron star-black hole and binary black hole merger simulations, Phys. Rev. D **88**, 064017 (2013).

[160] Prayush Kumar, Michael Pürrer, and Harald P. Pfeiffer, Measuring neutron star tidal deformability with Advanced LIGO: A Bayesian analysis of neutron star—black hole binary observations, Phys. Rev. D **95**, 044039 (2017).

[161] Yiwen Huang, Carl-Johan Haster, Salvatore Vitale, Vijay Varma, Francois Foucart, and Sylvia Biscoveanu, Statistical and systematic uncertainties in extracting the source properties of neutron star—black hole binaries with gravitational waves, Phys. Rev. D **103**, 083001 (2021).

[162] Sascha Husa, Sebastian Khan, Mark Hannam, Michael Pürrer, Frank Ohme, Xisco Jiménez Forteza, and Alejandro Bohé, Frequency-domain gravitational waves from non-precessing black-hole binaries. I. New numerical waveforms and anatomy of the signal, Phys. Rev. D **93**, 044006 (2016).

[163] Sebastian Khan, Sascha Husa, Mark Hannam, Frank Ohme, Michael Pürrer, Xisco Jiménez Forteza, and Alejandro Bohé, Frequency-domain gravitational waves from non-precessing black-hole binaries. II. A phenomenological model for the advanced detector era, Phys. Rev. D **93**, 044007 (2016).

[164] Rory Smith, Scott E. Field, Kent Blackburn, Carl-Johan Haster, Michael Pürrer, Vivien Raymond, and Patricia Schmidt, Fast and accurate inference on gravitational waves from precessing compact binaries, Phys. Rev. D **94**, 044031 (2016).

[165] Amanda Baylor, Rory Smith, and Eve Chase, Imrphenompv2_nrtidal_gw190425_narrow_mc (2019).

[166] Gregory Ashton *et al.*, BILBY: A user-friendly Bayesian inference library for gravitational-wave astronomy, Astrophys. J. Suppl. Ser. **241**, 27 (2019).

[167] John Skilling, Nested sampling for general Bayesian computation, Bayesian Anal. **1**, 833 (2006).

[168] Joshua S. Speagle, DYNESTY: A dynamic nested sampling package for estimating Bayesian posteriors and evidences, Mon. Not. R. Astron. Soc. **493**, 3132 (2020).

[169] Christian Rover, Renate Meyer, and Nelson Christensen, Bayesian inference on compact binary inspiral gravitational radiation signals in interferometric data, Classical Quantum Gravity **23**, 4895 (2006).

[170] Marc van der Sluys, Vivien Raymond, Ilya Mandel, Christian Rover, Nelson Christensen, Vicky Kalogera, Renate Meyer, and Alberto Vecchio, Parameter estimation of spinning binary inspirals using Markov-chain Monte Carlo, Classical Quantum Gravity **25**, 184011 (2008).

[171] LIGO Scientific Collaboration, LIGO Algorithm Library, 10.7935/GT1W-FZ16 (2018).

[172] C. Pankow, P. Brady, E. Ochsner, and R. O'Shaughnessy, Novel scheme for rapid parallel parameter estimation of gravitational waves from compact binary coalescences, Phys. Rev. D **92**, 023002 (2015).

[173] J. Lange *et al.*, Parameter estimation method that directly compares gravitational wave observations to numerical relativity, Phys. Rev. D **96**, 104041 (2017).

[174] D. Wysocki, R. O'Shaughnessy, Jacob Lange, and Yao-Lung L. Fang, Accelerating parameter inference with graphics processing units, Phys. Rev. D **99**, 084026 (2019).

[175] J. Wofford *et al.*, Improving performance for gravitational-wave parameter inference with an efficient and highly-parallelized algorithm, Phys. Rev. D **107**, 024040 (2023).

[176] Daniel Williams, Duncan Macleod, Avi Vajpeyi, and James Clark, transientlunatic/asimov: v0.3.2, 10.5281/zenodo.5142601 (2021).

[177] Charlie Hoy and Vivien Raymond, PESummary: The code agnostic parameter estimation summary page builder, SoftwareX **15**, 100765 (2021).

[178] Charlie Hoy and Vivien Raymond, pesummary, 10.5281/zenodo.3937806 (2020).

[179] P. A. R. Ade *et al.* (Planck Collaboration), Planck 2015 results. XIII. Cosmological parameters, Astron. Astrophys. **594**, A13 (2016).

[180] Craig Cahillane *et al.* (LIGO Scientific Collaboration), Calibration uncertainty for Advanced LIGO's first and second observing runs, Phys. Rev. D **96**, 102001 (2017).

[181] W. Farr, B. Farr, and T. Littenberg, Modelling calibration errors In CBC waveforms, (2014), https://dcc.ligo.org/LIGO-T1400682/public.

[182] Ethan Payne, Colm Talbot, Paul D. Lasky, Eric Thrane, and Jeffrey S. Kissel, Gravitational-wave astronomy with a physical calibration model, Phys. Rev. D **102**, 122004 (2020).

[183] LIGO Scientific Collaboration and Virgo Collaboration, GWTC-2.1: Deep extended catalog of compact binary coalescences observed by LIGO and Virgo during the first half of the third observing run—parameter estimation data release, Zenodo, 10.5281/zenodo.5117702 (2022).

[184] Michael Pürrer, Mark Hannam, and Frank Ohme, Can we measure individual black-hole spins from gravitational-wave observations?, Phys. Rev. D **93**, 084042 (2016).

[185] Salvatore Vitale, Ryan Lynch, Vivien Raymond, Riccardo Sturani, John Veitch, and Philp Graff, Parameter estimation for heavy binary-black holes with networks of second-generation gravitational-wave detectors, Phys. Rev. D **95**, 064053 (2017).

[186] Ken K. Y. Ng, Salvatore Vitale, Aaron Zimmerman, Katerina Chatziioannou, Davide Gerosa, and Carl-Johan Haster, Gravitational-wave astrophysics with effective-spin measurements: asymmetries and selection biases, Phys. Rev. D **98**, 083007 (2018).

[187] Luc Blanchet, Gravitational radiation from post-Newtonian sources and inspiralling compact binaries, Living Rev. Relativity **17**, 2 (2014).

[188] Etienne Racine, Analysis of spin precession in binary black hole systems including quadrupole-monopole interaction, Phys. Rev. D **78**, 044021 (2008).

[189] Michael Kesden, Davide Gerosa, Richard O'Shaughnessy, Emanuele Berti, and Ulrich Sperhake, Effective Potentials and Morphological Transitions for Binary Black-Hole Spin Precession, Phys. Rev. Lett. **114**, 081103 (2015).

[190] Davide Gerosa, Michael Kesden, Ulrich Sperhake, Emanuele Berti, and Richard O'Shaughnessy, Multi-timescale analysis of phase transitions in precessing black-hole binaries, Phys. Rev. D **92**, 064016 (2015).

[191] Nathan K. Johnson-McDaniel, Sumeet Kulkarni, and Anuradha Gupta, Inferring spin tilts at formation from gravitational wave observations of binary black

holes: Interfacing precession-averaged and orbit-averaged spin evolution, Phys. Rev. D **106**, 023001 (2022).

[192] C. M. Biwer, Collin D. Capano, Soumi De, Miriam Cabero, Duncan A. Brown, Alexander H. Nitz, and V. Raymond, PyCBC inference: A Python-based parameter estimation toolkit for compact binary coalescence signals, Publ. Astron. Soc. Pac. **131**, 024503 (2019).

[193] Alexander H. Nitz, Collin D. Capano, Sumit Kumar, Yi-Fan Wang, Shilpa Kastha, Marlin Schäfer, Rahul Dhurkunde, and Miriam Cabero, 3-OGC: Catalog of gravitational waves from compact-binary mergers, https://github.com/gwastro/3-ogc (2021).

[194] Yiwen Huang, Carl-Johan Haster, Salvatore Vitale, Aaron Zimmerman, Javier Roulet, Tejaswi Venumadhav, Barak Zackay, Liang Dai, and Matias Zaldarriaga, Source properties of the lowest signal-to-noise-ratio binary black hole detections, Phys. Rev. D **102**, 103024 (2020).

[195] Rich Abbott *et al.* (LIGO Scientific, Virgo, and KAGRA Collaborations), Search for intermediate-mass black hole binaries in the third observing run of Advanced LIGO and Advanced Virgo, Astron. Astrophys. **659**, A84 (2022).

[196] R. Abbott *et al.* (LIGO Scientific Collaboration and Virgo Collaboration), GW190521: A Binary Black Hole Merger with a Total Mass of $150 M_{\odot}$, Phys. Rev. Lett. **125**, 101102 (2020).

[197] R. Abbott *et al.* (LIGO Scientific Collaboration and Virgo Collaboration), Properties and astrophysical implications of the $150 M_{\odot}$ binary black hole merger GW190521, Astrophys. J. Lett. **900**, L13 (2020).

[198] Maya Fishbach and Daniel E. Holz, Where are LIGO's big black holes?, Astrophys. J. Lett. **851**, L25 (2017).

[199] Colm Talbot and Eric Thrane, Measuring the binary black hole mass spectrum with an astrophysically motivated parameterization, Astrophys. J. **856**, 173 (2018).

[200] Yuan-Zhu Wang, Shao-Peng Tang, Yun-Feng Liang, Ming-Zhe Han, Xiang Li, Zhi-Ping Jin, Yi-Zhong Fan, and Da-Ming Wei, Black hole mass function of coalescing binary black hole systems: Is there a pulsational pair instability mass cutoff?, Astrophys. J. **913**, 42 (2021).

[201] Yin-Jie Li, Yuan-Zhu Wang, Ming-Zhe Han, Shao-Peng Tang, Qiang Yuan, Yi-Zhong Fan, and Da-Ming Wei, A flexible Gaussian process reconstruction method and the mass function of the coalescing binary black hole systems, Astrophys. J. **917**, 33 (2021).

[202] Bruce Edelman, Zoheyr Doctor, and Ben Farr, Poking holes: Looking for gaps in LIGO/Virgo's black hole population, Astrophys. J. Lett. **913**, L23 (2021).

[203] Eric J. Baxter, Djuna Croon, Samuel D. McDermott, and Jeremy Sakstein, Find the gap: Black hole population analysis with an astrophysically motivated mass function, Astrophys. J. Lett. **916**, L16 (2021).

[204] Mario Spera and Michela Mapelli, Very massive stars, pair-instability supernovae and intermediate-mass black holes with the sevn code, Mon. Not. R. Astron. Soc. **470**, 4739 (2017).

[205] M. Renzo, R. Farmer, S. Justham, Y. Götberg, S. E. de Mink, E. Zapartas, P. Marchant, and N. Smith, Predictions for the hydrogen-free ejecta of pulsational pair-instability supernovae, Astron. Astrophys. **640**, A56 (2020).

[206] M. Coleman Miller and Douglas P. Hamilton, Production of intermediate-mass black holes in globular clusters, Mon. Not. R. Astron. Soc. **330**, 232 (2002).

[207] Fabio Antonini and Frederic A. Rasio, Merging black hole binaries in galactic nuclei: Implications for Advanced-LIGO detections, Astrophys. J. **831**, 187 (2016).

[208] Davide Gerosa and Emanuele Berti, Are merging black holes born from stellar collapse or previous mergers?, Phys. Rev. D **95**, 124046 (2017).

[209] Maya Fishbach, Daniel E. Holz, and Ben Farr, Are LIGO's black holes made from smaller black holes?, Astrophys. J. Lett. **840**, L24 (2017).

[210] Fabio Antonini, Mark Gieles, and Alessia Gualandris, Black hole growth through hierarchical black hole mergers in dense star clusters: Implications for gravitational wave detections, Mon. Not. R. Astron. Soc. **486**, 5008 (2019).

[211] Carl L. Rodriguez, Michael Zevin, Pau Amaro-Seoane, Sourav Chatterjee, Kyle Kremer, Frederic A. Rasio, and Claire S. Ye, Black holes: The next generation—repeated mergers in dense star clusters and their gravitational-wave properties, Phys. Rev. D **100**, 043027 (2019).

[212] Chase Kimball, Colm Talbot, Christopher P. L. Berry, Matthew Carney, Michael Zevin, Eric Thrane, and Vicky Kalogera, Black hole genealogy: Identifying hierarchical mergers with gravitational waves, Astrophys. J. **900**, 177 (2020).

[213] Giacomo Fragione, Abraham Loeb, and Frederic A. Rasio, On the origin of GW190521-like events from repeated black hole mergers in star clusters, Astrophys. J. **902**, L26 (2020).

[214] Z. Doctor, D. Wysocki, R. O'Shaughnessy, D. E. Holz, and B. Farr, Black hole coagulation: Modeling hierarchical mergers in black hole populations, Astrophys. J. **893**, 35 (2020).

[215] Antonella Palmese and Christopher J. Conselice, GW190521 from the Merger of Ultradwarf Galaxies, Phys. Rev. Lett. **126**, 181103 (2021).

[216] Vishal Baibhav, Davide Gerosa, Emanuele Berti, Kaze W. K. Wong, Thomas Helfer, and Matthew Mould, The mass gap, the spin gap, and the origin of merging binary black holes, Phys. Rev. D **102**, 043002 (2020).

[217] Michela Mapelli, Marco Dall'Amico, Yann Bouffanais, Nicola Giacobbo, Manuel Arca Sedda, M. Celeste Artale, Alessandro Ballone, Ugo N. Di Carlo, Giuliano Iorio, Filippo Santoliquido, and Stefano Torniamenti, Hierarchical black hole mergers in young, globular and nuclear star clusters: The effect of metallicity, spin and cluster properties, Mon. Not. R. Astron. Soc. **505**, 339 (2021).

[218] Ugo N. Di Carlo, Nicola Giacobbo, Michela Mapelli, Mario Pasquato, Mario Spera, Long Wang, and Francesco Haardt, Merging black holes in young star clusters, Mon. Not. R. Astron. Soc. **487**, 2947 (2019).

[219] Ugo N. Di Carlo, Michela Mapelli, Yann Bouffanais, Nicola Giacobbo, Filippo Santoliquido, Alessandro Bressan, Mario Spera, and Francesco Haardt, Binary black holes in the pair instability mass gap, Mon. Not. R. Astron. Soc. **497**, 1043 (2020).

[220] Kyle Kremer, Mario Spera, Devin Becker, Sourav Chatterjee, Ugo N. Di Carlo, Giacomo Fragione, Carl L. Rodriguez, Claire S. Ye, and Frederic A. Rasio, Populating

the upper black hole mass gap through stellar collisions in young star clusters, Astrophys. J. **903**, 45 (2020).

[221] M. Renzo, M. Cantiello, B. D. Metzger, and Y. F. Jiang, The stellar merger scenario for black holes in the pair-instability gap, Astrophys. J. Lett. **904**, L13 (2020).

[222] B. McKernan, K. E. S. Ford, W. Lyra, and H. B. Perets, Intermediate mass black holes in AGN discs—I. Production and growth, Mon. Not. R. Astron. Soc. **425**, 460 (2012).

[223] Imre Bartos, Bence Kocsis, Zoltán Haiman, and Szabolcs Márka, Rapid and bright stellar-mass binary black hole mergers in active galactic nuclei, Astrophys. J. **835**, 165 (2017).

[224] Nicholas C. Stone, Brian D. Metzger, and Zoltán Haiman, Assisted inspirals of stellar mass black holes embedded in AGN discs: Solving the "final au problem", Mon. Not. R. Astron. Soc. **464**, 946 (2017).

[225] Barry McKernan, K. E. Saavik Ford, J. Bellovary, N. W. C. Leigh, Z. Haiman, B. Kocsis, W. Lyra, M. M. Mac Low, B. Metzger, M. O'Dowd, S. Endlich, and D. J. Rosen, Constraining stellar-mass black hole mergers in AGN disks detectable with LIGO, Astrophys. J. **866**, 66 (2018).

[226] Y. Yang, I. Bartos, V. Gayathri, K. E. S. Ford, Z. Haiman, S. Klimenko, B. Kocsis, S. Márka, Z. Márka, B. McKernan, and R. O'Shaughnessy, Hierarchical Black Hole Mergers in Active Galactic Nuclei, Phys. Rev. Lett. **123**, 181101 (2019).

[227] Hiromichi Tagawa, Zoltán Haiman, Imre Bartos, and Bence Kocsis, Spin evolution of stellar-mass black hole binaries in active galactic nuclei, Astrophys. J. **899**, 26 (2020).

[228] Hiromichi Tagawa, Bence Kocsis, Zoltán Haiman, Imre Bartos, Kazuyuki Omukai, and Johan Samsing, Mass-gap mergers in active galactic nuclei, Astrophys. J. **908**, 194 (2021).

[229] Zacharias Roupas and Demosthenes Kazanas, Generation of massive stellar black holes by rapid gas accretion in primordial dense clusters, Astron. Astrophys. **632**, L8 (2019).

[230] Mohammadtaher Safarzadeh and Zoltán Haiman, Formation of GW190521 via gas accretion onto Population III stellar black hole remnants born in high-redshift minihalos, Astrophys. J. **903**, L21 (2020).

[231] Jared R. Rice and Bing Zhang, Growth of stellar-mass black holes in dense molecular clouds and GW190521, Astrophys. J. **908**, 59 (2021).

[232] L. A. C. van Son, S. E. De Mink, F. S. Broekgaarden, M. Renzo, S. Justham, E. Laplace, J. Morán-Fraile, D. D. Hendriks, and R. Farmer, Polluting the pair-instability mass gap for binary black holes through super-eddington accretion in isolated binaries, Astrophys. J. **897**, 100 (2020).

[233] Sebastien Clesse and Juan Garcia-Bellido, GW190425, GW190521, and GW190814: Three candidate mergers of primordial black holes from the QCD epoch, Phys. Dark Universe **38**, 101111 (2022).

[234] V. De Luca, V. Desjacques, G. Franciolini, P. Pani, and A. Riotto, GW190521 Mass Gap Event and the Primordial Black Hole Scenario, Phys. Rev. Lett. **126**, 051101 (2021).

[235] K. Belczynski *et al.*, Evolutionary roads leading to low effective spins, high black hole masses, and O1/O2 rates for LIGO/Virgo binary black holes, Astron. Astrophys. **636**, A104 (2020).

[236] Djuna Croon, Samuel D. McDermott, and Jeremy Sakstein, New physics and the black hole mass gap, Phys. Rev. D **102**, 115024 (2020).

[237] S. E. Woosley and Alexander Heger, The pair-instability mass gap for black holes, Astrophys. J. Lett. **912**, L31 (2021).

[238] Piero Madau and Martin J. Rees, Massive black holes as Population III remnants, Astrophys. J. Lett. **551**, L27 (2001).

[239] S. E. Woosley, A. Heger, and T. A. Weaver, The evolution and explosion of massive stars, Rev. Mod. Phys. **74**, 1015 (2002).

[240] Ataru Tanikawa, Tomoya Kinugawa, Takashi Yoshida, Kotaro Hijikawa, and Hideyuki Umeda, Population III binary black holes: Effects of convective overshooting on formation of GW190521, Mon. Not. R. Astron. Soc. **505**, 2170 (2021).

[241] Tomoya Kinugawa, Takashi Nakamura, and Hiroyuki Nakano, Formation of binary black holes similar to GW190521 with a total mass of $\sim 150 M_\odot$ from Population III binary star evolution, Mon. Not. R. Astron. Soc. **501**, L49 (2021).

[242] Simone S. Bavera, Tassos Fragos, Ying Qin, Emmanouil Zapartas, Coenraad J. Neijssel, Ilya Mandel, Aldo Batta, Sebastian M. Gaebel, Chase Kimball, and Simon Stevenson, The origin of spin in binary black holes. Predicting the distributions of the main observables of Advanced LIGO, Astron. Astrophys. **635**, A97 (2020).

[243] Jim Fuller, Anthony L. Piro, and Adam S. Jermyn, Slowing the spins of stellar cores, Mon. Not. R. Astron. Soc. **485**, 3661 (2019).

[244] Jim Fuller and Linhao Ma, Most black holes are born very slowly rotating, Astrophys. J. Lett. **881**, L1 (2019).

[245] H. C. Spruit, Dynamo action by differential rotation in a stably stratified stellar interior, Astron. Astrophys. **381**, 923 (2002).

[246] Christopher S. Reynolds, Observational constraints on black hole spin, Annu. Rev. Astron. Astrophys. **59**, 117 (2021).

[247] James C. A. Miller-Jones *et al.*, Cygnus X-1 contains a 21–solar mass black hole—Implications for massive star winds, Science **371**, 1046 (2021).

[248] Ying Qin, Pablo Marchant, Tassos Fragos, Georges Meynet, and Vicky Kalogera, On the origin of black hole spin in high-mass x-ray binaries, Astrophys. J. **870**, L18 (2019).

[249] Kenta Hotokezaka and Tsvi Piran, Implications of the low binary black hole aligned spins observed by LIGO, Astrophys. J. **842**, 111 (2017).

[250] Y. Qin, T. Fragos, G. Meynet, J. Andrews, M. Sørensen, and H. F. Song, The spin of the second-born black hole in coalescing binary black holes, Astron. Astrophys. **616**, A28 (2018).

[251] Pablo Marchant, Norbert Langer, Philipp Podsiadlowski, Thomas M. Tauris, and Takashi J. Moriya, A new route

towards merging massive black holes, Astron. Astrophys. **588**, A50 (2016).

[252] Ilya Mandel and Selma E. de Mink, Merging binary black holes formed through chemically homogeneous evolution in short-period stellar binaries, Mon. Not. R. Astron. Soc. **458**, 2634 (2016).

[253] Chase Kimball, Christopher Berry, and Vicky Kalogera, What GW170729's exceptional mass and spin tells us about its family tree, Res. Notes Am. Astron. Soc. **4**, 2 (2020).

[254] Davide Gerosa and Maya Fishbach, Hierarchical mergers of stellar-mass black holes and their gravitational-wave signatures, Nat. Astron. **5**, 749 (2021).

[255] Vassiliki Kalogera, Spin-orbit misalignment in close binaries with two compact objects, Astrophys. J. **541**, 319 (2000).

[256] Davide Gerosa, Emanuele Berti, Richard O'Shaughnessy, Krzysztof Belczynski, Michael Kesden, Daniel Wysocki, and Wojciech Gladysz, Spin orientations of merging black holes formed from the evolution of stellar binaries, Phys. Rev. D **98**, 084036 (2018).

[257] Carl L. Rodriguez, Michael Zevin, Chris Pankow, Vasilliki Kalogera, and Frederic A. Rasio, Illuminating black hole binary formation channels with spins in Advanced LIGO, Astrophys. J. Lett. **832**, L2 (2016).

[258] Will M. Farr, Simon Stevenson, M. Coleman Miller, Ilya Mandel, Ben Farr, and Alberto Vecchio, Distinguishing spin-aligned and isotropic black hole populations with gravitational waves, Nature (London) **548**, 426 (2017).

[259] S. E. de Mink and I. Mandel, The chemically homogeneous evolutionary channel for binary black hole mergers: Rates and properties of gravitational-wave events detectable by advanced LIGO, Mon. Not. R. Astron. Soc. **460**, 3545 (2016).

[260] Michal Dominik, Krzysztof Belczynski, Christopher Fryer, Daniel E. Holz, Emanuele Berti, Tomasz Bulik, Ilya Mandel, and Richard O'Shaughnessy, Double compact objects. I. The significance of the common envelope on merger rates, Astrophys. J. **759**, 52 (2012).

[261] J. J. Eldridge and E. R. Stanway, BPASS predictions for binary black hole mergers, Mon. Not. R. Astron. Soc. **462**, 3302 (2016).

[262] Nicola Giacobbo and Michela Mapelli, The progenitors of compact-object binaries: Impact of metallicity, common envelope and natal kicks, Mon. Not. R. Astron. Soc. **480**, 2011 (2018).

[263] Coenraad J. Neijssel, Alejandro Vigna-Gómez, Simon Stevenson, Jim W. Barrett, Sebastian M. Gaebel, Floor S. Broekgaarden, Selma E. de Mink, Dorottya Szécsi, Serena Vinciguerra, and Ilya Mandel, The effect of the metallicity-specific star formation history on double compact object mergers, Mon. Not. R. Astron. Soc. **490**, 3740 (2019).

[264] Charles D. Bailyn, Raj K. Jain, Paolo Coppi, and Jerome A. Orosz, The mass distribution of stellar black holes, Astrophys. J. **499**, 367 (1998).

[265] Feryal Özel, Dimitrios Psaltis, Ramesh Narayan, and Jeffrey E. McClintock, The black hole mass distribution in the galaxy, Astrophys. J. **725**, 1918 (2010).

[266] Will M. Farr, Niharika Sravan, Andrew Cantrell, Laura Kreidberg, Charles D. Bailyn, Ilya Mandel, and Vicky Kalogera, The mass distribution of stellar-mass black holes, Astrophys. J. **741**, 103 (2011).

[267] Todd A. Thompson, Christopher S. Kochanek, Krzysztof Z. Stanek, Carles Badenes, Tharindu Jayasinghe, Jamie Tayar, Jennifer A. Johnson, Thomas W. S. Holoien, Katie Auchettl, and Kevin Covey, Response to Comment on "A noninteracting low-mass black hole-giant star binary system", Science **368**, eaba4356 (2020).

[268] T. Jayasinghe *et al.*, A unicorn in monoceros: The $3M_\odot$ dark companion to the bright, nearby red giant V723 Mon is a non-interacting, mass-gap black hole candidate, Mon. Not. R. Astron. Soc. **504**, 2577 (2021).

[269] Ł. Wyrzykowski *et al.*, Black hole, neutron star and white dwarf candidates from microlensing with OGLE-III, Mon. Not. R. Astron. Soc. **458**, 3012 (2016).

[270] Łukasz Wyrzykowski and Ilya Mandel, Constraining the masses of microlensing black holes and the mass gap with Gaia DR2, Astron. Astrophys. **636**, A20 (2020).

[271] Maya Fishbach, Reed Essick, and Daniel E. Holz, Does matter matter? Using the mass distribution to distinguish neutron stars and black holes, Astrophys. J. **899**, L8 (2020).

[272] Chris L. Fryer, Krzysztof Belczynski, Grzegorz Wiktorowicz, Michal Dominik, Vicky Kalogera, and Daniel E. Holz, Compact remnant mass function: Dependence on the explosion mechanism and metallicity, Astrophys. J. **749**, 91 (2012).

[273] Marco Limongi and Alessandro Chieffi, Presupernova evolution and explosive nucleosynthesis of rotating massive stars in the metallicity range $-3 \leq [\mathrm{Fe/H}] \leq 0$, Astrophys. J. Suppl. Ser. **237**, 13 (2018).

[274] Michael Zevin, Mario Spera, Christopher P. L. Berry, and Vicky Kalogera, Exploring the lower mass gap and unequal mass regime in compact binary evolution, Astrophys. J. Lett. **899**, L1 (2020).

[275] Ilya Mandel and Bernhard Müller, Simple recipes for compact remnant masses and natal kicks, Mon. Not. R. Astron. Soc. **499**, 3214 (2020).

[276] Anuradha Gupta, Davide Gerosa, K. G. Arun, Emanuele Berti, Will M. Farr, and B. S. Sathyaprakash, Black holes in the low-mass gap: Implications for gravitational-wave observations, Phys. Rev. D **101**, 103036 (2020).

[277] Bin Liu and Dong Lai, Hierarchical black hole mergers in multiple systems: Constrain the formation of GW190412-, GW190814-, and GW190521-like events, Mon. Not. R. Astron. Soc. **502**, 2049 (2021).

[278] Wenbin Lu, Paz Beniamini, and Clément Bonnerot, On the formation of GW190814, Mon. Not. R. Astron. Soc. **500**, 1817 (2021).

[279] Manuel Arca Sedda, Dynamical formation of the GW190814 merger, Astrophys. J. Lett. **908**, L38 (2021).

[280] Kyriakos Vattis, Isabelle S. Goldstein, and Savvas M. Koushiappas, Could the $2.6M_\odot$ object in GW190814 be a primordial black hole?, Phys. Rev. D **102**, 061301 (2020).

[281] Mohammadtaher Safarzadeh and Daniel Wysocki, A common origin for low-mass ratio events observed by LIGO and Virgo in the first half of the third observing run, Astrophys. J. Lett. **907**, L24 (2021).

[282] Krzysztof Belczynski, Vassiliki Kalogera, and Tomasz Bulik, A comprehensive study of binary compact objects

as gravitational wave sources: Evolutionary channels, rates, and physical properties, Astrophys. J. **572**, 407 (2002).

[283] J. J. Eldridge, E. R. Stanway, and Petra N. Tang, A consistent estimate for gravitational wave and electromagnetic transient rates, Mon. Not. R. Astron. Soc. **482**, 870 (2019).

[284] Michela Mapelli, Nicola Giacobbo, Filippo Santoliquido, and Maria Celeste Artale, The properties of merging black holes and neutron stars across cosmic time, Mon. Not. R. Astron. Soc. **487**, 2 (2019).

[285] Sara Rastello, Michela Mapelli, Ugo N. Di Carlo, Nicola Giacobbo, Filippo Santoliquido, Mario Spera, Alessandro Ballone, and Giuliano Iorio, Dynamics of black hole-neutron star binaries in young star clusters, Mon. Not. R. Astron. Soc. **497**, 1563 (2020).

[286] Debatri Chattopadhyay, Simon Stevenson, Jarrod R. Hurley, Matthew Bailes, and Floor Broekgaarden, Modelling neutron star–black hole binaries: Future pulsar surveys and gravitational wave detectors, Mon. Not. R. Astron. Soc. **504**, 3682 (2021).

[287] P. Drozda, K. Belczynski, R. O'Shaughnessy, T. Bulik, and C. L. Fryer, Black hole–neutron star mergers: The first mass gap and kilonovae, Astron. Astrophys. **667**, A126 (2022).

[288] Floor S. Broekgaarden, Edo Berger, Coenraad J. Neijssel, Alejandro Vigna-Gómez, Debatri Chattopadhyay, Simon Stevenson, Martyna Chruslinska, Stephen Justham, Selma E. de Mink, and Ilya Mandel, Impact of massive binary star and cosmic evolution on gravitational wave observations I: Black hole–neutron star mergers, Mon. Not. R. Astron. Soc. **508**, 5028 (2021).

[289] Sebastian M. Gaebel, John Veitch, Thomas Dent, and Will M. Farr, Digging the population of compact binary mergers out of the noise, Mon. Not. R. Astron. Soc. **484**, 4008 (2019).

[290] Shanika Galaudage, Colm Talbot, and Eric Thrane, Gravitational-wave inference in the catalog era: Evolving priors and marginal events, Phys. Rev. D **102**, 083026 (2020).

[291] Leo P. Singer and Larry R. Price, Rapid Bayesian position reconstruction for gravitational-wave transients, Phys. Rev. D **93**, 024013 (2016).

[292] Leo P. Singer *et al.*, Going the distance: Mapping host galaxies of LIGO and Virgo sources in three dimensions using local cosmography and targeted follow-up, Astrophys. J. Lett. **829**, L15 (2016).

[293] T. Akutsu *et al.* (KAGRA Collaboration), KAGRA: 2.5 Generation interferometric gravitational wave detector, Nat. Astron. **3**, 35 (2019).

[294] Ryan Magee *et al.*, First demonstration of early warning gravitational wave alerts, Astrophys. J. Lett. **910**, L21 (2021).

[295] Alexander H. Nitz, Marlin Schäfer, and Tito Dal Canton, Gravitational-wave merger forecasting: Scenarios for the early detection and localization of compact-binary mergers with ground-based observatories, Astrophys. J. Lett. **902**, L29 (2020).

[296] Surabhi Sachdev *et al.*, An early-warning system for electromagnetic follow-up of gravitational-wave events, Astrophys. J. Lett. **905**, L25 (2020).

[297] https://dcc.ligo.org/LIGO-M2300033/public.

[298] Kipp Cannon *et al.*, GstLAL: A software framework for gravitational wave discovery, SoftwareX **14**, 100680 (2021).

[299] T. Adams, D. Buskulic, V. Germain, G. M. Guidi, F. Marion, M. Montani, B. Mours, F. Piergiovanni, and G. Wang, Low-latency analysis pipeline for compact binary coalescences in the advanced gravitational wave detector era, Classical Quantum Gravity **33**, 175012 (2016).

[300] Tyson B. Littenberg, Jonah B. Kanner, Neil J. Cornish, and Margaret Millhouse, Enabling high confidence detections of gravitational-wave bursts, Phys. Rev. D **94**, 044050 (2016).

[301] Joshua S. Speagle, dynesty: A dynamic nested sampling package for estimating Bayesian posteriors and evidences, Mon. Not. R. Astron. Soc. **493**, 3132 (2020).

[302] John D. Hunter, Matplotlib: A 2D graphics environment, Comput. Sci. Eng. **9**, 90 (2007).

[303] Michael L. Waskom, SEABORN: Statistical data visualization, J. Open Source Softwaare **6**, 3021 (2021).

[304] Charles R. Harris *et al.*, Array programming with NumPy, Nature (London) **585**, 357 (2020).

[305] Pauli Virtanen *et al.*, SciPy 1.0–Fundamental algorithms for scientific computing in Python, Nat. Methods **17**, 261 (2020).

[306] LIGO Scientific Collaboration and Virgo Collaboration, Parameter estimation sample release for GWTC-1, Technical Report No. P1800370, LIGO DCC, 2019.

[307] B. P. Abbott *et al.* (LIGO Scientific Collaboration and Virgo Collaboration), GW151226: Observation of Gravitational Waves from a 22-Solar-Mass Binary Black Hole Coalescence, Phys. Rev. Lett. **116**, 241103 (2016).

[308] Maite Mateu-Lucena, Sascha Husa, Marta Colleoni, Héctor Estellés, Cecilio García-Quirós, David Keitel, Maria de Lluc Planas, and Antoni Ramos-Buades, Parameter estimation with the current generation of phenomenological waveform models applied to the black hole mergers of GWTC-1, Mon. Not. R. Astron. Soc. **517**, 2403 (2022).

[309] LIGO Scientific Collaboration and Virgo Collaboration, GWTC-2 Data release: Parameter estimation samples and skymaps, Technical Report No. P2000223, LIGO DCC, 2020.

[310] Tousif Islam, Scott E. Field, Carl-Johan Haster, and Rory Smith, Improved analysis of GW190412 with a precessing numerical relativity surrogate waveform model, Phys. Rev. D **103**, 104027 (2021).

[311] Marta Colleoni, Maite Mateu-Lucena, Héctor Estellés, Cecilio García-Quirós, David Keitel, Geraint Pratten, Antoni Ramos-Buades, and Sascha Husa, Towards the routine use of subdominant harmonics in gravitational-wave inference: Reanalysis of GW190412 with generation X waveform models, Phys. Rev. D **103**, 024029 (2021).

[312] Michael Zevin, Christopher P. L. Berry, Scott Coughlin, Katerina Chatziioannou, and Salvatore Vitale, You can't always get what you want: The impact of prior assumptions on interpreting GW190412, Astrophys. J. Lett. **899**, L17 (2020).

[313] Rossella Gamba, Sarp Akçay, Sebastiano Bernuzzi, and Jake Williams, Effective-one-body waveforms for precessing coalescing compact binaries with post-newtonian twist, Phys. Rev. D **106**, 024020 (2022).

[314] Alexander H. Nitz and Collin D. Capano, GW190521 may be an intermediate mass ratio inspiral, Astrophys. J. Lett. **907**, L9 (2021).

[315] Collin D. Capano, Miriam Cabero, Julian Westerweck, Jahed Abedi, Shilpa Kastha, Alexander H. Nitz, Yi-Fan Wang, Alex B. Nielsen, and Badri Krishnan, Multimode quasinormal spectrum from a perturbed black hole, Phys. Rev. Lett. **131**, 221402 (2023).

[316] Héctor Estellés *et al.*, A detailed analysis of GW190521 with phenomenological waveform models, Astrophys. J. **924**, 79 (2022).

[317] Seth Olsen, Javier Roulet, Horng Sheng Chia, Liang Dai, Tejaswi Venumadhav, Barak Zackay, and Matias Zaldarriaga, Mapping the likelihood of GW190521 with diverse mass and spin priors, Phys. Rev. D **104**, 083036 (2021).